Clustering in iron-doped magnesium oxide

Inglis, A. D.

Clustering in Iron-doped Magnesium Oxide

by

A. D. Inglis, M. Sc.

A thesis

submitted to the University of Durham

in candidature for the degree of

Doctor of Philosophy

Department of Applied Physics
and Electronics,
Science Laboratories,
University of Durham, UK.
August, 1981

to Jodie

Acknowledgements

I would like to extend my grateful thanks to all those who have helped during the past three years. I am particularily indebted to

.....Professor G. G. Roberts, for the use of the research facilities in the department, and for his friendly interest and encouragement;

.....Dr J. S. Thorp, my supervisor, for his guidance and enthusiastic support;

.....Dr G. J. Russell, for willing assistance and advice, for many helpful discussions, and especially for taking the photographs included with Chapter 9;

.....and to the other members of the department, staff and students, who have not only helped with this work but have made the three years which Jodie and I have spent in Durham so enjoyable.

Abstract

The distribution of iron in single crystals of magnesium oxide has been investigated using electron paramagnetic resonance (EPR), ferrimagnetic resonance (FMR) and reflection electron diffraction (RED). The total iron content of the samples was in the range 100 - 13000 ppm by weight, the crystals being examined in the as-received state, after solution treatment, and following various aging treatments. The solution treatment involved the samples being held at 1400°C for 24 hours in an oxygen atmosphere, and then quenched to room temperature. The samples were aged in oxygen at temperatures in the range 600 - 800°C for various lengths of time.

The EPR investigations were carried out at 9 GHz, over the temperature range from 4 - 300 K. Comparison of the integrated intensity of the EPR spectral lines with those of a standard suggested that in both the as-received and solution treated crystals very little (in some cases <0.1%) of the iron contributes to the Fe^{3+} isolated ion cubic site spectrum. Analysis of the experimental linewidths and shapes lends support to this suggestion. The experimental linewidths are in all cases broader than is expected on the basis of dipolar broadening theory, and it is suggested that this broadening is partly due to interactions with the undetected fraction of the iron.

An unusual broad (1.3 kG wide) line which shows a complex structure at liquid helium temperatures was detected in two of the samples following solution treatment. Its appearance was accompanied by a complete absence of fine structure lines from the spectra in which it appeared. It is probable that the disappearance of the fine structure and the appearance of this broad line are related, but the

relationship is not at present clear.

Following aging treatments ferrimagnetic resonance was detected at 9 GHz, in the temperature range 4 - 500 K. This resonance arises out of the precipitation of magnesioferrite from the host lattice. In most of the samples which showed evidence of precipitation two quite different FMR lines were found - an isotropic line which appeared after short aging times, and an anisotropic line which apparently replaces the isotropic one as aging progresses.

Analysis of the measured anisotropy field of the particles precipitated at 800°C indicated that the rate of growth of the volume of the precipitates is linear with time, after about one hour's aging. The chemical formula for these particular precipitates was determined to be $Mg_xFe_{3-x}O_{4-(x-1)/2}$, where x = 1.29, the fraction of Mg ions on tetrahedral sites being taken to be 0.30.

Analysis of the magnetic characteristics of the precipitates generally gave agreement with what published data are available. In addition the measured anisotropy field H_a^{sp} in all samples was found to obey the empirical relationship

$$\sqrt{|H_a^{sp}|} = C + DT \qquad g^{0.5}$$

where D = -0.045 ± .004 $G^{0.5}$ K^{-1}, T is the temperature and C is a sample dependent constant.

The widths of the FMR lines obtained from the high concentration samples aged at 800°C were independent of sample, and after aging for one hour decreased monotonically with continued aging. This change in width is possibly a consequence of 'voids' of host material in the initial precipitates filling with aging. These

linewidths were also remarkable in that they showed a marked decrease with increased recording temperature. Since this behaviour is quite at variance with the behaviour of bulk magnesioferrite it is probably a consequence of the superparamagnetic nature of the particles.

Reflection electron diffraction studies of the etched surfaces of the crystals showed only one pattern - the standard spinel pattern - when ferrimagnetic precipitates were present, regardless of the type of FMR spectral line produced by the precipitates. This spinel had a lattice parameter almost exactly twice that of the host. Two other RED patterns were recorded from some of the samples - one possibly due to the calcium-stabilised zirconia discussed by Venables, and the other tentatively assigned to an aluminium spinel.

CONTENTS

CHAPTER 9

CHAPTER 1

Introduction

Magnesium oxide has been exploited in industry for many years as a refractory oxide, and in particular as an electrically insulating refractory oxide which will maintain its insulating properties over a range of temperatures. It is used for example as the insulator between filament and casing in electrical heating elements; and as the insulator surrounding instrumentation cables in nuclear reactor cores. Although generally reliable, magnesium oxide is prone to sudden electrical breakdown, especially when used at high temperatures. Despite extensive study during the past two or three decades neither the nature of the electrical conduction mechanism nor the mechanism of dielectric breakdown in this material has been unambiguously settled. It is thought that the impurities which occur even in the purest commercially available samples, and which may in addition diffuse in at high temperatures from the surrounding casing or heater filament probably play a role.

Many of these impurities, particularily those which are liable to diffuse in, are transition metal ions of the iron group. In an attempt to determine what role, if any, these impurities play in the electrical behaviour an extensive investigation of transition metal doped magnesium oxide has been carried out in this department. A variety of species of dopant have been investigated, over a range of dopant concentrations, using two principal means of attack. On the one hand electron paramagnetic resonance has been used to characterise

the dopant valence states and sites; on the other, a programme of dielectric measurements, across several decades of frequency, has been instigated.

To date these studies have concentrated on investigations of bought-in doped single crystals, mainly in the as-received state, and have usually been carried out at room temperature or below. There are many reports in the literature however which suggest that heat treatment of magnesium oxide, even over a temperature range of only a few hundred degrees above room temperature, may have a marked influence on the behaviour of the impurities, and especially on the behaviour of the iron ions. These are reported to change valence state, and to cluster or disperse, depending upon such factors as temperature range, ambient gas pressure, rate of cooling and impurity concentration. In particular it is suggested that clusters of ferrimagnetic spinel precipitates of the Mg - Fe - O system may form on heating and subsequent cooling. Since dielectric breakdown occurs in circumstances where the magnesium oxide is subject to - sometimes fluctuating - temperatures in excess of room temperature, it was decided to investigate samples of iron-doped single crystal magnesium oxide in an attempt to correlate spinel cluster formation with change in dielectric properties. Some of the work carried out during that investigation is presented in this thesis, which is concerned with a study of the formation of the spinel precipitates in iron doped magnesium oxide.

Electron paramagnetic resonance (EPR) was used to detect and characterise the isolated transition metal ions, in particular the iron ions. A dual-cavity method was used to compare the number of isolated ions with the total iron content in the as received samples

and linewidth measurements on other spectra obtained at the same stage allowed an analysis of the impurity ion interactions. The same spectrometer system was then used to detect and monitor the growth of the spinel clusters, which give rise to ferrimagnetic resonance (FMR). At some stages of the treatment some samples gave both EPR and FMR lines on the same spectra.

Much of the reported work on spinel cluster formation in magnesium oxide has involved transmission electron microscope (TEM) studies of the precipitates. However this is an essentially destructive technique in that the extremes of thinness required to allow transmission of the electron beam mean that the sample, once prepared for the electron microscope, is of little use for other, further, investigations. Reflection electron diffraction (RED) methods which involve 'reflecting' the electron beam from the sample surface at a very shallow angle do not require that the sample be thinned. This is the technique which was used in this work, but to ensure that the information obtained related to the bulk of the sample and not merely to the surface layer

i) TEM techniques were applied to selected samples

ii) some samples were heat treated and then cleaved, and the cleaved surfaces examined with RED.

Following some initial comments regarding defects and impurities in magnesium oxide, the work is reported in three sections. The EPR characterisation of the impurities and impurity states in the as-received crystals is described, and the findings are discussed, in Chapters 3 - 6; in Chapters 7 and 8 the FMR spectra are described, and analysed to yield information relating to the spinel precipitates and

precipitation; and in Chapter 9 the results of the RED studies are presented and discussed.

1.2 Previous Work

The alkali-earth oxides have been much studied, because of their technological importance and because besides being 'first cousins' to, and isostructural with the alkali halides, they may be obtained in the form of reasonably large single crystals which lend themselves to studies of the effects of defects and impurities on the lattice and its properties. Consequently, the literature is extensive - a review by Henderson and Wertz (1) published in 1977 includes a bibliography listing more than three hundred papers. Many more have appeared since. Here we mention only those papers which relate to magnesium oxide, either 'pure' or with iron doping. We include the 'pure' material since even the purest commercially available material has iron as an impurity.

Many authors (2 - 10) have addressed themselves to the behaviour of the solid Mg - Fe - O system under different conditions of temperature, and in different atmospheres, and as a result the behaviour of this system overall is reasonably well documented. However in order to deal with the system across the range from MgO to FeO these workers have generally dealt with combinations which have included at the least a few per cent of the minority cation; and it may be difficult and possibly erroneous to extrapolate from data so produced to the cases with which we are concerned here where the iron is present in concentrations of less than - and sometimes very much less than - one per cent.

The first direct evidence for isolated ions in octahedral

sites in MgO came from Low (11) who reported the EPR spectrum of isolated Fe^{3+} ions in such sites. His samples contained approximately one per cent iron, by weight, and it is of interest to note in view of what will follow later that he suggested that much of the iron in his samples was in the ferrous state. Later, Low and Weger (12) reported low temperature EPR spectra of Fe^{2+} in samples containing less than 0.01 per cent iron - and there have been several other reports of both Fe^{2+} (13,14) and Fe^{3+} (14 - 17) as isolated ions in sites of octahedral symmetry. Fe^{3+} has been found in sites of lower symmetry by Henderson et al (18) and Weeks et al (19). Spectra have also been reported of Fe^{1+} (13,20) but as this species is only produced in samples subjected to ionizing radiations no further reference will be made to it here.

The work of Brynestad and Flood (3) suggested that for materials in the Fe - Mg - O system the spectral state of the iron is dictated by iron concentration, heat treatment, and ambient atmosphere and pressure during this treatment. This is broadly confirmed by workers who have followed the variation in intensity of EPR spectral lines with heat treatment (21), but in view of the difficulty in obtaining an accurate measurement of concentration from these spectra one cannot be absolutely sure. The uncertainty is in part due to inaccuracies inherent in the method and in part to the fact that change of ionic state may not be the only change brought about by heat treatment. Clustering of impurities and vacancies may also occur, and unless one can clearly monitor both these changes at once, it is impossible to tell to what extent each effect may contribute to changes in spectra which take place during heat treatment.

This clustering phenomenon was studied in detail by Fine and

various co-workers (22 - 26). It was found that for samples containing between about one and five 'cation per cent' iron that heat treatment in the region of seven hundred degrees centigrade produced precipitates which were coherent with the lattice. The growth of these precipitates was studied using electron microscopy and magnetometry and they were shown to be precipitates, from the solid solution, of non-stoichiometric magnesioferrite. The exact cation content and distribution within these precipitates was found to depend upon aging temperature (23), whilst their final size depended upon the impurity content of the crystal (26). Many authors (27 - 33) have shown that these precipitates affect the strength of the single crystals in which they form, again the precise effect (and presumably the precise nature of the precipitate) depending upon the parameters considered by Brynestad and Flood.

Recently direct (19) and indirect (17,34) evidence from EPR studies has suggested that even with very low iron concentrations clustering, and possibly precipitation of magnesioferrite, occurs; and it would appear from the evidence that this is true not only for those crystals which have been heat treated but even for those in the 'as received' state.

Finally it is appropriate to mention the work of Gourdin, Kingery and Driear (35,36) who investigated theoretically the binding energies of various impurity/defect aggregates in magnesium oxide and concluded that for trivalent impurities such as Al^{3+} and Fe^{3+}, complex aggregates such as trimers and higher order clusters should be stable.

Whilst this review is by no means inclusive, it is certainly

representative. From these reports it would seem reasonable to draw the following conclusions regarding the expected behaviour of small quantities of iron in the magnesium oxide lattice:

the iron may be in the ferrous or ferric state;

the spectral state may be altered by the appropriate heat treatment;

in either state it is expected to substitute for Mg^{2+} when isolated;

in these circumstances the Fe^{3+} excess charge will be compensated by Mg^{2+} vacancies - one vacancy for every two ferric ions;

the compensation may be local, or non-local, the two situations being distinguishable by EPR;

appropriate heat treatments will cause precipitation of clusters of magnesioferrite spinel, of various degrees of stoichiometry.

CHAPTER 2

The Magnesium Oxide Samples : Structure, Defects and Treatment

2.1 The Structure of Magnesium Oxide.

Magnesium oxide crystallises with the 'rock-salt' structure (37) which may be described as two interpenetrating face-centred cubic lattices - one of magnesium ions and one of oxygen ions - aligned, but displaced along the body diagonal by one half of the length of the unit cell diagonal. However, since in practice the anion is very much larger than the cation the structure may perhaps be more easily visualised as a cubic close packed array of oxygen ions with magnesium ions occupying the octahedral interstices (see Figure 2.1).

The binding is predominantly ionic, each ion being surrounded by six nearest neighbours of the opposite sign charge. The lattice parameter (at 21^{o}C) is given (37) as a = 4.2112 Å. With a 'hard-shell' ionic model it should be possible to relate this lattice parameter to the ionic radii since for this structure

$$a = 2(r_+ + r_-)$$

where r_- and r_+ are anion and cation radii respectively (see Figure 2.2).

Unfortunately it is not possible to be as precise about ionic radii as it is about interplanar spacing. Various workers have tackled this problem, much of the work being reviewed by Shannon and Prewitt (38) who considered a large number of reported experimental

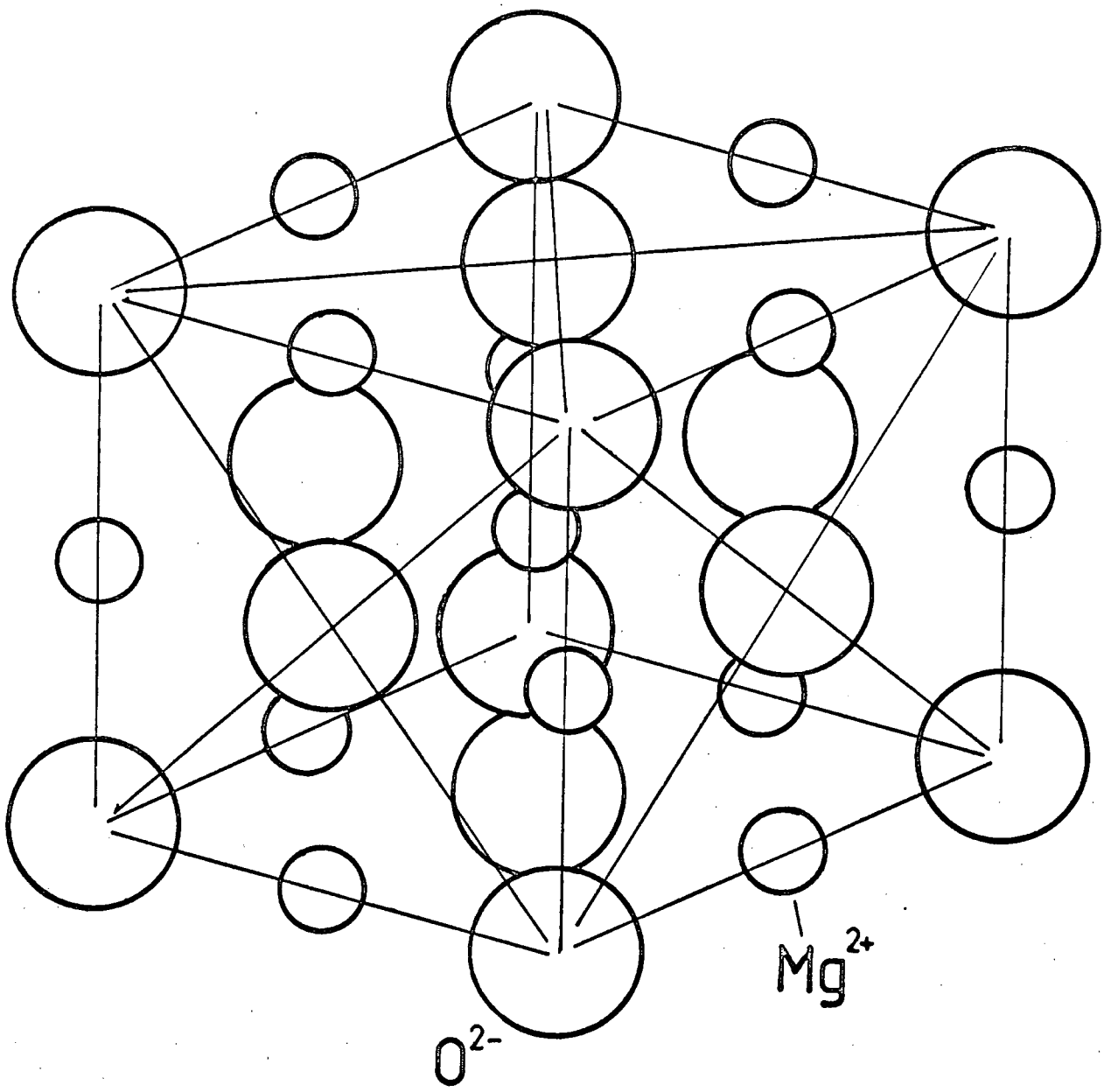

FIGURE 2,1 Unit Cell of MgO.

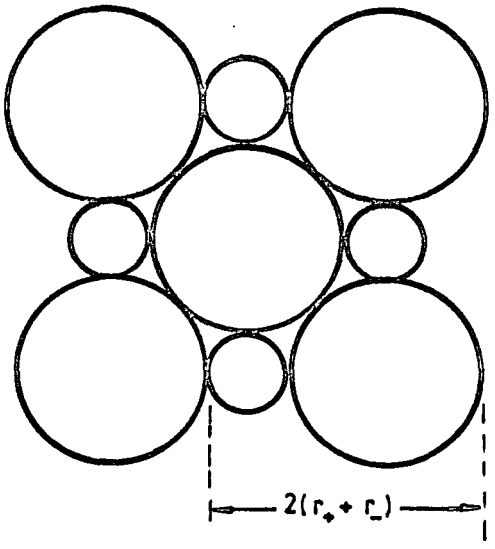

Figure 2.2 Idealised Rock-salt Structure

Figure 2.3 MgO Structure - showing separation of anions

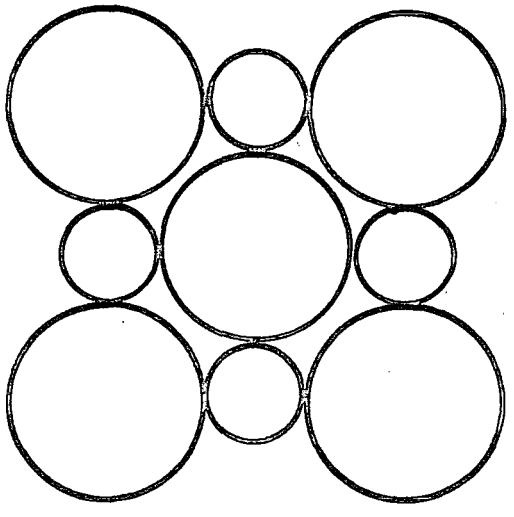

observations of interatomic distances, and assumed a linear relationship between ionic volume and unit cell volume for a series of isotypic oxides and fluorides. The values of radii which they tabulated were derived from this data but electronic spin state and the coordination of cations and anions, both of which are expected to affect the radii in the solid state, were taken into account. Shannon and Prewitt give values of ionic radii for magnesium and oxygen in six-fold coordination of

$$r_+(Mg^{2+}) = 0.72 \text{ Å} \qquad r_-(O^{2-}) = 1.40 \text{ Å}$$

These values suggest a unit cell parameter of 4.24 Å which is slightly larger than that found in practice (37). A similar discrepancy may be shown to arise with many of the highly symmetric rock-salt, fluorite and perovskite structures (38). It has been suggested that the observed interionic distances are a consequence of the minimization of anion - anion repulsion.

If one assumes that this minimisation will be partly brought about by the maintenance of a strict orthogonality within the oxygen sublattice and take the oxygen radius as being 1.40 Å (38) then the maximum allowable radius for a 'hard-shell' magnesium ion is only 0.58 Å, if anions are to be in contact with nearest-neighbour anions. By insisting on inserting a cation of 0.72 Å radius we partly separate the anions, as shown in Figure 2.3, providing they maintain their orientation with respect to the unit cell axes. This separation will reduce the interanionic repulsive force.

A second reason why we should not expect a 'hard-shell' model to yield an exact result arises out of consideration of the

degree of ionicity of the ions. No solid structure exhibits totally ionic bonding which would necessitate the complete transfer of (in our case two) electrons from one atom to another; bonding is always partly covalent. Since this covalency implies an overlapping of cation and anion electronic wave functions in the region between the cation and anion, it will allow tighter packing of the ions than would be allowed if the two ions were purely ionically bonded 'hard shells'. Bluck (39) has used an approach due to Pauling to roughly estimate the percentage ionic character of the bonding in MgO at sixty eight per cent.

It is expected that when magnesium oxide is doped with iron the iron ions will substitute for magnesium ions. Shannon and Prewitt give ionic radii for the charge states of iron in high spin states in octahedral sites as

$$Fe^{2+} \text{ - radius } = 0.77 \text{ Å} \quad : \quad Fe^{3+} \text{ - radius } = 0.65 \text{ Å}$$

This implies that the ferrous ion is slightly oversize, and the ferric ion slightly undersize when substituted for magnesium, and suggests that the Fe^{2+} ion will set up a strain in the surrounding lattice. That such an effect exists is indicated by the width of the EPR spectral line of Fe^{2+} (40). On the other hand because the Fe^{3+} ion is slightly smaller than the Mg^{2+} it can occupy the magnesium sites without causing distortion. Again this is borne out by the EPR spectra, which for isolated ions show a relatively narrow, highly isotropic central transition (16). The mechanism by which the excess charge of the ferric ion may be compensated is discussed in Section 2.2.

2.2 Defects and Impurities in Magnesium Oxide.

Even the purest magnesium oxide crystals available contain a large variety of impurity species. Typical quantities for crystals grown by W. and C. Spicer are shown in Table 2.1. We are particularily concerned in this study with the behaviour of iron, and there will of course be very much more iron than other impurities in crystals which have been deliberately doped with iron. Nevertheless, it should be borne in mind that other impurities such as aluminium may be present in a trivalent state; and these could be expected to behave analogously with iron as far as association between vacancies and impurities is concerned (35).

As regards lattice defects, grown in dislocations and low angle grain boundaries are plentiful (41). However, the crystals examined by RED always gave rise to apparently single crystal diffraction patterns, as did those one or two samples examined by x-ray back-reflection techniques: misorientation between grains was not thought to be more than a few minutes of arc at most. Both anion and cation vacancies are found in magnesium oxide and are readily detected since with suitable treatment they can be induced to trap holes and electrons, which give rise to EPR spectra (1).

Owing to their high energy of formation - in the region of 12 eV - interstitials of magnesium, oxygen or iron are not expected. On the other hand, calculations show that if combined with appropriate clusters of cation vacancies such interstitials are expected to be very stable (35): the formation of these interstitial-vacancy clusters is an essential stage in the formation of the spinel magnesioferrite structure as a precipitated phase.

TABLE 2.1: Typical impurity content of Spicer single crystal MgO. (See Ref.1).

Impurity	ppm.wt. present
Aluminium	35
Calcium	20
Silicon	15
Iron	3
Nickel	2
Manganese	0.1
Phosphorus	2
Lead	< 1
Sulphur	5
Copper	< 1
Zinc	5
Vanadium	< 2
Chromium	< 1
Arsenic,Potassium	< 5
Titanium	<20
Barium	<0.5
Sodium	1
Zirconium	3

The impurity iron ions, whether deliberately introduced or not, are thought to occupy the cation sites in the as-grown crystals (16,35), both ferric and ferrous states being stable. Brynestad and Flood (3) investigated material containing at least two cation per cent iron and derived a relationship between the fraction of iron in the Fe^{3+} state and the total quantity of iron, the temperature, and the oxygen partial pressure. Graphs illustrating these relationships are shown in Figure 2.4 and it can be seen that for temperatures up to about 700°C most of the iron is expected to be in the trivalent state. Above this temperature the iron is gradually reduced with increasing temperature. This reduction is greatest for the highest concentrations of iron, but the fraction reduced may be minimised by maximising the oxygen partial pressure. For this reason heat treatments carried out at 1400°C were always carried out in an oxygen atmosphere.

Although ferrous ions might reasonably be expected to occupy isolated sites as far as charge-balance considerations are concerned, Woods and Fine (26) suggested that they tend to cluster. This may be for purely mechanical reasons, in the sense that these ions are really too large for the cation sites and it could be that by clustering they reduce the total amount of strain which they introduce into the lattice. In the case of Fe^{3+} it is perhaps surprising, in the light of charge-balance considerations, that it may be so readily detected as an isolated ion in octahedral symmetry (11). The symmetry of the EPR spectrum is such that it is not thought that charge-compensating vacancies can be closer than about two lattice parameters.

According to the calculations of Gourdin, Kingery and Driear (35,36) trivalent impurity-vacancy dimers and trimers are expected to

form, and to remain stable. Two possible such arrangements are shown in Figure 2.5; trimers could appear as linear extensions of these. However, because of the closeness of association the EPR spectra of these iron ions would not show octahedral symmetry. Spectra from iron ions in sites of other symmetry have been recorded (18).

Using shell model calculations Gourdin and Kingery (35) find that, contrary to what might be expected if one merely considered a simple coulomb calculation for the binding energy of the dimers, the ⟨100⟩ orientation is more stable than the ⟨110⟩ . The intervening oxygen ion probably plays a key role here since both displacement of the ion core and polarisation of this ion would contribute to an increase in the binding energy. Fixing the positions of either the oxygen core or shell produces a considerable decrease in binding energy. The ⟨100⟩ trimer will have a greater binding energy than its ⟨110⟩ counterpart, for the same reasons, since the linear trimers are essentially two dimers placed end to end, and sharing a common vacancy.

In the same study the binding energies of more complex clusters, of the sort which would be required to bring about a localised change of the structure from rock-salt to spinel, were also considered. The simplest of these - which Gourdin and Kingery call a 4-1 cluster - is shown in Figure 2.6. It comprises an interstitial, with the four nearest-neighbour cation sites vacant and with four additional trivalent impurities placed symmetrically about the defect to diminish the overall charge of the region. It was calculated that this type of defect would be about as stable as the ⟨100⟩ linear trimer.

Combinations of such complex defects may be used to

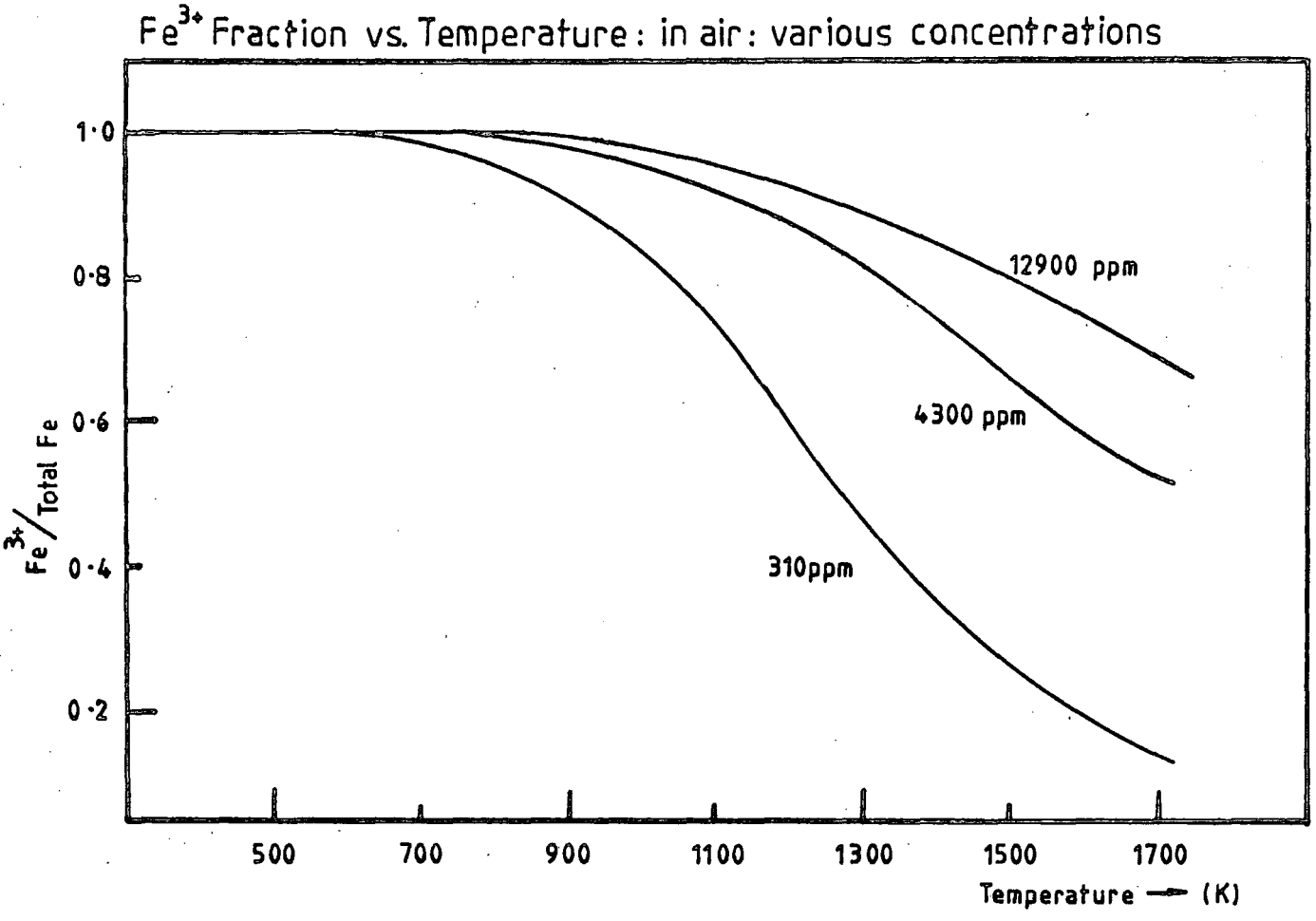

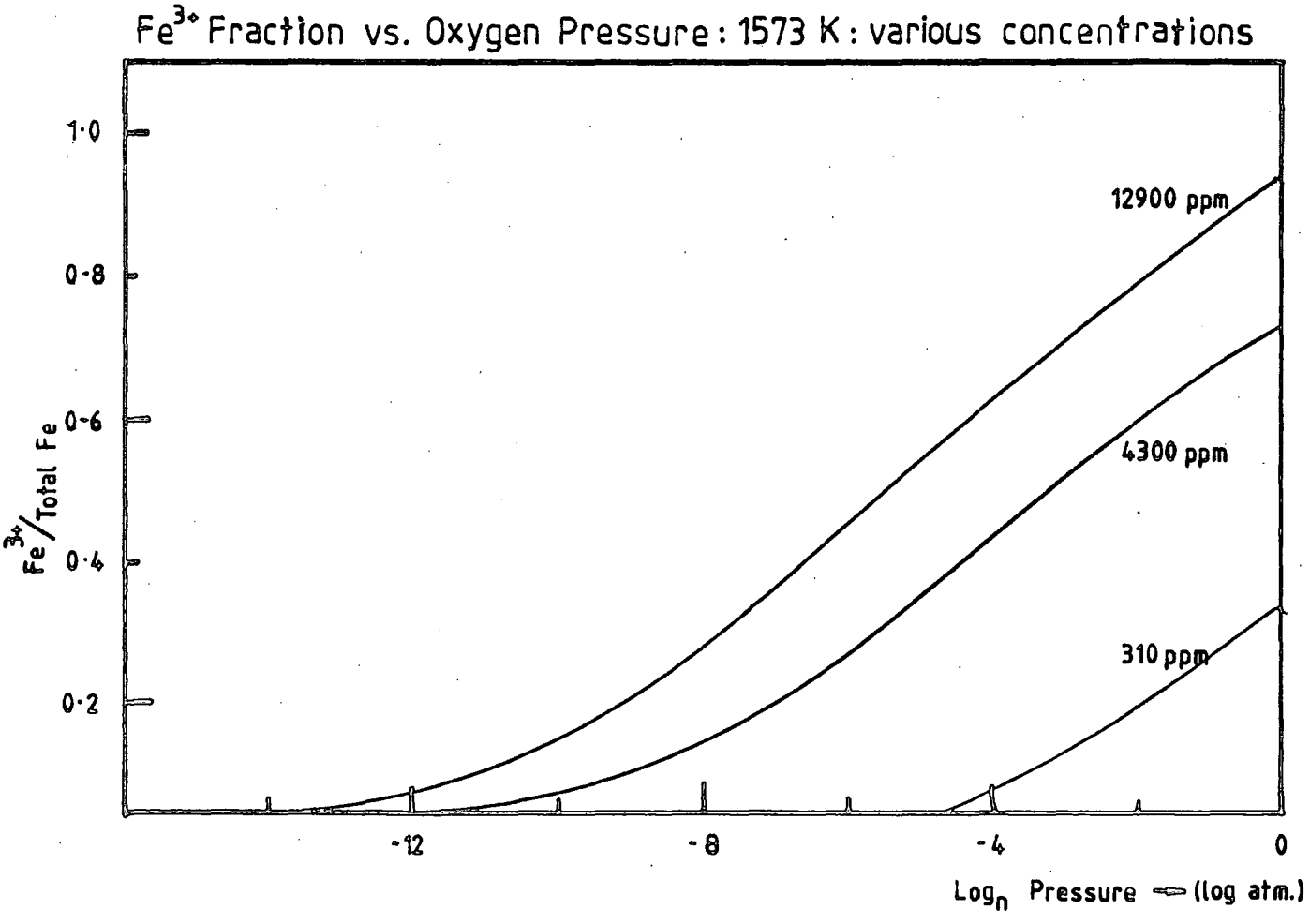

Figure 2.4 Variation of Fe^{3+} Fraction with temperature, oxygen pressure, and iron concentration

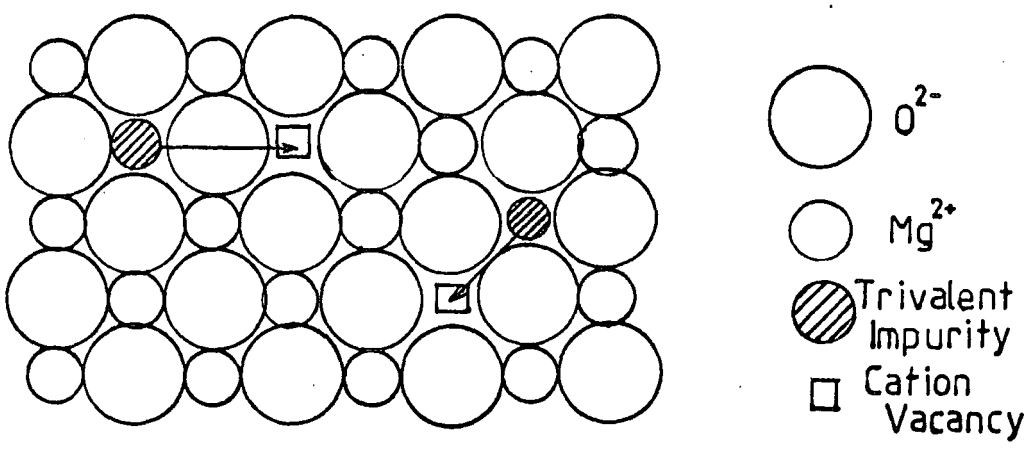

Figure 2.5 Impurity-Vacancy Dimers

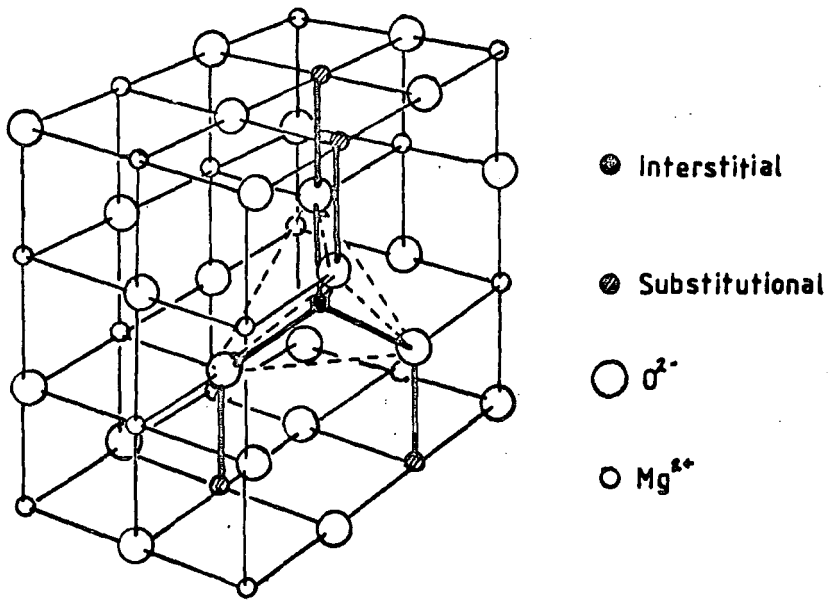

Figure 2.6 The '4-1' Cluster

(after Gourdin & Kingery)

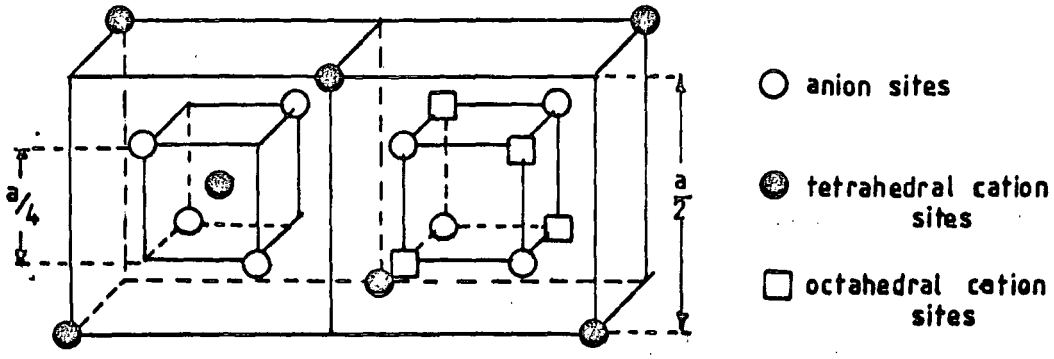

Figure 2.7 Two octants of the spinel lattice

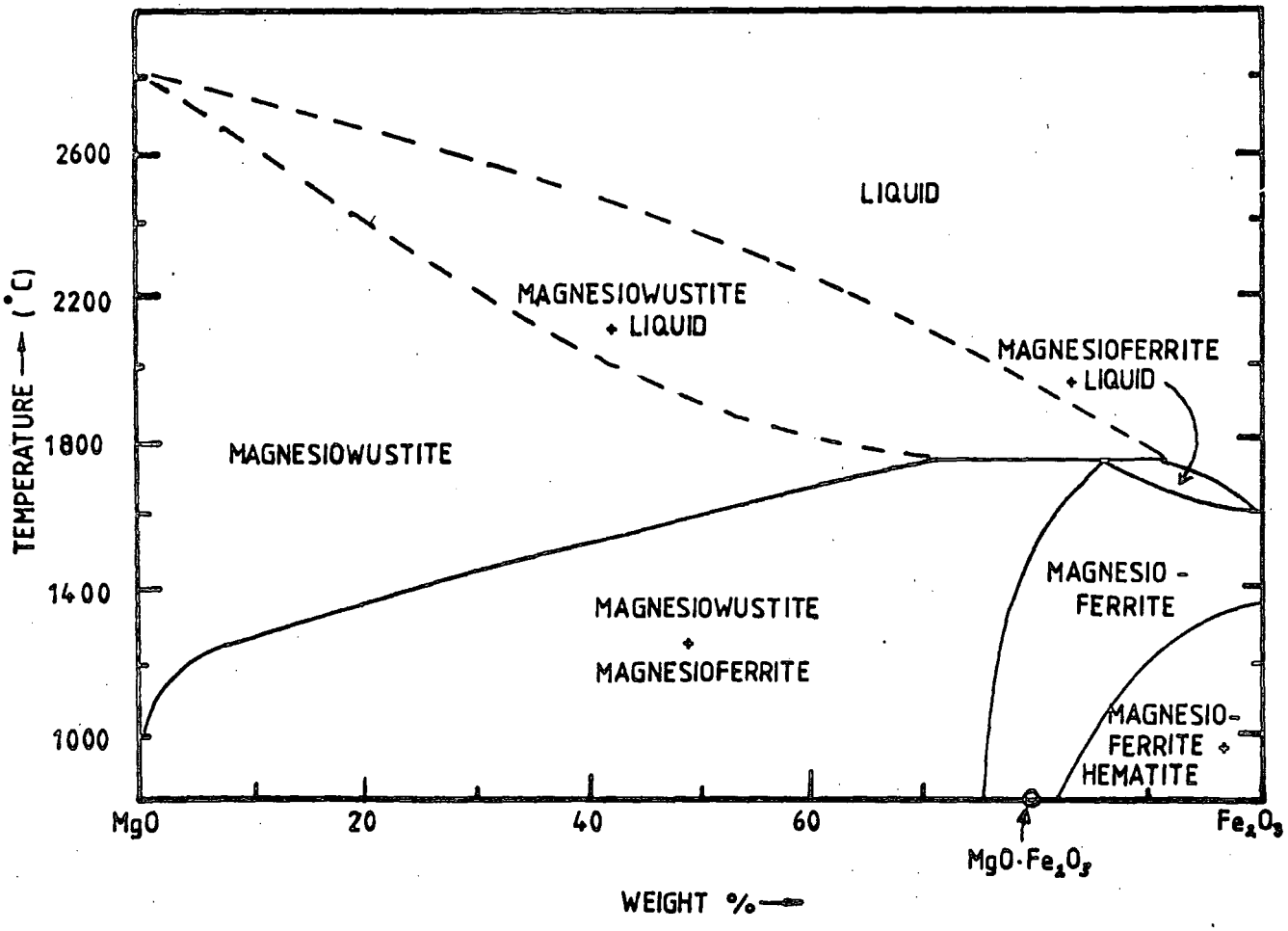

Figure 2.8 Phase Relations in the System Mg - Fe - O (after Phillips et al [43])

construct a spinel-type unit cell, and it was found that energetically the most stable defects considered were large aggregates which modelled a substantial portion of such a unit cell.

2.3 The Spinel Structure.

The spinel structure is based upon the same face-centred cubic lattice of oxygen ions as the magnesium oxide structure, described in Section 2.1. The cations, which are usually divalent or trivalent are packed into the interstices, of which there are 96 in a unit cell. Of these cation sites 64 are tetrahedral, and 32 are octahedral, the symmetry being referred to the neighbouring oxygen ions. Normally only a total of 24 cation sites will be occupied, 8 of these being tetrahedral or 'A' type sites and the remainder octahedral, or 'B' type, sites. A small section of the spinel unit cell is shown in Figure 2.7.

In the case of 'normal' spinel, with a formula typically MeZ_2O_4, where Me is a divalent and Z a trivalent cation, the trivalent ions occupy the B sites and the divalent the A sites. In the inverse spinel structure the B sites are shared equally between the divalent and trivalent cations, the balance of the trivalent ions going to the A sites. Distributions of cations intermediate between normal and inverse do occur, the version of the spinel structure precipitated as magnesioferrite from iron doped magnesium oxide being an example (7,22,this work). The degree of inversion in the magnesioferrite structure depends upon the thermal history of the specimen (7,22).

Since the precipitated magnesioferrite is also thought to be rich in magnesium (5,7,23), a more appropriate chemical formula than

that given above is $Mg_xFe_{(3-x)}O_{4-(x-1)/2}$ where x is slightly greater than one. The reduction in the number of oxygen ions is required to maintain the charge balance.

2.4 The Magnesium Oxide Samples.

The magnesium oxide samples used in this work were grown, by the arc-fusion method, by W. and C. Spicer Ltd. of Cheltenham. When received the crystals ranged in colour from cloudy white (the 4N samples) through transparent (3N) to progressively darker shades of green with increasing dopant concentration. The dopant concentrations, which ranged from 310 to 12900 ppm by weight, were reported by the suppliers to be accurate to within two per cent, having been determined by Johnson, Matthey and Co. (by x-ray fluorescence).

The crystals ranged in size from 0.5 cm x 0.5 cm x 0.3 cm to 1.0 cm x 1.0 cm x 0.5 cm, and were cleaved to provide samples 0.03 cm thick and approximately 0.4 cm x 0.2 cm in area. There were two reasons for using such thin samples. Firstly, it was important that when a sample was inserted into or removed from the furnace that the temperature changes within the sample took place quickly, and as uniformly throughout the sample as was possible. Secondly, it is hoped to correlate this work with future work on the dielectric behaviour of similarily treated samples; and the A.C. bridge which will be used for the low frequency part of that investigation cannot cope with thicker samples of magnesium oxide. Those few samples used for TEM studies had to be very much thinner, so they were heat treated

whilst still 0.03 cm thick and then thinned using standard etch-resist masking and hot orthophosphoric acid.

Although no attempt was made to analyse the total impurity content of the samples, it is highly probable that many impurity species besides iron were present. EPR evidence of Cr^{3+} was found in some samples but as with all magnesium oxide other paramagnetic and non-paramagnetic ions would be expected. As well as those listed in Table 2.1 one would expect OH^- radicals, although these are removed by the solution treatment (42).

It is of interest to note that the Spicer iron doped magnesium oxide studied by Gourdin et al (36) contained fewer other impurities as iron content increased. We have noticed similar behaviour, in that the samples which give the most intense Cr^{3+} EPR signal are the 4N samples, and the next most intense are the 3N samples. It may be that the size difference between the iron and magnesium ions means that the inclusion of a certain amount of iron in the lattice has a stabilizing effect, and that if the iron is not added deliberately other ions are likely to be incorporated to play the same role.

2.5 The Heat Treatment of Samples.

Two different types of heat treatment were carried out on the various samples - a 'solution' treatment and an 'aging' treatment. The solution treatment was an attempt to produce the maximum possible number of isolated Fe^{3+} ions, by heating the samples to a temperature at which the iron oxides would form a solid solution with the MgO and then quenching rapidly to room temperature. According to the phase-relations data of Phillips, Somiya and Muan (43), which are

reproduced in Figure 2.8, for quantities of iron of the order of one per cent or less this should be achieved at temperatures above 1000°C.

At these elevated temperatures one obtains magnesiowustite - Fe_xO dissolved in MgO. The value of x is variable, being maximised by maximising the oxygen partial pressure. Consequently, 'solution' treatments were carried out at 1400°C, for 24 hours, in flowing oxygen. Quenching to room temperature then preserves the high temperature distribution. Reference to Figure 2.8 also shows that annealing at temperatures below 1000°C produces a second phase, magnesioferrite.

The furnace tube used in the solution treatment was of recrystallised alumina, the element being crucilite. The samples were loaded in a platinum boat, and after the appropriate length of time were quenched by pulling quickly to the end of the furnace. Since it has been shown (19) that the rate of cooling can critically affect the iron distribution, experiments were tried with quenching into water, or into liquid nitrogen, in order to speed up the quench rate. . The main outcome of these early experiments was an unacceptably large number of shattered samples.

The aging treatments were also carried out in oxygen at one atmosphere. Since the aging temperatures were in the region of 600 - 800°C a furnace wound with Kanthal A with a silica glass liner was used for these treatments. For aging the samples were loaded in a platinum basket in a silica boat, and they were quenched by pushing rapidly to one end of the furnace, into the stream of cold inflowing oxygen.

CHAPTER 3

Magnetic Resonance : Experimental Details.

3.1 The Spectrometer.

The magnetic resonance measurements were made with a Varian V-4502-15 EPR Spectrometer system, employing a V-153-C klystron operating at about 9 GHz. A schematic diagram of the spectrometer including the arrangement of the microwave components is shown in Figure 3.1. Information regarding the constructional and operational considerations relating to such an instrument may be found in the standard texts: the treatise by C. P. Poole (44) is particularily detailed. It is sufficient here to draw attention to certain features of the system.

The klystron supplies microwave power through an isolator and a variable attenuator to the microwave bridge, which divides the power equally between two arms, one arm (arm 2) terminating in a matched load, and the other (arm 3) leading to the cavity. When the cavity is properly matched no power reaches the detector crystal in arm 4. Since the cavity impedance changes with loading a variable iris is provided to allow matching when different samples, sample holders and dewars are inserted in the cavity. An adjustable slide-screw tuner in arm 2 reflects sufficient power to bias the detector crystal.

The bulk of the EPR, and all of the FMR, measurements were made using a rectangular V-4531 multi-purpose cavity, operating in the TE_{102} mode. To count spins a V-4532 Dual Sample Cavity was

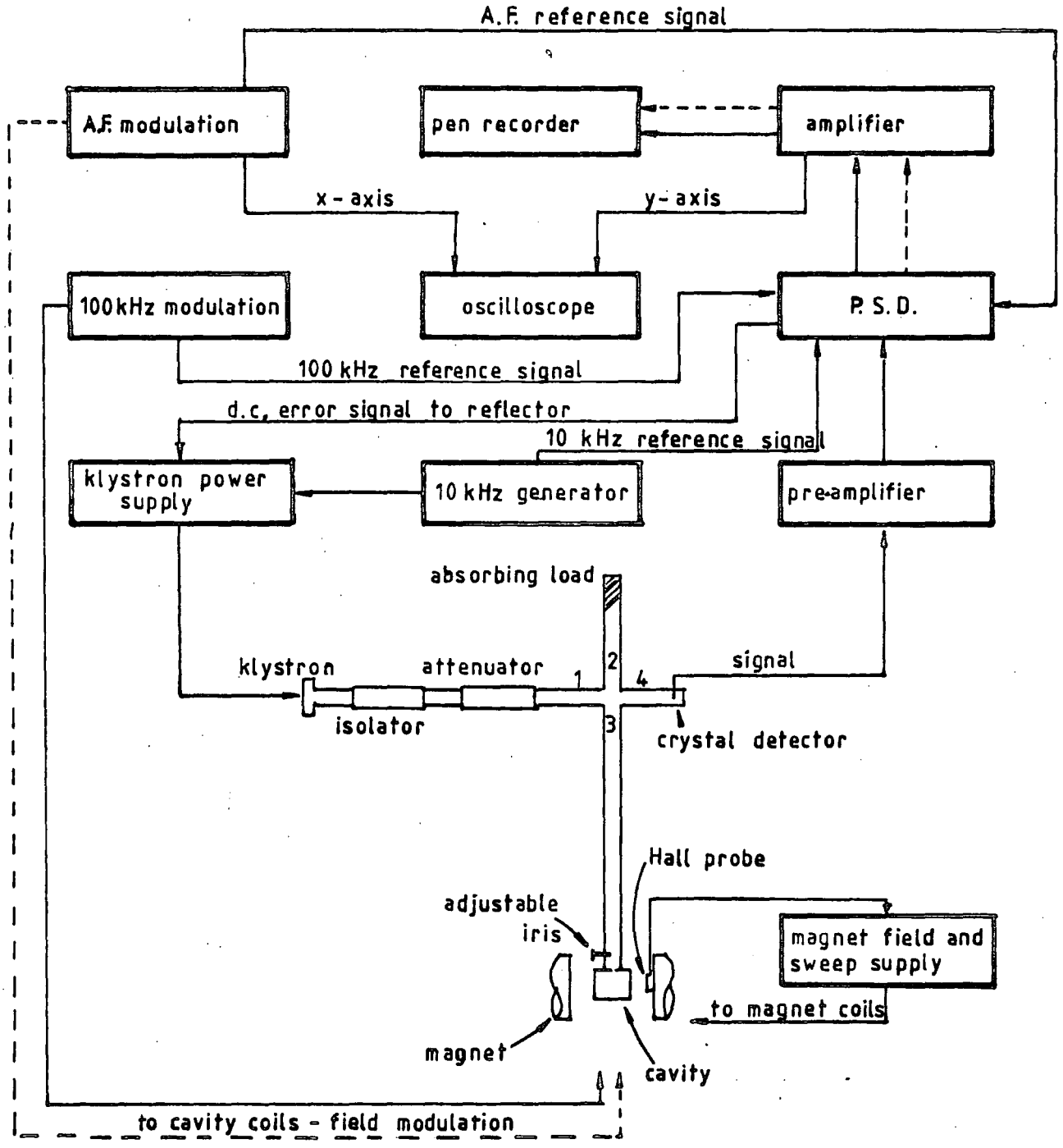

Figure 3.1 Schematic of the Spectrometer System

employed, which was in effect two single rectangular cavities joined end-to-end and operated in a TE_{104} mode. Two samples - one of known and one of unknown spin density - were then positioned at the 1/4 and the 3/4 positions along the cavity length. The resonant frequency of either cavity varied with loading, being particularily affected by the insertion of quartz glass-ware. However the klystron frequency was adjustable, mechanically and electronically, over a small range; and once set to the cavity frequency it was held at that frequency by an automatic frequency control system. The klystron frequency was measured with a Hewlett-Packard X532B frequency meter.

The swept D.C. field was supplied by a V-3603 magnet controlled by a V-FR2503 Fieldial unit, control being established by means of a Hall probe attached to one poleface. The Hall voltage from this probe was continuously monitored automatically and compared with a preset value whose magnitude depended upon the selected field and sweep values. The magnet sweep was calibrated with a Newport Instruments P2 proton magnetometer.

The absorption of power was detected in the change of power reflected from the cavity at resonance. The signal to noise ratio was enhanced by the superposition of a modulation field, of up to a few gauss in value, on top of the D.C. field by means of coils embedded in the cavity walls. A phase-sensitive detection system was then used to detect the absorption signal, which was recorded as a derivative. The dual-sample cavity contained two separate sets of coils, one for each of the samples, and was constructed such that neither sample was affected by the other's modulation field. The two sets of coils in the dual-sample cavity were modulated at different frequencies - one at 400 Hz and one at 100 kHz - allowing the absorption signals from

each sample to be separated, and recorded separately on a two-channel Y - t chart recorder.

To detect weak signals or to initially locate signals it is acceptable to operate with a modulation field of several gauss. However, unless the modulation amplitude is considerably less than the width of the line being detected, the line is broadened. For precise measurements of linewidth the modulation amplitude was set to a suitably small value.

Samples were mounted on a 4 mm. diameter quartz rod which was held in a goniometer attached to the top of the cavity. The sample was attached to a flat machined facet at the bottom of the rod and a second facet at the top of the rod, precisely positioned with respect to the first, allowed alignment of the sample with respect to the field. The sample could then be rotated by means of the geared drive on the goniometer, and positioned to within one half of a degree of any required angle, relative to its initial orientation. It was neccesary when using the V-4557 variable temperature aparatus to replace the rod with a 4 mm. outside diameter quartz tube. The end of the tube was partially plugged and then machined to provide a sample mount. The tube allowed hot (or cold) gas to escape, and at the same time provided an entry point for the thermocouple used to monitor the temperature of the sample.

3.2 Temperature Control.

Sample temperatures in the range 90K - 500K were obtained by means of a V-4557 variable temperature system. The sample was located, on its mounting tube, within a 6 mm bore quartz cavity insert

which carried a stream of dry nitrogen. The nitrogen flowed over a heater and a temperature sensor, both of which were located outside the cavity, before bathing the sample. The sensor was monitored, and the heater controlled, by a V-4540 Temperature Controller which maintained the nitrogen at a preselected temperature.

For temperatures in the range 90K - ambient the nitrogen was first cooled by passing it through a heat exchanger comprising a coiled copper tube, immersed in liquid nitrogen, from which it emerged at a temperature of about 80K. Control of the gas flow-rate and the heater current enabled control of the sample temperature, which was monitored with a copper/constantan thermocouple placed in the cavity adjacent to the sample. As the quartz insert did not provide very efficient insulation it was necccesary when operating at temperatures below ambient to continuously flush the cavity with a stream of dry nitrogen gas, to prevent water condensing in the cavity.

Temperatures in the range 3K - 90K were obtained with an Oxford Instruments ESR9 Continuous Flow Cryostat, in conjunction with a DTC-2 Temperature Controller. Liquid helium was continuously suplied from a storage dewar, via a flexible transfer tube comprising two concentric stainles steel tubes, surrounded by a vacuum jacket. It then passed through a stainless steel capillary tube in the cryostat, emerging just below the cavity as a stream directed onto the sample. The capillary, sample holder and sample were all located within a dewar which was sealed at the top.

After cooling the sample the helium (gas) returned up an outer layer of the transfer tube, thus assisting in cooling the incoming liquid. Coarse temperature control was achieved by regulating the flow of helium. For fine adjustment and automatic

control a copper heat exchanger surrounding the tip of the stainless steel capillary was heated, via the temperature control unit.

CHAPTER 4

EPR : The Theoretical Spectrum of Fe^{3+} in MgO

In order to characterise the starting materials samples with various concentrations of iron were investigated using EPR at X-band (9 GHz). These investigations were carried out on samples in the as-received state, and after they had been solution treated. The spectra gave information regarding the types of paramagnetic impurity present in each sample and also, by comparison with a standard sample of known spin density, the approximate number of isolated Fe^{3+} ions occupying cubic sites. Linewidth measurements on the same samples gave information regarding the interactions between the dopant ions. In Chapter 6 the results are presented, and discussed. This chapter and the next are concerned with the theoretical background relating to the EPR spectra and the expected relative intensity, shape, and width of the spectral lines.

4.1 The Spin Hamiltonian.

The energy of an ion containing unpaired electrons and nuclei with non-zero spin is given (45) by the Hamiltonian operator

$$\hat{H} = \hat{H}(el) + \hat{H}(cf) + \hat{H}(ls) + \hat{H}(ss) + \hat{H}(ze) + \hat{H}(hf) + \hat{H}(zn) + \hat{H}(nn) + \hat{H}(q)$$

where the terms represent various contributions to the energy of the

electron, as follows :-

$\hat{H}(el)$: the kinetic energy, and the electronic and nuclear potential energies of the electron.

$\hat{H}(cf)$: the splitting and shifting of the energy levels of the electron by the crystal field due to the surrounding ions.

$\hat{H}(ls)$: the spin-orbit coupling term.

$\hat{H}(ss)$: the spin-spin interaction term between electrons.

$\hat{H}(ze)$: the Zeeman splitting of the electronic levels due to an externally applied magnetic field.

$\hat{H}(hf)$: the hyperfine interaction between the electrons and the spin of their own nucleus.

$\hat{H}(zn)$: the nuclear Zeeman term.

$\hat{H}(nn)$: the spin-spin interaction between adjacent nuclei.

$\hat{H}(q)$: the quadrupole energy term.

Fortunately we may discard some of these terms, as far as EPR spectroscopy is concerned, because the energies involved are many orders of magnitude too large to be detected by this method; for example, the crystal field splitting term is detected by optical

spectroscopy. Other terms may be ignored for the particular case with which we are concerned; for example, the hyperfine term will contribute little to the Fe^{3+} spectrum as the Fe^{57} nucleus with the non-zero spin necessary to provide an interaction with the electron is only 2.4 per cent abundant, and therefore has negligible effect. In fact one would expect for this case, of Fe^{3+} in cubic sites, to be able to ignore, to a first approximation, all but the Zeeman term and to write the Hamiltonian as

$$\hat{H} = g \beta \bar{H}.\bar{S}$$

where S is the effective spin, H is the applied field, β is the Bohr magneton, and g the spectroscopic splitting factor. This would yield a spectrum comprising a single isotropic line, at a field strength appropriate to the single free-electron g-value of g = 2.0023.

However, although the spin does not interact directly with the crystal field the degeneracy of the levels of the $^6S_{5/2}$ state is partially lifted (by interactions which involve the crystal field and spin-orbit interactions of excited states which are admixed to a small extent with the ground state) to give one two-fold and one four-fold degenerate level (46,47). This interaction is taken into account by the inclusion of an additional term in the effective spin Hamiltonian, which is written (11) as

$$\hat{H} = g \beta \bar{H}.\bar{S} + 1/6\ a\ (S_x^4 + S_y^4 + S_z^4 - 1/5(S(S+1)(3S^2 + 3S - 1)))$$

Here S is the effective spin; S_x is the projection of S on the x-axis, etc; and 3a is the zero-field splitting parameter, whose magnitude and sign are both determined experimentally.

Since the orbital quenching is not complete, the g-factor for the 3d series transition-metal ions usually departs from the free-electron value. In the case of the $3d^5$ ions this departure is small, since the ground, S, state has no orbital moment, and shift of g-value is brought about only through the admixture of higher energy terms into the ground state term (48).

4.2 The Zeeman Energy Levels, and Transitions.

The variation of the energy levels with applied magnetic field for the case of the $^6S_{5/2}$ ion in octahedral symmetry has been evaluated by Debye (49), and by Kronig and Bouwkamp (50). To a good approximation the levels are given, for reasonably high values of applied field, by the expressions listed in Table 4.1. Since values of g and a have been determined experimentally (11) it is possible to plot the levels and their variation with applied field, for any direction of applied field. This is illustrated in Figure 4.1 where the levels are plotted for the case in which the field is applied along a ⟨100⟩ direction.

Besides the transitions for $\Delta m_s = 1$ reported by Low, transitions for $\Delta m_s = 3$, 4 and 5 have been investigated and reported by Kolopus and Holroyd (51). In addition, de Biasi (52) has investigated the transitions for $\Delta m_s = 2$ which are forbidden when the applied field is in a ⟨100⟩ direction, but allowed for other orientations. At X-band however fields of 2 kilogauss and greater are sufficient to exclude all but those transitions for which $\Delta m_s = 1$. This spectrum comprises five lines only, the transition energies being given in Table 4.2, and the positions of the transitions for microwave

TABLE 4.1 : Energy levels of $^6S_{5/2}$ state ion in an octahedral site, and strong magnetic field (49,50).

Level	Energy
$\pm \frac{5}{2}$	$\pm \frac{5}{2} g\beta H + \frac{1}{2} pa \pm (212-24p-113p^2)\,(a^2/240\, g\beta H)\ldots$
$\pm \frac{3}{2}$	$\pm \frac{3}{2} g\beta H - \frac{3}{2} pa \pm (12 + 8p - 15p^2)\,(a^2/16\, g\beta H)\ldots$
$\pm \frac{1}{2}$	$\pm \frac{1}{2} g\beta H + pa \pm (-2 - 3p + 5p^2)\,(a^2/3\, g\beta H)\ldots$

where $p = 1 - 5(\ell^2 m^2 + m^2 n^2 + n^2 \ell^2)$; and ℓ, m, n are direction cosines of applied magnetic field, with respect to the fourfold crystal axis.

TABLE 4.2 : Transition Energies and relative intensities for $\Delta m_s = 1$

Transition	Transition Energy	Relative Intensity
$\frac{5}{2} \leftrightarrow \frac{3}{2}$	$h\nu = g\beta H + 2pa + (2-9p+7p^2)\,(a^2/15 g\beta H)$	5
$\frac{3}{2} \leftrightarrow \frac{1}{2}$	$= g\beta H - \frac{5}{2} pa + (68+72p-125p^2)\,(a^2/48 g\beta H)$	8
$\frac{1}{2} \leftrightarrow -\frac{1}{2}$	$= g\beta H + (-2-3p+5p^2)\,(2a^2/3 g\beta H)$	9
$-\frac{1}{2} \leftrightarrow -\frac{3}{2}$	$= g\beta H + \frac{5}{2} pa + (68+72p-125p^2)\,(a^2/48 g\beta H)$	8
$-\frac{3}{2} \leftrightarrow -\frac{5}{2}$	$= g\beta H - 2pa + (2-9p+7p^2)\,(a^2/15 g\beta H)$	5

TABLE 4.3 : Some of Van Vleck's dipolar line broadening data (71).

Substance	Linewidths $\Delta H_{\frac{1}{2}}$ (gauss)	
	Experimental	Calculated
$MnCl_2.4H_2O$	1,410	1,530
$MnCl_2$	750	2,950
$MnSO_4.4H_2O$	1,150	1,560
$MnSO_4$	665	3,520
$Mn(NO_2)_2.6H_2O$	1,210	1,033
MnF_2	470	7,020

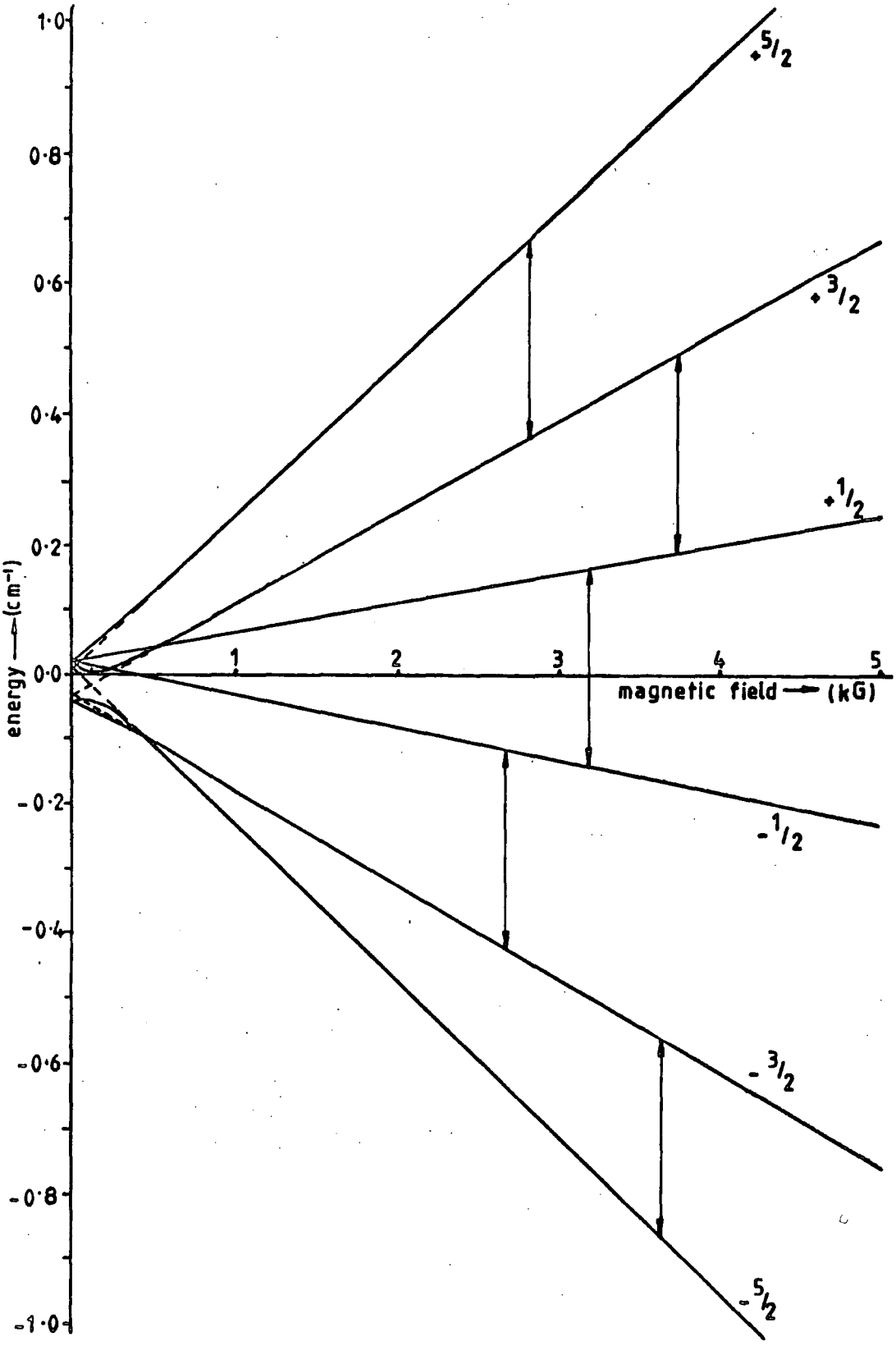

Figure 4.1 Zeeman Levels for $^6S_{5/2}$ State, H//⟨100⟩
Transitions for Fe^{3+} in cubic sites in MgO (at 9.1 GHz)

frequencies of 9.1 GHz being shown on Figure 4.1.

As all these lines are allowed whatever the orientation, the spectrum has the same form for all directions of applied field. However the outer pairs of lines are highly anisotropic, varying in position with rotation of the crystal in a way which reflects the symmetry of the crystal field. This anisotropy is illustrated in Figure 4.2 which shows the computed isofrequency plot for a rotation of 90 degrees in a {100} plane, the microwave frequency being 9.1 GHz. This theoretical isofrequency plot is symmetrical about the [110] direction in this plane, as a result of the assumption of perfect cubic symmetry; in practice it would seem that there is a slight perturbation of this symmetry.

The relative intensities of the absorption lines follow from the square of the matrix elements, which is

$$S(S + 1) - m(m - 1)$$

for the transition $m \longrightarrow (m - 1)$. The relative intensities have been given along with the other data in Table 4.2. However the actual intensities of the lines will be dictated by a Maxwell- Boltzman distribution of the form

$$N(1)/N(2) = \exp - (\Delta E/kT)$$

where N(1) and N(2) are the populations of the levels involved, and ΔE is their energy separation. Since at very low temperatures the 1/T term will start to dominate it is possible, by working at helium temperatures to determine the order of the transitions, and hence the sign of a (53).

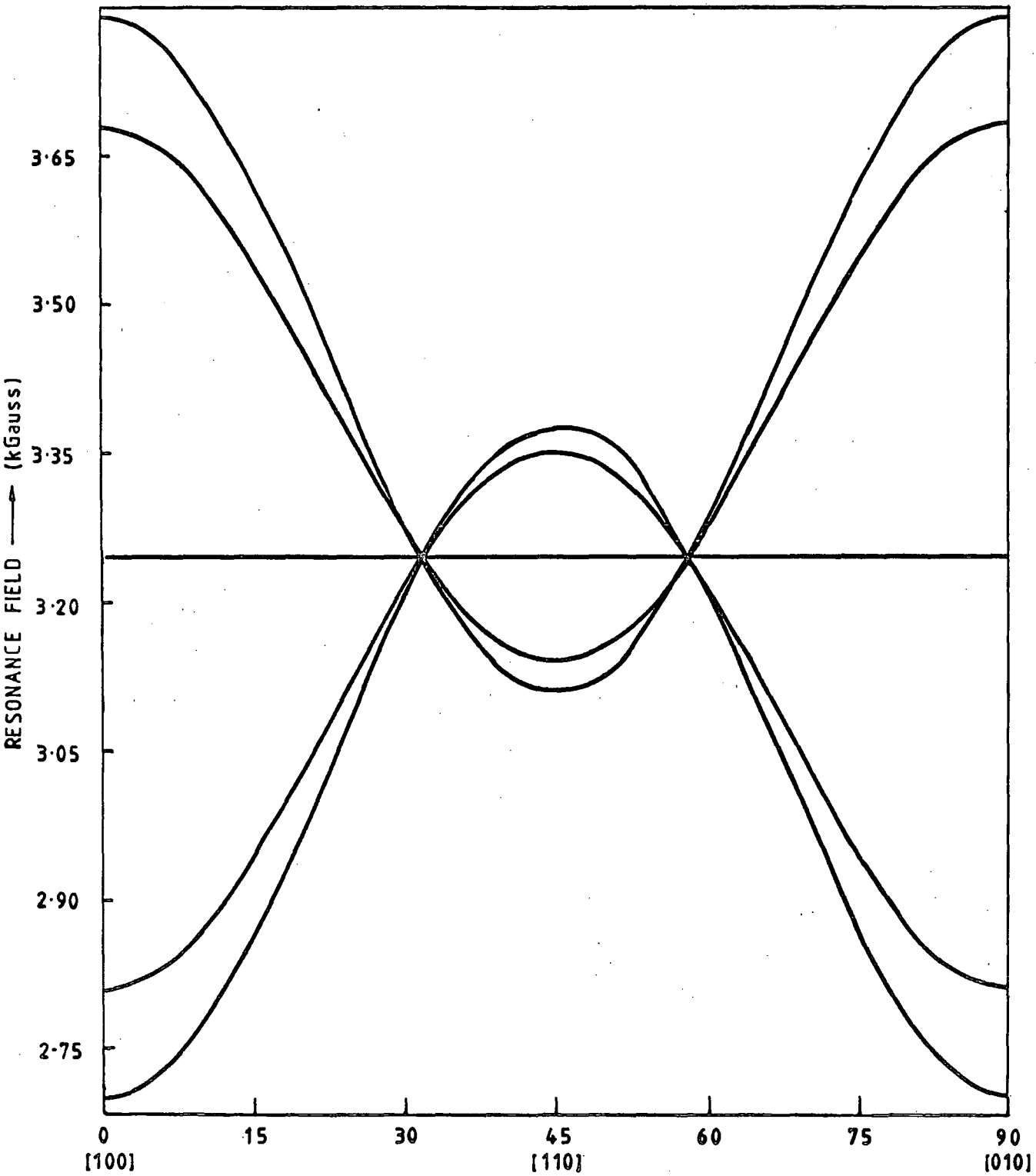

Figure 4.2 Computed Isofrequency Plot : Fe^{3+}/MgO : 9·1 GHz : H in (001) plane

4.3 The Widths of EPR Spectral Lines.

The widths and shapes of EPR spectral lines are of interest because they provide information regarding the interactions taking place between the magnetic ions and their surroundings. The 'intrinsic' width of the line related to a transition between two states is governed by the lifetime of the spin in the upper state to which the transition takes place; and this in turn is affected by the type of relaxation processes which maintain the equilibrium of the two levels. However, provided one does not drastically alter the populations by saturating the resonance, one may regard this contribution to the linewidth as being negligible in comparison with other contributions.

Mechanisms which can affect the linewidth and lineshape may be classified in two groups - those which broaden the line homogenously and those which broaden it inhomogenously. Sources of inhomogenous broadening include unresolved structure; inhomogeneity in the applied field; and mosaic structure and/or internal strains within the crystal. These effects all result in a spectral line which is really merely an envelope containing more than one, narrower, spin packet, as is illustrated in Figure 4.3. It is assumed that inhomogenous sources of broadening are negligible for the samples examined here, and no further reference is made to this type of mechanism. Homogenous mechanisms which are likely to come into play include, besides the spin-lattice relaxation already mentioned, spin-spin interactions such as dipolar and exchange effects; motion of unpaired spins in the field; and the diffusion of excitation throughout the sample. All these mechanisms, and the ways in which

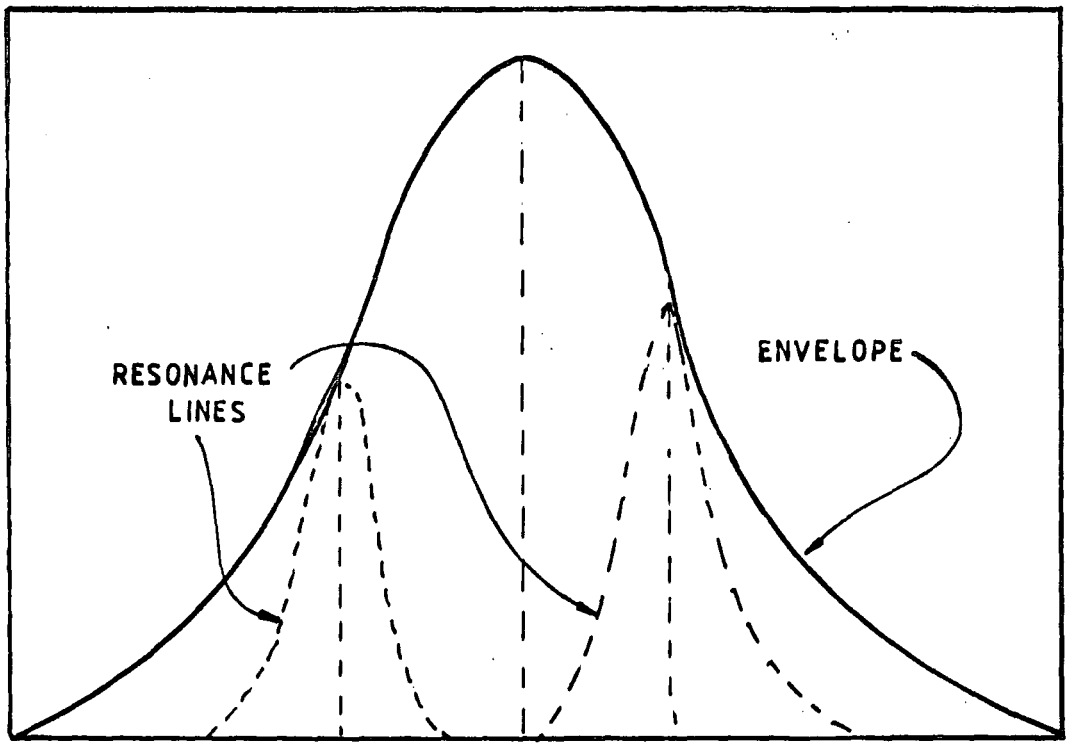

Figure 4.3 Inhomogenous Broadening - envelope is recorded

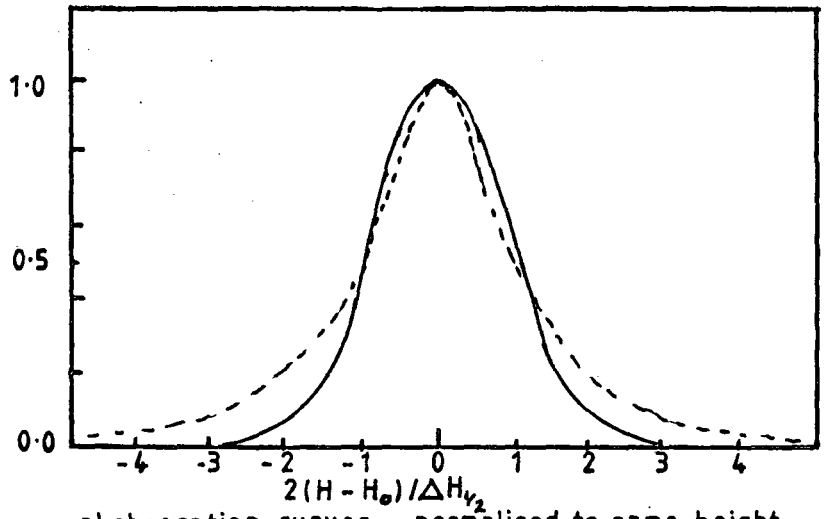

a) absorption curves - normalised to same height

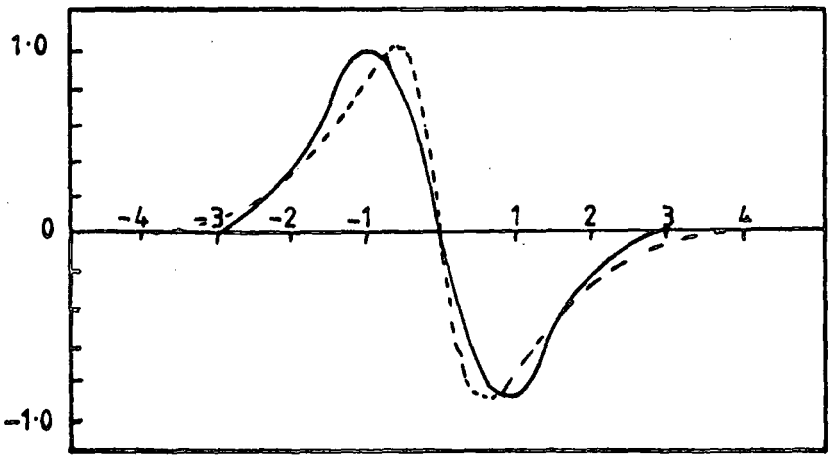

b) derivative curves - normalised to same peak-peak amplitude

Figure 4.4 Typical Gaussian and Lorentzian curves: same width at half-height in this case.
Gaussian ——
Lorentzian - - - -

they arise, are discussed at length in the standard texts (40,54). We will consider only those which are expected to have an appreciable effect on the linewidths of the samples investigated - the dipolar and the exchange effects, both of which are interactions between the spins of the paramagnetic ions.

Expressions have been derived in the literature by various workers (55 - 59) which enable one to determine the expected effects of these interactions upon the width and shape of spectral lines. As the model due to Van Vleck has been used on several occasions recently to derive data relating to magnesium oxide doped with paramagnetic ions, for comparison with experiment (16,60,61), it is important to comment briefly on the applicability of this model.

As the spins precess about the applied field each will have associated with it a magnetic moment oriented with respect to the applied field. The magnetic field which any one dipole sees is the sum of the applied field and the fields due to all the other dipoles in the sample. Because of the numbers of spins involved this would be a difficult effect to quantify, were it not for the fact that the interaction reduces with distance as the inverse of the sixth power of the distance - and consequently one need only sum over a few shells of relatively near neighbours, for any one ion. The outcome of applying Van Vleck's model is that the dipolar interaction is expected to broaden the line, and render it Gaussian in shape. One further consequence is that the linewidth is expected to change with concentration of paramagnetic impurity ions, increasing as the square root of the concentration.

The exchange interaction is different, in origin and effect. It arises from the electrostatic energy due to the overlap of the

electron shells of neighbouring ions. Where paramagnetic ions are not nearest neighbours - being separated by waters of hydration, for example - then their shells will no longer overlap. However, it is possible that an exchange-type interaction can still take place between them by the mechanism of superexchange (62) via the electron shells of the intervening diamagnetic ion. The effects of exchange on linewidth, and the dependence of these effects on the concentration of paramagnetic species are illustrated by some of Van Vleck's data which are listed in Table 4.3.

It can be seen from the experimental values in this table that where the paramagnetic species are concentrated the line is considerably narrower than one would expect from the effects of dipolar broadening alone. However, since the exchange interaction decreases with distance even more rapidly than does the dipolar interaction, only a relatively small amount of dilution is sufficient to remove most of the narrowing.

It is also demonstrated by Van Vleck that exchange narrowed lines are expected to be Lorentzian rather than Gaussian in the centre, although they remain Gaussian in the wings. In each of the cases where the Van Vleck model has been applied to lightly doped magnesium oxide samples (16,60,61), the linewidths calculated have turned out to be larger - in some cases two orders of magnitude larger - than the experimental linewidths. Since in addition the experimental lines have turned out to be Lorentzian rather than Gaussian, it has been suggested that exchange narrowing is a dominant mechanism. This is difficult to visualise for the dopant concentrations used in the reported investigations (typically 100 - 1000 ppm by weight), if the dopant is homogenously distributed,

since even the superexchange mechanism is limited in range to the interaction between next nearest neighbours; and one does not expect to find loosely bound hydrogenic-like states in ionic insulators, as may arise in doped semiconductor materials.

The problem arises because this is essentially a misuse of the Van Vleck model, which is based on the assumption that each ion interacts through the dipolar mechanism with a large number of others. For systems as magnetically dilute as the magnesium oxide in question this assumption does not apply. If one considers that the dipolar interaction will be effective only over a distance of one or two unit cells, and assumes that the effect of any non-random clustering will be to alter the energy of the spins concerned to such an extent that they do not contribute to the cubic site spectrum, then clearly many of the ions will be magnetically isolated. Most others will have very few magnetic neighbours, located randomly on lattice sites in the immediate vicinity.

The problem of the randomly populated dilute magnetic lattice has been tackled in a variety of ways, by various workers. Here the approach due to Kittel and Abrahams (57) - which is essentially a development of the original Van Vleck model - is used, as it has been shown (17) to provide a reasonable fit with experimental results.

4.4 The Kittel and Abrahams Model.

Both Van Vleck, and Kittel and Abrahams, start from the same premises, with a Hamiltonian comprising

$$\hat{H} = \hat{H}(\text{Zeeman}) + \hat{H}(\text{exchange}) + \hat{H}(\text{dipolar})$$

Provided that the Zeeman energy is large compared with the exchange and dipolar terms one may derive expressions for the second and fourth moments of the expected absorption line in terms of the effective spin, the g-value, the 'spin lattice' constant, and the direction cosines of the applied field relative to the principal crystallographic axes. It is reasonable to work in terms of a spin lattice rather than the actual lattice constant, since only those ions which have non-zero spin will contribute to the broadening in this case.

If one follows the Van Vleck model then it is found that the exchange term does not contribute to the second moment of the line, although it does contribute to the fourth moment. It is for this reason that a lineshape which approximates a Lorentzian rather than a Gaussian is often taken to imply exchange narrowing, since the nett effect of adding to the fourth moment of the line and not the second is to enhance the wings at the expense of the centre.

Kittel and Abrahams find for their second moment term

$$\langle \Delta\nu^2 \rangle = \left[S(S+1)/3\hbar^2 \right] f \sum_k B_{jk}^2 \qquad 4.1$$

where ν is in frequency units, f is the probability of occupation of a

lattice site k, and

$$B_{jk} = -3g^2\beta^2 r_{jk}^{-3}\left[\tfrac{3}{2}\gamma_{jk}^2 - \tfrac{1}{2}\right] \qquad 4.2$$

The separation of the interacting ions is given by r, γ is the direction cosine of $\underline{r}_{jk}$ with respect to the static field, and h, g and β have their usual meanings. For a simple cubic lattice with the applied field in a $\langle 100 \rangle$ direction the fourth moment is, in terms of the second moment,

$$\langle \Delta\nu^4 \rangle = 3\left[\langle \Delta\nu^2 \rangle\right]^2 \times \left\{.742 + f^{-1}\left[.098 - .021(S^2 + S)^{-1}\right]\right\} \qquad 4.3$$

If all sites are occupied - i.e. f = 1 - this leads to the equivalent Van Vleck equation. For an effective spin of S = 1/2 the term in the curly brackets approximates to 1, and so the lineshape approaches Gaussian, for a dopant concentration of $f > 0.1$. If $f < 0.01$ then the line departs markedly from Gaussian: but this clearly cannot be a result of exchange narrowing, since the smaller the concentration the greater will be the departure.

In Chapter 5 it is shown that the relationship between the linewidth and the second and fourth moments is given by

$$\Delta H_{ms} = \sqrt{\frac{\langle \nu^2 \rangle^3}{\langle \nu^4 \rangle}} \cdot \frac{\pi}{3} \cdot \frac{\partial H}{\partial \nu} \quad \text{kG}$$

where ΔH_{ms} is the linewidth between points of maximum slope, f is the probability of occupation of a lattice site by a dopant ion, and $\partial H/\partial \nu$ is determined from the isofrequency plot. As the dopant species in question are expected to substitute on the cation sites only, f is effectively the cation site fraction i.e. the ratio of the number of

cation sites occupied by dopant ions to the total number of cation sites.

When the expressions for the moments are evaluated we find that for the samples considered in this study we may write the relationship between linewidth and dopant concentration (see Chapter 5) as

$$\Delta H_{ms} = 20.39\ f \quad kG \qquad 4.4$$

when the static field is applied along a $\langle 100 \rangle$ direction. Although some of the samples referred to here are the same as those which were the subject of a recent publication on linewidth studies (17) the figures arrived at here for the relationship between dopant concentration and both the second moment and the width of the line are a little different from the published ones. There are two reasons for this. The published values were arrived at by assuming in the first place that the Kittel and Abrahams calculated formulae for both the fourth moment and the linewidth in terms of the second moment would be a reasonable approximation for a face centred cubic lattice, although they were derived for a simple cubic case; and they were arrived at by summing the electronic interactions over a total of eight unit cells, as had been done on many previous occasions.

In this thesis the fourth moments are calculated using the Kittel and Abrahams approximation

$$\langle \Delta\nu^4 \rangle = \left[\frac{S(S+1)}{3h^2}\right]^2 \left[-\tfrac{3}{2} g^2 \beta^2\right]^4 f \sum_k \left[r_{jk}^{-3}(3\gamma_{jk}^2 - 1)\right]^4$$

and many of the cation sites in the next 'layers' of atoms around the

unit cell have been included in the summation. The nett effect of these changes is to increase the accuracy of the calculation; and in fact to bring the calculated values closer to the experimental values.

4.5 The Shapes of EPR Spectral Lines.

The two 'extremes' of shape - Gaussian and Lorentzian - are shown in Figure 4.4, normalised to the same maximum amplitude. The derivatives of the two are also shown, normalised to the same amplitude at the peaks. The width may be assessed either as the width at half the maximum amplitude ($\Delta H_{\frac{1}{2}}$) or as the width between points of maximum slope (ΔH_{ms}). It is simpler in practice to deal with the latter since this is the peak-to-peak separation of the derivative, and so is easily measured experimentally.

Because the moments of the line, measured about the centre frequency, depend upon the shape, the calculation of the line moments gives information relating to the expected line shape. If the lines are symmetrical the odd moments disappear; but the second and fourth moments are calculable. For a Gaussian line the relationship between the two is given (63) as

$$\frac{\langle \Delta \nu^4 \rangle^{1/4}}{\langle \Delta \nu^2 \rangle^{1/2}} = 1.32$$

For a Lorentzian line the even moments are not strictly obtainable, as they theoretically go to infinity. However, if one truncates the line at a reasonable distance from the centre frequency then this gives a very good approximation. If the Kittel and Abrahams scheme is followed and the line truncated at $\nu = \nu_0 \pm \alpha$ where ν_0 is the centre frequency and

$\alpha \gg \frac{\Delta H_{1/2}}{2}$ then one arrives at the expression

$$\frac{\langle \Delta\nu^4 \rangle^{1/4}}{\langle \Delta\nu^2 \rangle^{1/2}} = \frac{\pi \alpha}{3 \Delta H_{1/2}}$$

Even though we have defined the truncation point this ratio is still variable, since it depends upon the reciprocal of the linewidth which in turn depends upon the concentration of paramagnetic impurity. We should note that consequently we will expect the shape of the line to vary with concentration - as we go to weaker and weaker concentrations we expect the line to become more peaked in the centre and more spread in the wings - i.e. 'more Lorentzian'.

For the range of concentrations with which this study is concerned the cation site fraction of dopant, f, varies from approximately 0.01 - 0.0001, giving for $\alpha = 5\Delta H_{1/2}$ theoretical ratios of moments varying from 1.64 - 5.18. Hence we expect a Lorentzian line in every case.

CHAPTER 5

EPR : Linewidths, Lineshapes and Impurity Concentration

5.1 The Second Moments Equation

In general we expect both lineshape and linewidth to be dependent upon the effective spin, the concentration of paramagnetic impurities, and the symmetry of the 'spin lattice'. Kittel and Abrahams start from the same point as Van Vleck but derive an expression for the mean deviation of resonance frequency from the centre frequency, for the case of interaction between like ions, of

$$\langle \Delta\nu^2 \rangle = \left[\frac{S(S+1)}{3h^2}\right] f \sum_k B_{jk}^2 \qquad 5.1$$

where $\langle \Delta\nu^2 \rangle$ is the second moment of the line, in (frequency)^2 units, S is the effective spin of the paramagnetic ion, f is the cation site fraction and

$$B_{jk} = -\frac{3}{2} g^2 \beta^2 \; r_{jk}^{-3}(3\gamma_{jk}^2 - 1) \qquad 5.2$$

Here r is the separation of ion k from ion j, γ is the direction cosine of $\underline{r}$ with respect to the applied magnetic field direction, and g and β have their usual meanings.

Because of the dependence of B_{jk}^2 on r_{jk}^{-6}, the effect of the interaction decreases rapidly with distance from the central ion j. The sum $\sum_k$ which is strictly over all lattice sites in the sample is therefore restricted to a few shells of neighbouring cations. However because of the angular dependence of the sum term it is not sufficient

merely to consider the distance from the central ion when deciding which lattice sites should be included: direction relative to applied field is also taken into account.

Combining equations 5.1 and 5.2 we may write

$$\langle \Delta\nu^2 \rangle = \frac{3}{4} S(S+1)\left[\frac{g^2\beta^2}{h}\right]^2 f \sum_k r_{jk}^{-6}(3\gamma^2 - 1)^2 \qquad 5.3$$

The right hand side of this expression comprises three distinct components - an atomic component in S, g, β and h; a concentration component f; and the sum term in r and γ which is a lattice-dependent component. The atomic and concentration components may be evaluated simply, if we know the characteristics of the paramagnetic ions and their concentrations.

5.2 The Lattice Site Summation

There are different ways of dealing with the sum term. One approach, outlined by Thorp et al. (16), expands the cosine term in Legendre polynomials i.e.

$$\sum_k r_{jk}^{-6}(3\gamma^2 - 1)^2 = \sum_k r_{jk}^{-6}\left[\frac{72}{35}P_4(\gamma) + \frac{8}{7}P_2(\gamma) + \frac{4}{5}P_0(\gamma)\right] \qquad 5.4$$

where $P_n(\gamma)$ is the Legendre polynomial of n^{th} order. If we then define the orientations of the applied field, and the vector $\underline{r}_{jk}$ with respect to the axes of symmetry of the crystal, through θ_H, ϕ_H and θ_k, ϕ_k respectively, as shown in Figure 5.1, we can employ the Addition Theorem for Spherical Harmonics (64) to write

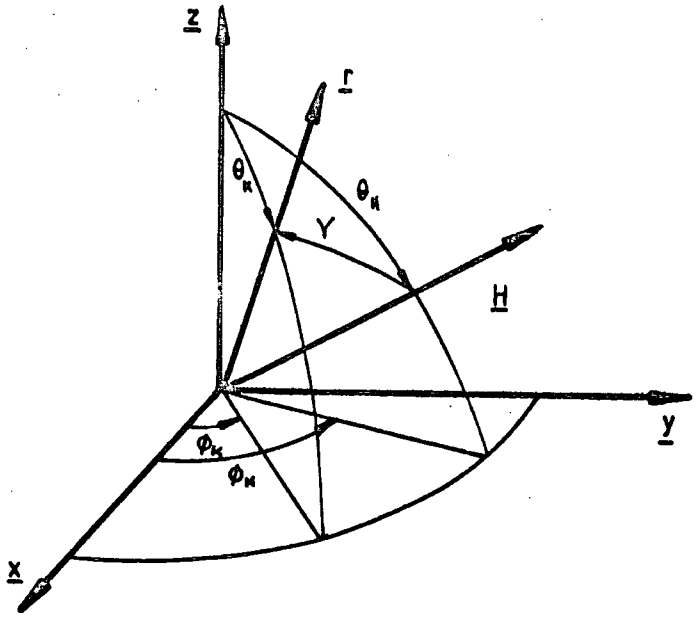

Figure 5.1 Lattice Site Vector $\underline{r}$ and Static Field Vector $\underline{H}$ referred to crystal axes $\underline{x},\underline{y},\underline{z}$

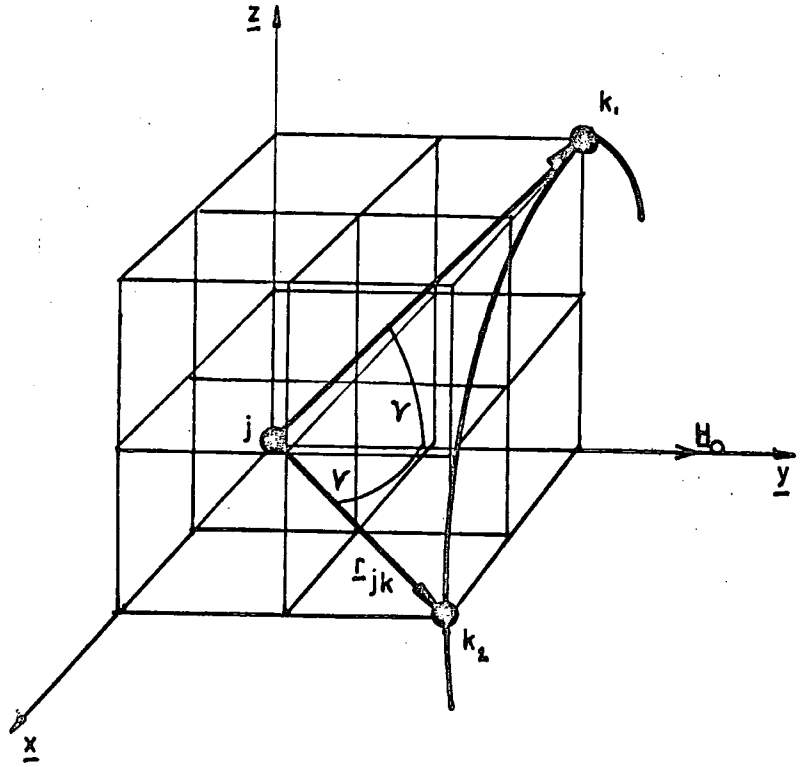

Figure 5.2 Illustrates how ions in symetrically similar sites k_1, k_2 are identical with respect to ion j, when $H_0 \parallel \langle 100 \rangle$

expression 5.4 in terms of spherical harmonics, $Y_n^{\pm m}$, as

$$\left.\begin{aligned}\sum_{k} r_{jk}^{-6}(3\gamma^2-1)^2 = \sum_{k} r_{jk}^{-6}\Big\{&\tfrac{32}{35}\pi\Big[Y_4^{-4}(\theta_k,\phi_k)Y_4^{-4*}(\theta_H,\phi_H) + Y_4^{4}(\theta_k,\phi_k)Y_4^{4*}(\theta_H,\phi_H) \\ &+ Y_4^{0}(\theta_k,\phi_k)Y_4^{0*}(\theta_H,\phi_H)\Big] \\ + \tfrac{32}{35}\pi(Y_2^0(\theta_k,\phi_k)Y_2^{0*}(\theta_H,\phi_H)) &+ \tfrac{16}{5}\pi(Y_0^0(\theta_k,\phi_k)Y_0^{0*}(\theta_H,\phi_H))\Big\}\end{aligned}\right\} 5.5$$

All terms in m=odd have been omitted here, as they disappear upon evaluation. For cubic symmetry, which is the case in question, we may also expect zero contributon from the terms in Y_2^0 (65). If we now subtitute for the spherical harmonics using

$$Y_n^{\pm m}(\theta,\phi) = \sqrt{\frac{(2n+1)(n-m)!}{4\pi(n+m)!}}\, P_n^m(\cos\theta)e^{\pm im\phi} \qquad 5.6$$

where $P_n^m(\cos\theta)$ are the associated Legendre polynomials, then after collecting terms we obtain

$$\begin{aligned}\sum_{k} r_{jk}^{-6}(3\gamma^2-1)^2 = \sum_{k} r_{jk}^{-6}\Big\{&\tfrac{4}{5} + \tfrac{72}{35}P_4(\cos\theta_k)P_4(\cos\theta_H) \\ &+ \tfrac{144}{35}P_4^4(\cos\theta_k)P_4^4(\cos\theta_H)\cos 4(\phi_H - \phi_k)\end{aligned} \qquad 5.7$$

This is a more general expression than that published previously for the lattice sum over the MgO lattice (16) since by retaining the term in $\cos 4(\phi_H - \phi_k)$ we retain sufficient information to allow the evaluation of the sum for any direction of applied field, and not merely for any direction within a $\{100\}$ plane.

Since the associated Legendre polynomials are tabulated we may calculate the sum, and thence from equation 5.3 the second moment of the line. However this information by itself is insufficient to allow us to draw any conclusions regarding the linewidth: we must have

in addition some knowledge of shape. (If the Van Vleck approach were applicable and the line assumed to be Gaussian then since the relationship between second moment and linewidth is known the width may be deduced directly from the second moment.)

The required knowledge may be obtained by calculation of the fourth moment of the line using the Kittel and Abrahams (57) approximation for any moment of

$$\langle \Delta \nu^{2n} \rangle = \left[\frac{S(S+1)}{3h^2}\right]^n \left[-\frac{3}{2} g^2\beta^2\right]^{2n} f \sum_k \left[r_{jk}^{-3}(3\gamma^2 - 1)\right]^{2n} \ldots\ldots \qquad 5.8$$

$$n = 1,2,3,\ldots.$$

For the fourth moment we write n = 2.

If we now pursue an evaluation of the fourth moment via the spherical harmonics approach however, the summation term becomes somewhat complicated. As we only require a measure of linewidth for samples of each concentration we can simplify matters by considering only the special case in which the applied field is directed along a $\langle 100 \rangle$ axis. Then since

$$\gamma = \cos\theta_H \cos\theta_k + \sin\theta_H \sin\theta_k \cos(\phi_H - \phi_k)$$

we find in this case

$$\gamma = \cos\theta_k$$

which reduces the expression for moments of any (even) order to

$$\langle \Delta \nu^{2n} \rangle = \left[\frac{S(S+1)}{3h^2}\right]^n \left[-\frac{3}{2} g^2\beta^2\right]^{2n} f \sum_k \left[r_{jk}^{-3}(3\cos^2\theta_k - 1)\right]^{2n} \qquad 5.9$$

This equation is not merely simpler to handle, but gives clearer

physical insight into the interactions than does the general expression of 5.8. It can be seen that all information relating to ϕ_k has now disappeared: Figure 5.2 illustrates why. It is clear from this diagram that the ions may be grouped into sets of sites such that the ions k in any one type of site are all at the same distance $\pm\underline{r}_{jk}$ from the central ion j: and the vector $\underline{r}_{jk}$ sweeps out a cone of semi-angle θ_k. Since both $\underline{r}_{jk}$ and $\cos\theta_k$ are raised to even powers ions at $+\underline{r}_{jk}$ have the same effect on the central ion j as ions at $-\underline{r}_{jk}$.

We have earlier commented upon the effect the combination of r_{jk} and $\cos\theta_k$ may have; ions located on the surface of cones of very small semi-angle can have a larger effect than ions at closer sites which subtend larger values of θ_k. Perhaps the most surprising aspect of this angular dependence is that for

$$3\cos^2\theta_k = 1 \qquad \text{i.e. for } \theta = 54.74^\circ$$

the sum term, and therefore the contribution to the second moment, collapses to zero. This implies that ions in the $\langle 111 \rangle$ directions from the central ion make no contribution to the line broadening, no matter how close to the central ion they may be. Consequently, a simple cubic and a body-centred cubic spin lattice with the same lattice parameters would yield very similar results for the summation, and ultimately for the theoretical linewidth, even though the body centred spin lattice contained twice as many occupiable sites per spin lattice unit cell.

The dependence upon distance and angle can be seen from the figures of Table 5.1, where the contributions to the summation from

TABLE 5.1 : Lattice Site Contributions to the Lattice Summation.

		No. of sites	Second Moment Terms.		Fourth Moment Terms.	
r_{jk}	γ	N	$\times 10^{-45}$ (cm^{-6}) Nr^{-6}	$Nr_{jk}^{-6}[3\cos^2\gamma-1]^2$ $\times 10^{-45}$ (cm^{-6})	Nr_{jk}^{-12} $\times 10^{-89}$ (cm^{-12})	$Nr_{jk}^{-12}[3\cos^2\gamma-1]^4$ $\times 10^{-89}$ (cm^{-12})
4.2112	0	2	.3586	1.4344	.6429	10.2864
6.6585	18.44	8	.0918	.2653	.0105	.0877
5.1576	35.26	8	.4250	.4252	.2258	.2260
7.8784	36.70	16	.0669	.0577	.0028	.0021
2.9778	45	8	11.474	2.8685	164.565	10.2854
5.9555	45	8	.1793	.0448	.0402	.0025
7.2940	54.74	8	.0531	.0000	.0035	.0000
7.8784	57.69	16	.0669	.0014	.0028	.0000
5.1576	65.9	16	.8500	.2123	.4516	.0282
6.6585	71.57	8	.0918	.0450	.0105	.0025
7.8784	74.5	16	.0669	.0413	.0028	.0011
2.9778	90	4	5.7370	5.7370	82.2825	82.2825
4.2112	90	4	.7172	.7172	1.2858	1.285
5.9555	90	4	.0897	.0897	.0201	.0201
6.6585	90	8	.0918	.0918	.0105	.0105

Lattice Sum - 2nd moment

$$\sum_k r_{jk}^{-6}[3\cos^2\gamma-1]^2 = 12.0316 \times 10^{45} \text{ (cm}^{-6}\text{)}$$

Lattice Sum - 4th moment

$$\sum_k r_{jk}^{-12}[3\cos^2\gamma-1]^4 = 104.52 \times 10^{89} \text{ cm}^{-12}$$

ions at different sites in a face-centred cubic spin lattice are tabulated. The list has been arranged in order of increasing values of θ_k, and then increasing values of r_{jk} to illustrate the point. From the table we obtain the values of the lattice sum contributions to the second and fourth moments respectively of

$$\left.\begin{aligned} \sum_k r_{jk}^{-6}(3\cos^2\theta_k - 1)^2 &= 12.0 \times 10^{45}\ \text{cm}^{-6} \\ \sum_k r_{jk}^{-12}(3\cos^2\theta_k - 1)^4 &= 104.5 \times 10^{89}\ \text{cm}^{-12} \end{aligned}\right\} 5.10$$

5.3 Linewidths and Lineshapes.

Taking the effective spin S = 5/2 and g = 2.0033 (66) we now use the expression at 5.9 and the results of the summations of the previous section to obtain second and fourth moments of

$$\left.\begin{aligned} \langle \Delta\nu^2 \rangle &= 2.1525\ f \times 10^{20} \quad (\text{Hz})^2 \\ \langle \Delta\nu^4 \rangle &= 0.3345\ f \times 10^{40} \quad (\text{Hz})^2 \end{aligned}\right\} 5.11$$

The ratio of these moments gives information regarding the lineshape. Al'tshuler and Kosyrev (63) give

$$\frac{\langle \Delta\nu^4 \rangle^{1/4}}{\langle \Delta\nu^2 \rangle^{1/2}} \gg 1$$

for a Lorentzian line. From 5.11 we get

$$\frac{\langle \Delta\nu^4 \rangle^{1/4}}{\langle \Delta\nu^2 \rangle^{1/2}} = \frac{0.518}{\sqrt[4]{f}} \qquad 5.12$$

To obtain a value for the theoretical linewidth we asume the line to be truncated at $\nu_0 = \pm\alpha$, where ν_0 is the centre frequency; then

if the half-width at half-height is $\Delta H_{1/2}/2$ we may use the relations (57)

$$\langle \Delta \nu^2 \rangle = \frac{\Delta H_{1/2}\,\alpha}{\pi} \quad \text{and} \quad \langle \nu^4 \rangle = \frac{\Delta H_{1/2}\,\alpha^3}{3\pi} \qquad 5.13$$

to obtain

$$\left[\frac{\Delta H_{1/2}}{2}\right]^2 = \frac{\langle \Delta \nu^2 \rangle^3}{\langle \Delta \nu^4 \rangle} \frac{\pi^2}{12} (\text{Hz})^2$$

For a Lorentzian shape (63)

$$\Delta H_{rms} = \frac{\Delta H_{1/2}}{\sqrt{3}}$$

so we have

$$\Delta H_{rms} = \sqrt{\frac{\langle \Delta \nu^2 \rangle}{\langle \Delta \nu^4 \rangle}} \cdot \frac{\pi}{3} \cdot \frac{\partial H}{\partial \nu} \quad g\,\text{auss} \qquad 5.14$$

where $\partial H/\partial \nu$ is obtained from the experimental isofrequency plot. Substitution then gives us the result for Fe^{3+} ions in the MgO lattice

$$\Delta H_{rms} = 20.39\ f \qquad \text{kilogauss} \qquad 5.15$$

which is the result used in Chapter 6 to calculate theoretical linewidths of the EPR spectra. The calculated values are listed in that section, alongside the experimental values.

CHAPTER 6

EPR : Experimental Results

For the initial characterisation of the impurity states and distributions spectra were obtained from samples of various nominal impurity concentrations, both before and after solution treatment and at various temperatures from 4 K to 300 K. Dual cavity spectra were used to determine the number of isolated Fe^{3+} ions whilst single cavity spectra gave information regarding the behaviour of the cubic site Fe^{3+} Zeeman energy levels as a function of applied field direction, and the widths of the spectral lines as a function of applied field direction and of impurity concentration.

6.1 Experimental Results.

All samples when received showed mainly the well known Fe^{3+} cubic site spectrum. The nominally pure (i.e. 4N) samples showed in addition a strong line at g = 1.980 which was taken to be Cr^{3+}, also in cubic sites. Examples of typical spectra are given in Figures 6.1 and 6.2, 6.1 being taken from a sample with a nominal iron concentration of 310 ppm by weight, and 6.2 (a) and (b) showing spectra from 4N samples, before and after solution treatment respectively.

The Fe^{3+} $+1/2 \rightarrow -1/2$ transition was found to be almost isotropic, whilst the fine structure lines were highly anisotropic, in agreement with previously published data (16). Following solution treatment the $+1/2 \longrightarrow -1/2$ transitions were always considerably

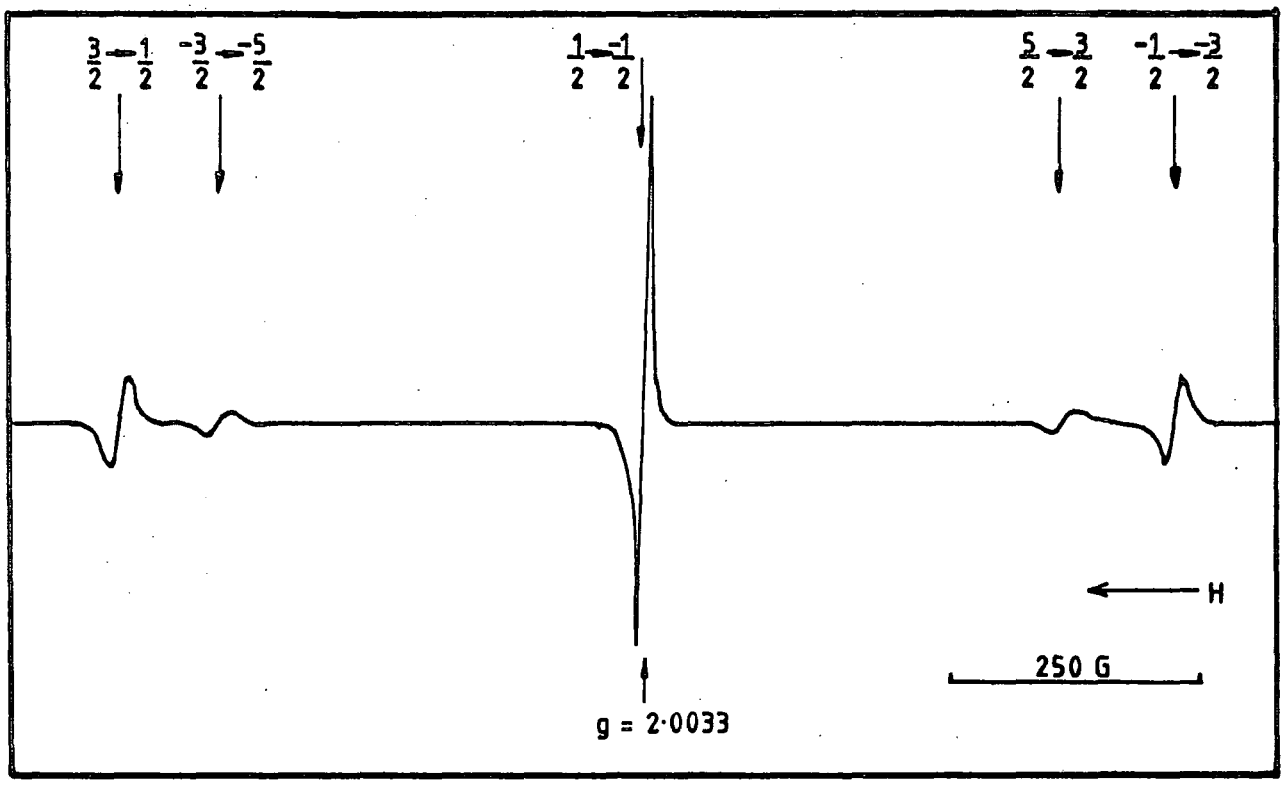

Figure 6.1 Spectrum of Fe^{3+} in cubic sites: 9.2GHz, H//K100>, 310 ppm Fe

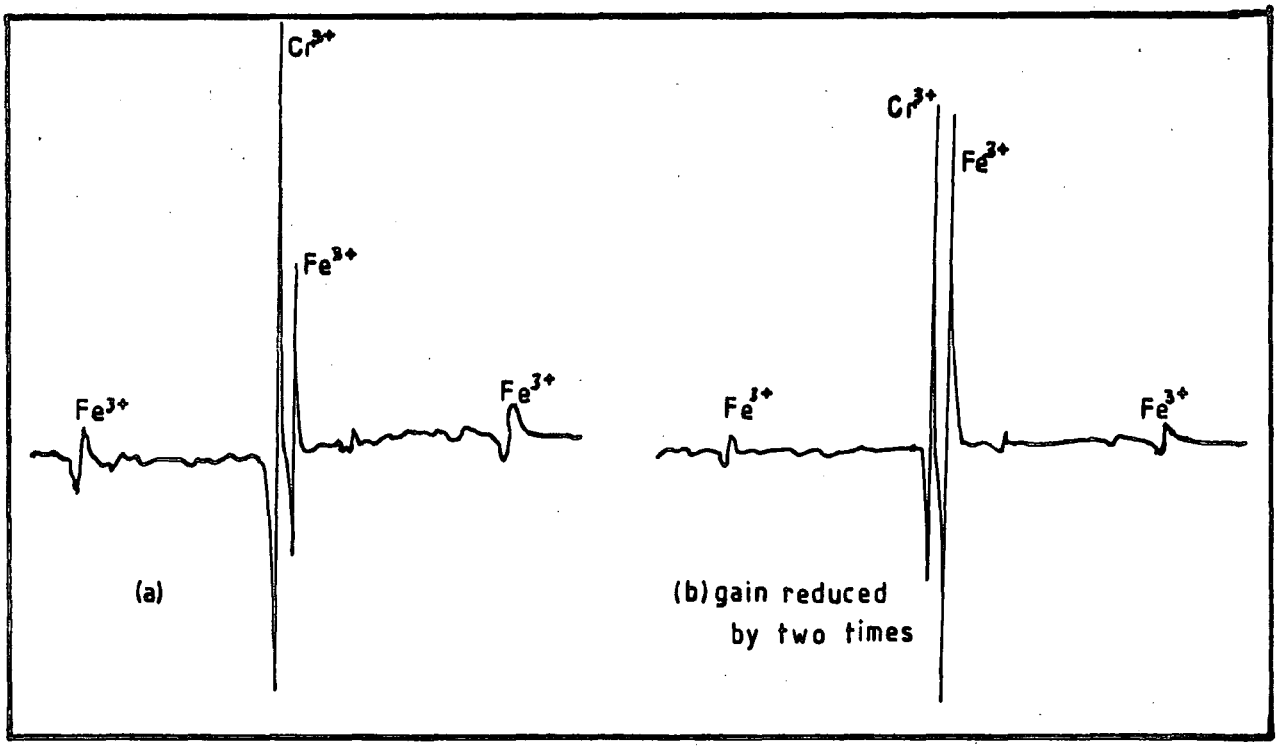

Figure 6.2 Spectra from 4N sample: (a) before, (b) after, solution treatment

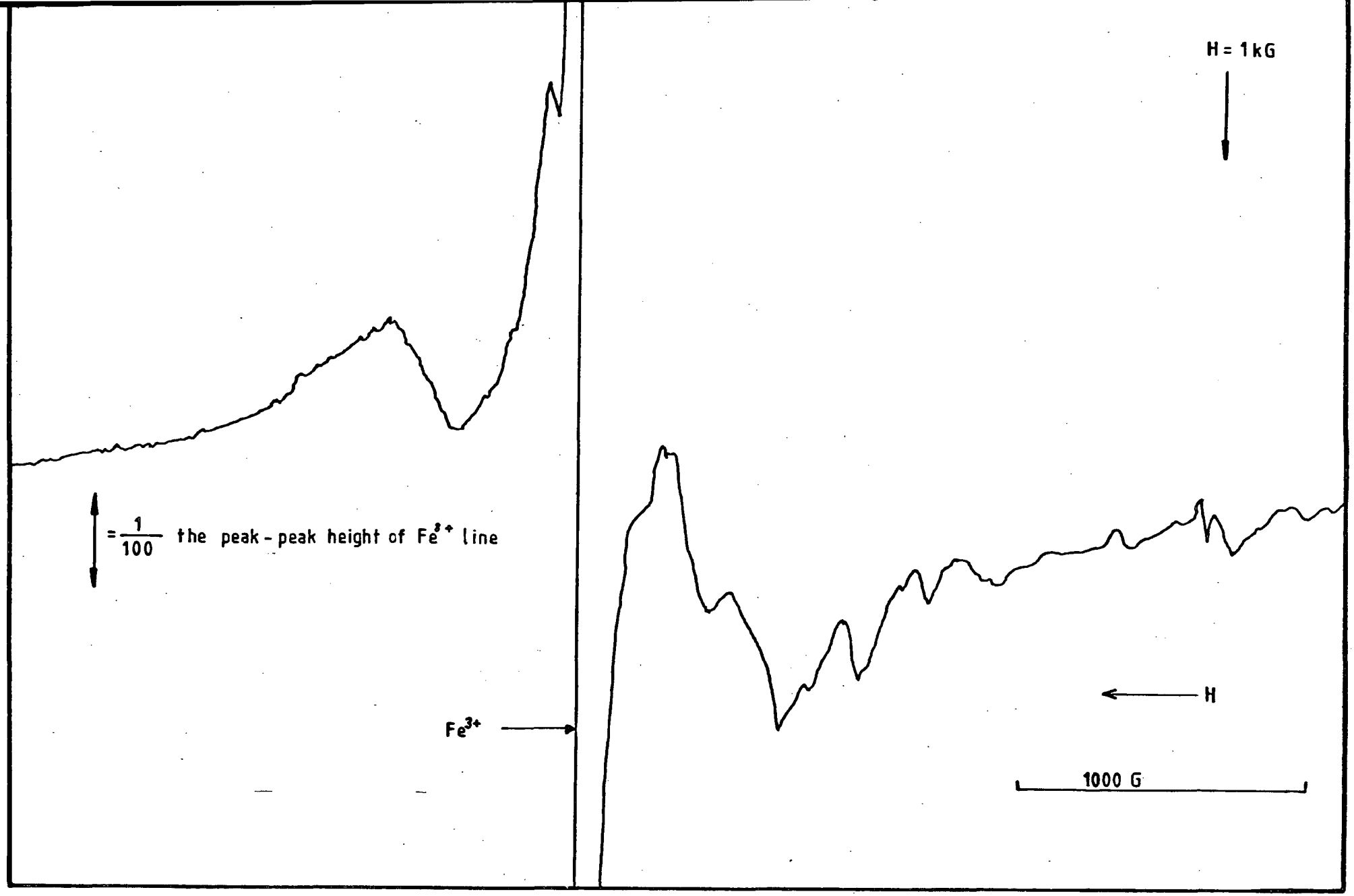

Figure 6.3 Spectrum from 4300 ppm sample, E1; 4.2 K; H //⟨100⟩; 9.111 GHz ; after solution treatment

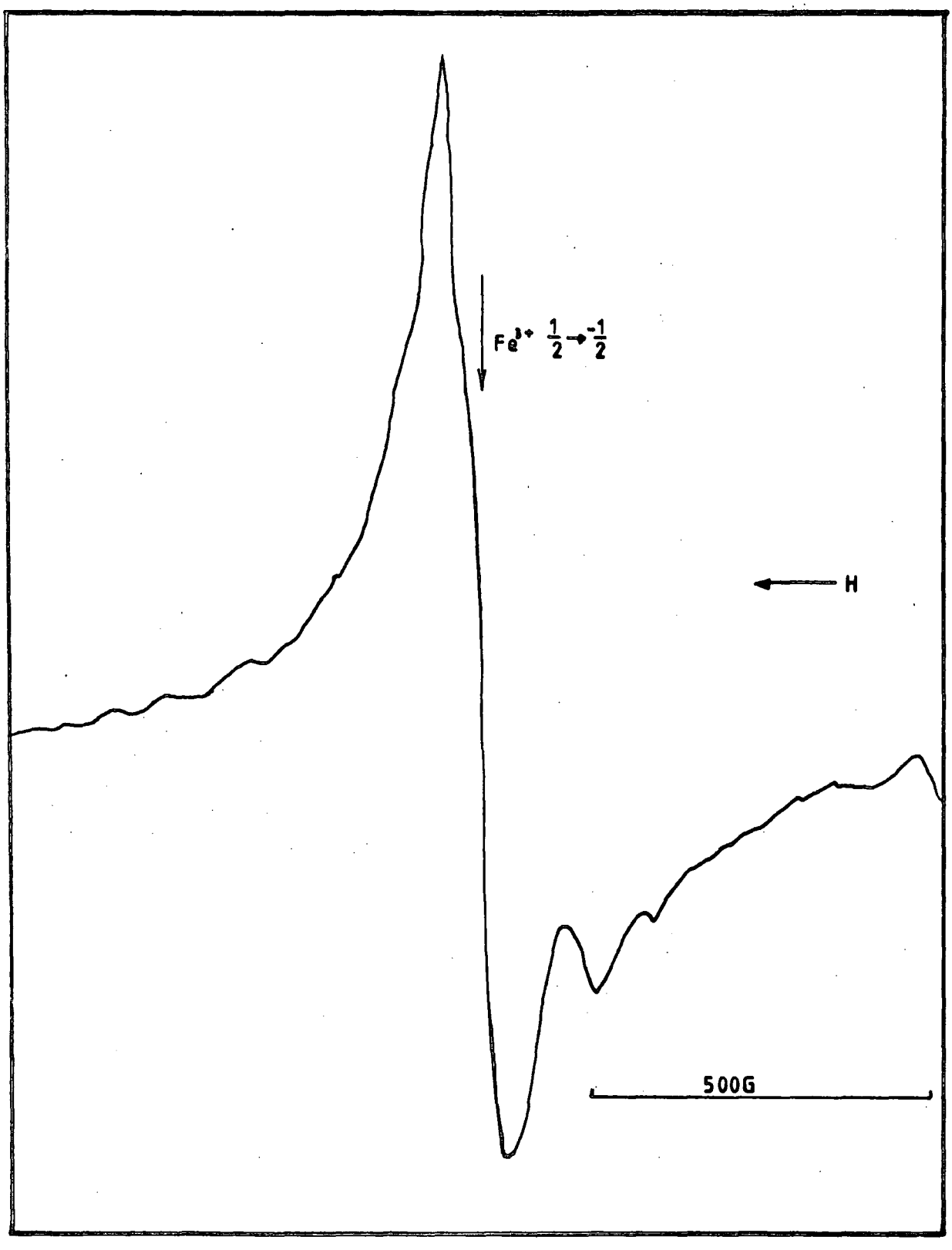

Figure 6.4 Spectrum from E1 ; 4.2 K ; H at 35° to ⟨100⟩, in (010) plane; 9.111GHz

enhanced, but it was noted in addition that

i) the amplitude of these transitions increased considerably compared with the amplitude of the Cr^{3+} transition, in those cases where the latter could be observed;

ii) the amplitude of the central Fe^{3+} transition increased considerably, relative to the amplitude of the fine structure transitions;

and iii) that in two samples - E1 and F1 - which contained nominally 4300 and 8500 ppm iron by weight respectively the fine structure disappeared, although the central transition appeared to be enhanced in the usual way. At the same time features which had the appearance of a very broad, but very low amplitude line appeared. This broad line, if that is what it is, is centred about g = 2, and has a width measured from peak to peak of the derivative, of 1.3 kilogauss.

At liquid Helium temperatures and very high gains the low field section of this 'line' showed several features, which were identical in both samples. These features are illustrated in Figure 6.3, which shows a spectrum recorded at 4.2 K. Upon rotation of the crystal with respect to applied field, this 'line' narrows considerably, being at its narrowest when the field lies in a direction of about 35^{o} with respect to the [100] axis. Figure 6.4 illustrates this effect, and also shows that this narrowing is accompanied by a great increase in intensity, the peak to peak amplitude for this orientation rivalling that of the Fe^{3+} central

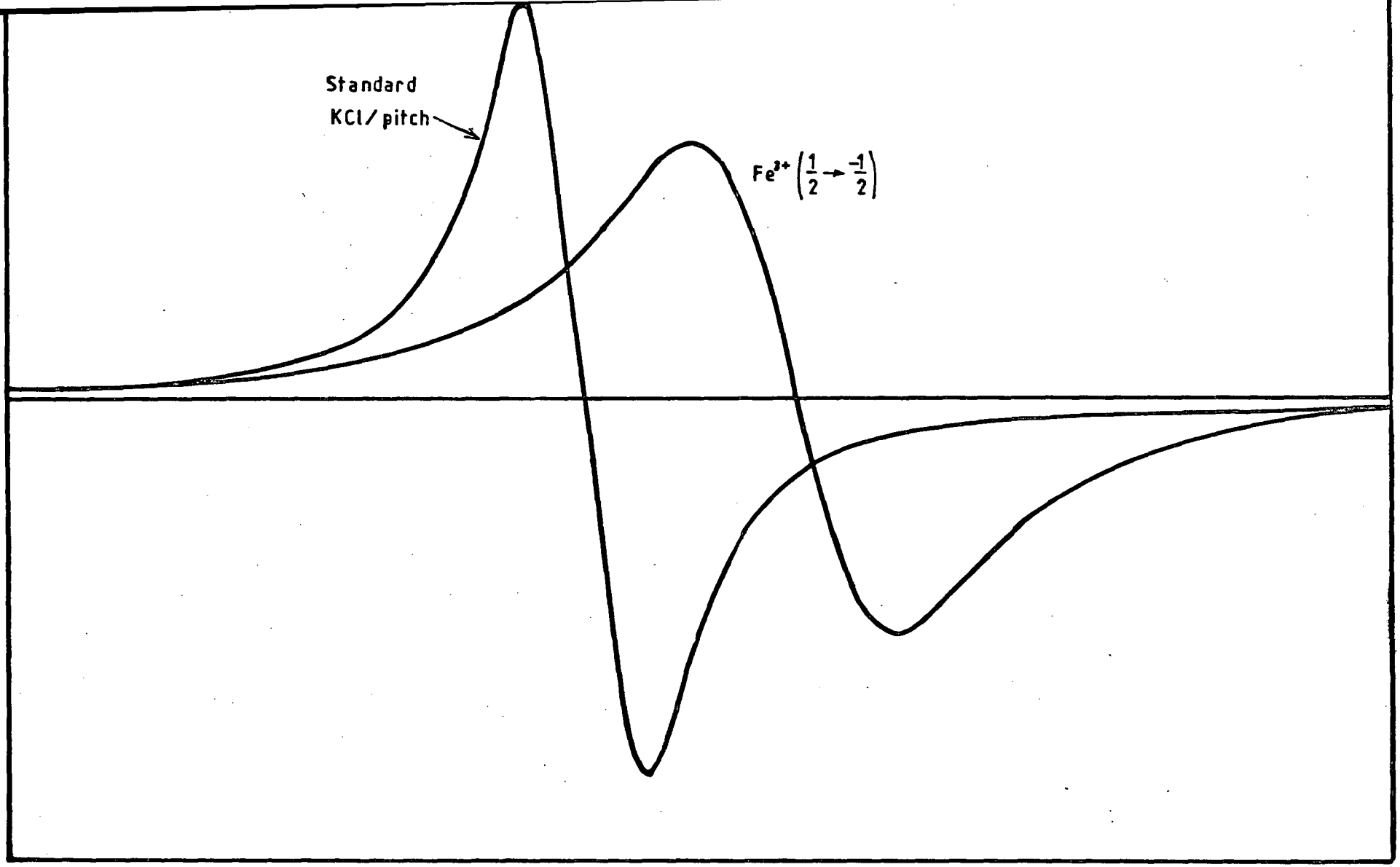

Figure 6.5 Dual cavity spectra : pens are offset along field axis

transition, which it overlies.

Many of the samples showed a group of two or three additional weak lines at a field of about 1.0 kilogauss. As the proton magnetometer could not be induced to work at frequencies low enough to allow precise determinations of g-values for these lines an estimate was made by comparison with the Fe^{3+} cubic site spectrum. This comparison gave $g \approx 6$, and it is therefore assumed that these lines are due to Fe^{3+} ions in sites of lower symmetry (18,67). The amplitudes of these lines also increased with solution treatment, but even then was very small indeed when compared with that of the cubic site spectrum.

After solution treatment there was no sign of any iron in the Fe^{2+} or Fe^{1+} states. Whilst Fe^{1+} was not expected, Fe^{2+} was, and consequently the appropriate regions of the spectrum were swept at 4 K, very slowly, and at high gain - to no avail.

Figure 6.5 shows an example of the output from the dual-channel system used to count spins. The technique employed was to record two such spectra, the samples being switched between channels for the second recording, resulting in a total of four curves. The curves were integrated numerically, and the absorption curves obtained were then integrated using Simpson's Rule to give the area under each. The reason for switching channels is that one can then ignore the different sensitivities of the two channels, and obtain the spin count directly by means of the expression (derived in ref.68)

$$N_g = N_c \left[\frac{A_{g1}}{G_{g1}} \cdot \frac{A_{g2}}{G_{g2}} \cdot \frac{G_{c1}}{A_{c1}} \cdot \frac{G_{c2}}{A_{c2}} \right]^{1/2} \qquad 6.1$$

Here subscripts B and C refer to 'unknown' and 'standard' respectively; subscripts 1 and 2 refer to channels 1 and 2; N is the number of spins per unit volume, A the area under the curve, and G the amplifier/recorder gain. The measured numbers of spins are given in Table 6.1 along with the deduced weight fraction and the manufacturers nominal concentration of iron in the samples.

Linewidths were determined for the $+1/2 \rightarrow -1/2$ transitions with the static field directed along the $\langle 100 \rangle$ axes, the width (ΔH_{ms}) being measured as the peak-to-peak separation of the derivative curves. Values of linewidths, which agree well with published values (16), are given in Table 6.2 for samples before and after solution treatment. In some cases the crystal was rotated so that the variation of linewidth with direction of applied field could be determined. A typical plot showing the measured variation of width with orientation is shown in Figure 6.6.

6.2 Spin Counts and Impurity Concentrations

The dopant concentrations obtained from the spin count data and listed in Table 6.1 are astonishing. It can be seen that in every case the measured quantities of Fe^{3+} isolated ions on cubic sites comprise only a fraction, and in most cases a very small fraction, of the total iron content of the samples. These quantities suggest no simple relationship exists between the total quantity of iron in the samples and the quantity which occupies the cubic sites in the Fe^{3+} state. Whilst solution treatment does increase the intensity of the cubic site spectrum, even after this treatment only the very lightly doped samples show a spectrum which represents a reasonable amount of the total iron content.

TABLE 6.1 : Iron concentrations calculated from spin-count data.

Sample	Nominal Concentration (ppm wt.)	As received		Solution Treated	
		Spin Density (mm^{-3})	ppm wt.	Spin Density (mm^{-3})	ppm wt.
A1	4N	0.79×10^{15}	20	4.26×10^{15}	110
C1	310	2.31×10^{15}	60	8.36×10^{15}	216
D1	2,300	2.40×10^{15}	62	18.20×10^{15}	471
E1	4,300	1.70×10^{15}	44	15.60×10^{15}	404
F1	8,500	1.07×10^{15}	28	14.70×10^{15}	380
G1	11,900	1.21×10^{15}	31	19.20×10^{15}	497
H1	12,900	0.79×10^{15}	20	12.40×10^{15}	321

TABLE 6.2 : Measured linewidths for the Fe^{3+} $\frac{1}{2} \leftrightarrow -\frac{1}{2}$ transition ; H // <100> ; 9.2 GHz ; 293 K

Sample	Nominal Concentration (ppm wt.)	Linewidth ΔH_{ms} (Gauss)	
		As received	Solution treated
A1	4N	4.9	5.8
C1	310	5.4	6.4
D1	2,300	5.0	8.6
E1	4,300	5.3	10.3
F1	8,500	6.9	11.6
G1	11,900	6.3	9.8
H1	12,900	5.7	11.1

Even were all the iron in isolated cubic sites as Fe^{3+} ions we would not expect to account for all of it in the spin count figure since this was derived from the $+1/2 \rightarrow -1/2$ transition, and there is insufficient data on the relationship between the intensity of this line and the fine structure lines to allow extrapolation. Nevertheless, the fine structure lines were always of relatively very low intensity, or non existent, and it was felt justifiable therefore to ignore them when converting from spin counts to cation site fraction or ppm weight.

Since all the spin counts were made using the one standard - the Varian 'pitch on KCl' standard - one might suspect that the low spin counts may have been due to some experimental error. However an error with an effect which depends upon the concentration of iron in the magnesium oxide in a highly non-linear manner would need to be postulated, and one does not readily spring to mind. The particular standard used was recently compared, by Hodgkiss (69), with a variety of copper sulphate single crystals and with DPPH, and found to produce consistent results in each case. In addition, we have found that repeated measurements on the same iron doped magnesia samples leads to reproducibilty in spin count of within ten per cent. Finally, we have checked the spin counts of samples C1 and E1 by comparing them directly with each other using the dual cavity method. The ratio of their spin counts measured in this way agrees to within six per cent with that obtained by comparing each independently with the standard sample.

It would seem reasonable, in the light of the evidence available, to conclude that the spin counts obtained give to within a factor of about two the total number of Fe^{3+} ions on isolated cubic

sites. The problem which immediately arises is the question as to the location and state of the rest, in many cases the major fraction, of the iron. It is assumed throughout that the figure for total iron concentration given by the manufacturer is correct. This figure is obtained by x-ray fluorescence analysis by Johnson, Matthey and Company, and is quoted to within two per cent. Yager and Kingery (70), besides others, have checked the total iron content of various Spicer magnesium oxide crystals, and have concluded that the manufacturer's figures are reasonable.

Assuming then that the figures for total iron content and for Fe^{3+} ions isolated in cubic sites are as outlined in Table 6.1, then the remainder of the iron must be either

i) in some other spectroscopic state

or ii) in some sites other than isolated cubic ones i.e. clustered in such a way that it does not contribute to the isolated ion signal.

Despite repeated careful slow scans in the appropriate regions of the spectrum it has not been possible to obtain any EPR evidence of the existence of any of the iron in the Fe^{2+} state after solution treatment. (Unfortunately the helium cryostat was not available early enough to allow a check for this ion before the solution treatment.) Even allowing for the difference in transition probabilities it is thought to be unlikely that Fe^{2+} ions were present in any quantities and undetected, at the instrument gains used in the helium runs.

There is evidence that some of the iron is present in the 3+ state in non-cubic sites. This is suggested by the lines at $g \approx 6$ apparent in many of the spectra, which are taken to be Fe^{3+} in sites of axial and orthorhombic symmetry (18,67). However the

intensity of these lines is always minute in comparison with the lines of the cubic site spectra. Consequently, one is forced to return to the possibility that either there is some flaw in the spin-counting technique; or many of the iron ions are in the Fe^{3+} state, but clustered in such a way that they do not contribute to the Fe^{3+} spectrum.

This type of behaviour has been reported previously by de Biasi (34). His data are shown plotted alongside ours on the graph in Figure 6.7. It can be seen that whilst the results of de Biasi and of the present study do not coincide they do exhibit a similar type of behaviour in terms of the trends with changing concentrations of iron. Wicks and Lewis (31) also report a measurement of the number of Fe^{3+} isolated ions in a sample of magnesium oxide, as a fraction of total iron concentration. Their data has also been plotted in Figure 6.7 and it can be seen that again there is reasonable agreement with our data.

As further evidence that clustering is important one may point to the fact that the solution treatment increases the intensity of the spectrum. It has been pointed out earlier (Chapter 2) that heating the samples above about 650°C and then quenching them should result in a decrease in the quantity of iron in the Fe^{3+} state, which would in turn result in a decrease in the intensity of the spectrum. Presumably any decrease in the fraction of iron in this state which may take place is offset in our case by the dissolution of clusters at elevated temperatures, leading to the observed increase in the intensity of the isolated ion Fe^{3+} spectrum.

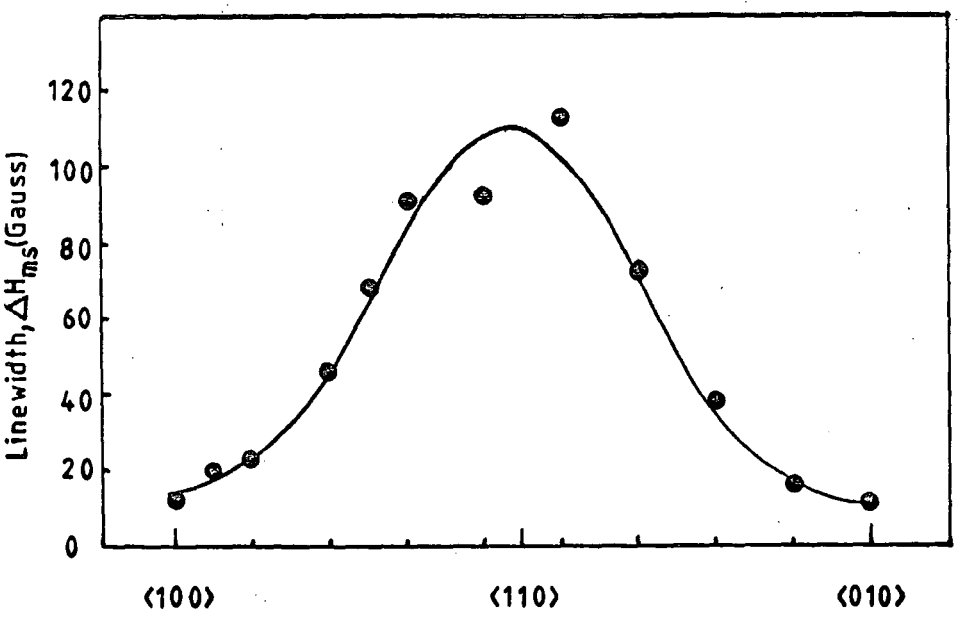

Figure 6.6 Variation of linewidth with orientation
293K : 8500ppm iron : H in {100}

Figure 6.7 Comparison of measure quantity of Fe^{3+} in cubic sites with total iron content(manufacturer's value)

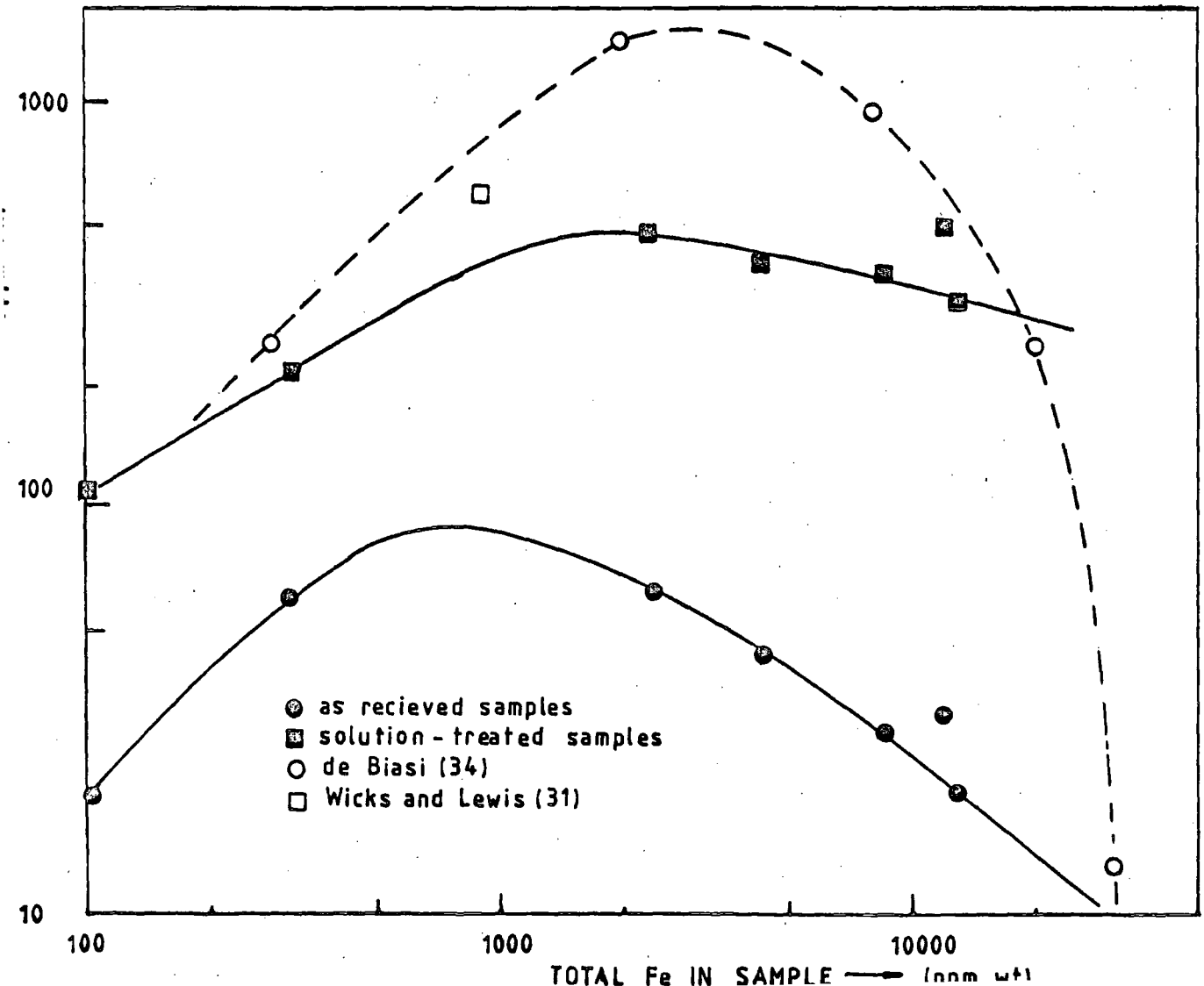

6.3 Measured Linewidths and Impurity Concentrations

It has been shown in Chapters 4 and 5 that if the iron ions are isolated, that is are separated sufficiently from other iron ions and from charge compensating vacancies that the symmetry of their spectra is essentially cubic, then the EPR spectral lines will be Lorentzian in shape. The derivative peak-to-peak linewidth ΔH_{ms} will vary linearly with concentration of iron, and will be given by

$$\Delta H_{ms} = 20.39\ f \qquad \text{kilogauss} \qquad (6.2)$$

where f is the cation site fraction. This relationship between the linewidth and the concentration of impurity can be used to give a check upon the surprisingly low values of spin counts dealt with in the previous section.

If the small measured impurity contents discussed in that section are a result of a faulty standard sample, or a fault in the experimental technique which has introduced a systematic error of some sort, then it could be possible that the integrated intensity of the line would be falsely reduced, leading to inexplicably low values for the spin counts. However, were this the case, although the amplitude of the spectral line would be reduced the lineshape and the linewidth, which are depedent upon such factors as the nature of the impurities and the interactions between them, would remain unchanged.

Measured values of the linewidths when the static field is applied along a $\langle 100 \rangle$ axis are listed in Table 6.2. In Figures 6.8 and 6.9 they are compared graphically with theoretical values

Figure 6.8 Variation of measured and calculated linewidths with iron concentration - as-recieved samples

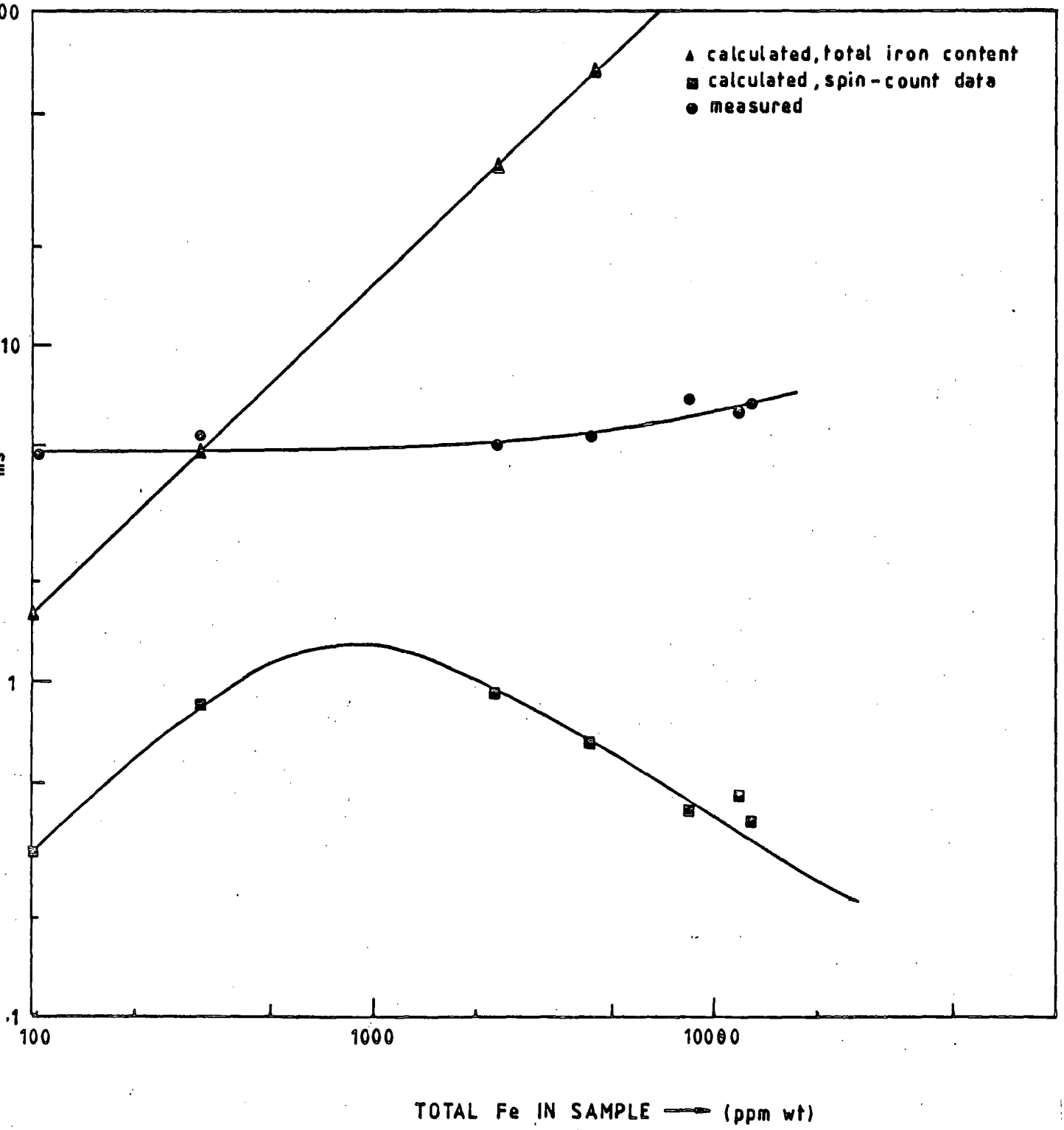

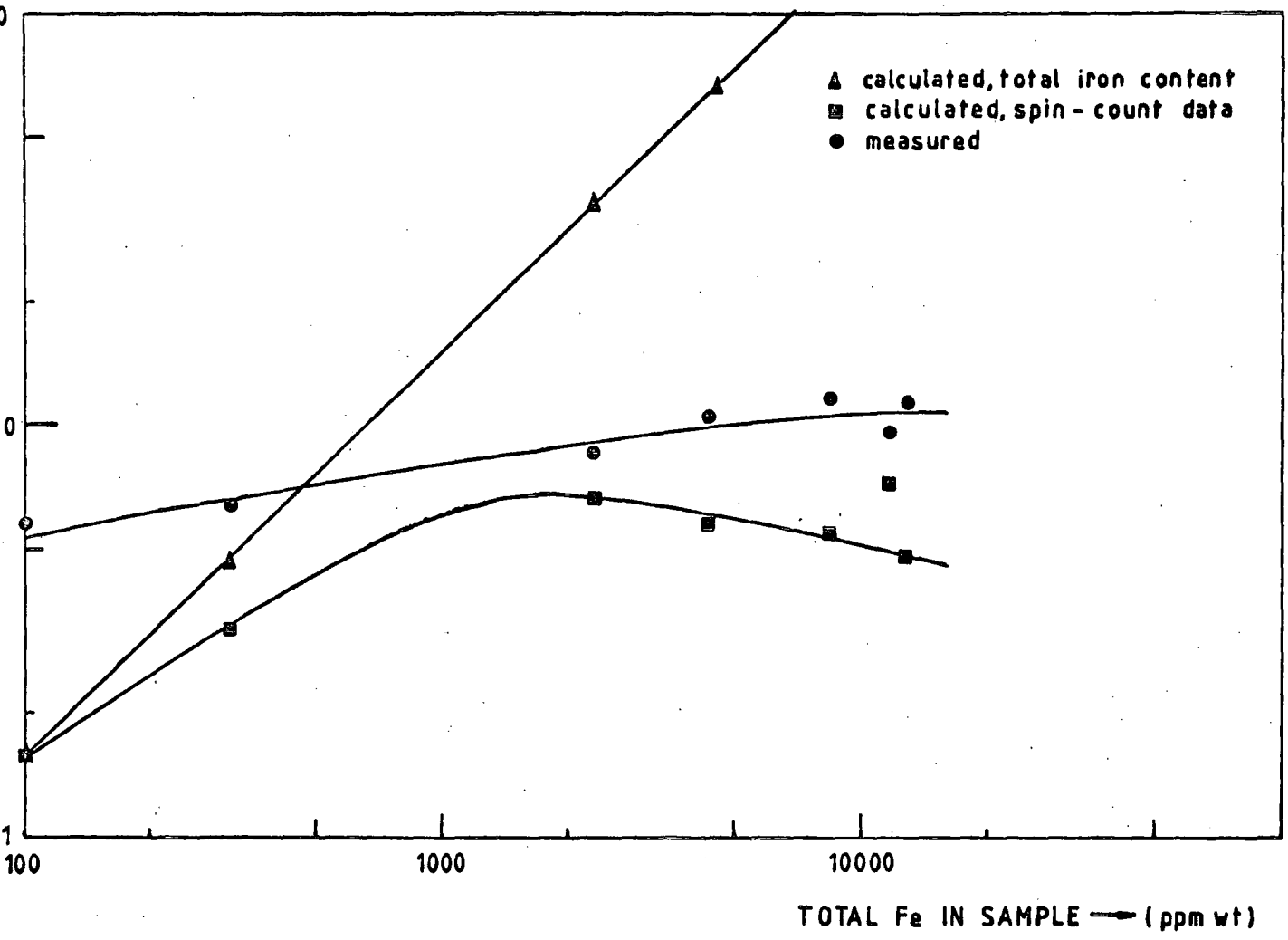

Figure 6.9 Variation of measured and calculated linewidths with iron concentration - after solution treatment

calculated both from the total iron content of the samples, according to the manufacturer's data, and from the measured quantities of Fe^{3+} isolated cubic site ions derived from the spin counts. Figure 6.8 shows the situation before solution treatment, and Figure 6.9 the situation after. In each case the linewidths calculated using the total iron content are considerably in excess of the experimental values, except in the case of the very lowest concentrations. It would be necessary, in order to correlate these calculated widths with the measured ones to invoke some sort of narrowing mechanism such as exchange or super-exchange. In Chapter 4 we have discussed this possibility and shown that it is unlikely to arise in the cases in question.

The linewidths calculated from the spin count data mirror the behaviour of the calculated concentrations, in view of the simple proportional relationship between the two. In the case of the mid-range concentrations they also provide a reasonable approximation to the measured values, bearing in mind the uncertainty in the spin count data. After solution treatment this agreement is considerably enhanced. This is to be expected since the purpose of the solution treatment is to increase the number of Fe^{3+} ions on isolated sites by dissolving clusters of iron ions.

The precise effect of a cluster on the resonance of a nearby otherwise isolated ion would presumably depend upon cluster shape, size and content as well as the separation vector between the ion and the cluster and the direction of that vector with respect to the lattice and the static field. In view of the possible number of different arangements this would be an extremely difficult, if not impossible effect to quantify, but the idea that there could be a

contribution of this type to the line width is supported by the fact that as the impurity concentration is increased the experimental line broadening becomes increasingly greater in comparison with the width calculated for dipolar broadening due to the measured iron ion concentration.

On the other hand the divergence of the measured and calculated values in the low concentration samples is thought to be only partly explained by this mechanism. That there is a contribution can be inferred from the fact that the solution treatment reduces the discrepancy between the measured and calculated values. However the increase in divergence as lower and lower concentrations are approached cannot be explained solely by this mechanism; as the concentration of iron decreases it becomes less and less likely that clusters will form, and also less likely that an isolated ion will find itself close enough to a cluster to be affected.

It is to be remembered though that the calculations of dipolar broadening have only taken into account the iron ions, which is a reasonable approach when there is a high concentration of iron. It has already been noted that in the lowest concentration samples considerable quantities of chromium, in the form of Cr^{3+} ions are present (Figure 6.2). Whilst the effect of the interaction between unlike ions is not so great as that between like ions (55) the effect of these other paramagnetic impurities would nevertheless be to broaden the line. It has been suggested elsewhere (36) that the concentration of impurities other than iron in relatively pure magnesium oxide appears to vary with the inverse of the iron concentration. Hence the behaviour depicted on the graphs - as the iron content reduces, leading to a narrowing of the calculated

linewidth the concentration of other impurities which may lead to line broadening increases. The nett effect is that the measured linewidth narrows with decreasing concentration, but not to the extent predicted by calculations based on the iron concentration alone.

We will draw this discussion of the EPR linewidths to a close by summarising as follows :-

i) There is reasonable agreement between the measured linewidths and those calculated by the Kittel and Abrahams dipolar broadening model, if the concentrations measured by the spin counting technique, rather than the total iron concentrations, are used.

ii) The discrepancies between the measured and calculated values are thought to be explainable in terms of the interactions between the isolated ions and clusters of iron ions; and in the case of the low concentrations there is of course an additional contribution from the other paramagnetic species such as chromium.

iii) In the light of this agreement it would seem reasonable to conclude that the linewidth measurements offer strong support to the surprising result of the spin count measurements discussed in Section 6.2 - that even after solution treatment and quenching much of the iron impurity in magnesium oxide remains in a clustered state, rather than in the form of a solid solution.

6.4 The Fine Structure Lines

The relative weakness of the fine structure lines, in comparison with the central transitions, is not unusual in the sense

that all workers who have referrred to the relative intensities have reported the same finding. Low (11) suggested that this effect could be partly due to disorder in the crystals, as would arise from randomly distributed vacancies or excess oxygen ions. The number of vacancies in the doped crystals will be effectively dictated by the number of Fe^{3+} ions requiring charge compensating magnesium vacancies; and magnesium vacancies imply in effect excess oxygen ions. Either or both of these mechanisms are possible contributory factors since we have always found that the relatively most intense fine structure is associated with the lower concentrations of iron, which have the fewest charge compensating vacancies.

However the fraction of iron in the Fe^{3+} state is expected to vary with iron concentration, heat treatment and oxygen partial pressure, as discussed in Chapter 2. It was shown there that for any concentration of iron the fraction in the Fe^{3+} state decreases with increasing temperature, above about $650^{o}C$. This effect may be reduced, but not negated, by carrying out the heat treatment in oxygen at atmospheric pressure rather than in air. We would therefore expect that the solution treatment would have the effect of decreasing the number of charge-compensating vacancies, consequently reducing the discrepancy between the predicted and measured transition intensity ratios. In fact we observe just the opposite effect.

The broad 'ferrimagnetic' line which appears in the spectra of samples E1 and F1 after solution treatment is similar to that reported by Weeks et al (19) as occurring in the spectra of some of their higher impurity concentration samples after heat treatment. In our case though the appearance of this line has been accompanied by the disappearance of the fine structure lines, whereas in the cases

reported by Weeks et al it was not. It may be that the two events are unrelated: if that is so it is odd that in both the samples where we have found this odd feature, and only in those samples, the fine structure lines have disappeared.

It is clearly difficult to draw any useful conclusions regarding the interpretation of the behaviour of the fine structure lines at this stage. It would seem though that since their very existence is owed to the effects of the surrounding crystal field that a closer study of their behaviour could yield much useful information regarding the crystal field as well as the behaviour of the iron ions.

6.5 EPR Results : Conclusions.

Both the spin count and the linewidth data suggest that, contrary to expectation, very little of the iron impurity in the magnesium oxide samples studied was in isolated cubic sites as Fe^{3+} ions; and that even after solution treatment in all but the most lightly doped samples the bulk of the iron was probably clustered in such a way that it did not contribute to the cubic site spectrum. These clusters may contribute to the observed line broadening, although it has been shown that much of this broadening can be explained as a consequence of dipolar interactions between iron ions and betwen iron and other paramagnetic ions.

The number of Fe^{3+} ions in cubic sites is increased on solution treatment, despite the fact that the total Fe^{3+} content of the samples is expected to decrease with this treatment. It is thought that the observed increase is further evidence for the existence of clusters, which start to dissolve with the appropriate

heat treatment. However the simultaneous observed decrease in the relative intensities of the fine structure lines is not understood, although it may be related to the appearance of a broad 'ferrimagnetic' type of line seen in some samples.

CHAPTER 7

The Effects of Aging, I : Magnetic Resonance.

When magnesium oxide containing iron impurities is aged at temperatures around 700°C there is little change in the spectral state of the iron ions (see Chapter 2); there is however a dramatic change in the magnetic resonance spectrum. The isolated ion spectrum of the Fe^{3+} ions is replaced by a massive line (or lines) of much greater intensity than would be achieved even if all the iron ions in the sample were to become isolated Fe^{3+} ions. These new lines are attributed to precipitates of magnesium ferrite, which form in the shape of octahedra, in register with the MgO lattice, and give rise to ferrimagnetic resonance.

Samples with concentrations from 100 - 12900 ppm iron were aged in oxygen as part of this study at temperatures in the range 600 - 800°C, for various aging times. In particular the effects of aging at 700°C and 800°C were studied by subjecting various samples to successive aging treatments, the resonance spectrum being obtained between each treatment. For some of the samples aged at 800°C the spectra were taken at a variety of temperatures, and analysis of these spectra gave information regarding the mean particle size, magnetisation, g-factor and stoichiometry of, and site occupation in, the spinel phase. The results of the aging experiments are presented in this chapter.

Whilst there are reports in the literature (19,31,72-76) of ferrimagnetic resonance spectra obtained from magnesioferrite precipitated in iron doped magnesia there is little information with

which to compare the spectra reported here. Although de Biasi and Devezas have derived the parameters of the precipitates such as mean volume, and magnetisation, and have reported measurements of g-value, they have not commented on linewidths or shape, or illustrated their spectra at all. Weeks, Gastineau and Sonder, on the other hand, have published two different spectra, and given rough g-values and linewidths, but have made no comment on the way in which the lines alter with aging temperature, or time.

7.1 Aging at 700°C

As might have been expected, the ease of precipitate formation turned out to vary with the iron concentration in the sample. Samples with high concentrations - 8500 ppm iron and greater - gave a very intense ferrimagnetic resonance signal after only 2 - 3 minutes at 700°C. Samples containing 310 ppm showed no precipitation for aging times up to 1 hour, whilst the 4N samples, with only a few tens of ppm iron showed no precipitation after times up to 12 hours at 700°C. Samples with 2300 ppm were interesting in that for these concentrations at this temperature the precipitation was slow enough to show some change in the resonance signal after each 5 minute aging period; whilst for the 4300 ppm samples 5 - 10 minutes were required at 700°C to produce the full ferrimagnetic signal.

An example of the spectra obtained from the 8500, 11900, and 12900 ppm samples is shown in Figure 7.1. The line is, within the limits of the measurements, isotropic, which is somewhat surprising as ferrimagnetic precipitates could be expected to show magnetocrystalline or shape anisotropy. In each of these samples the

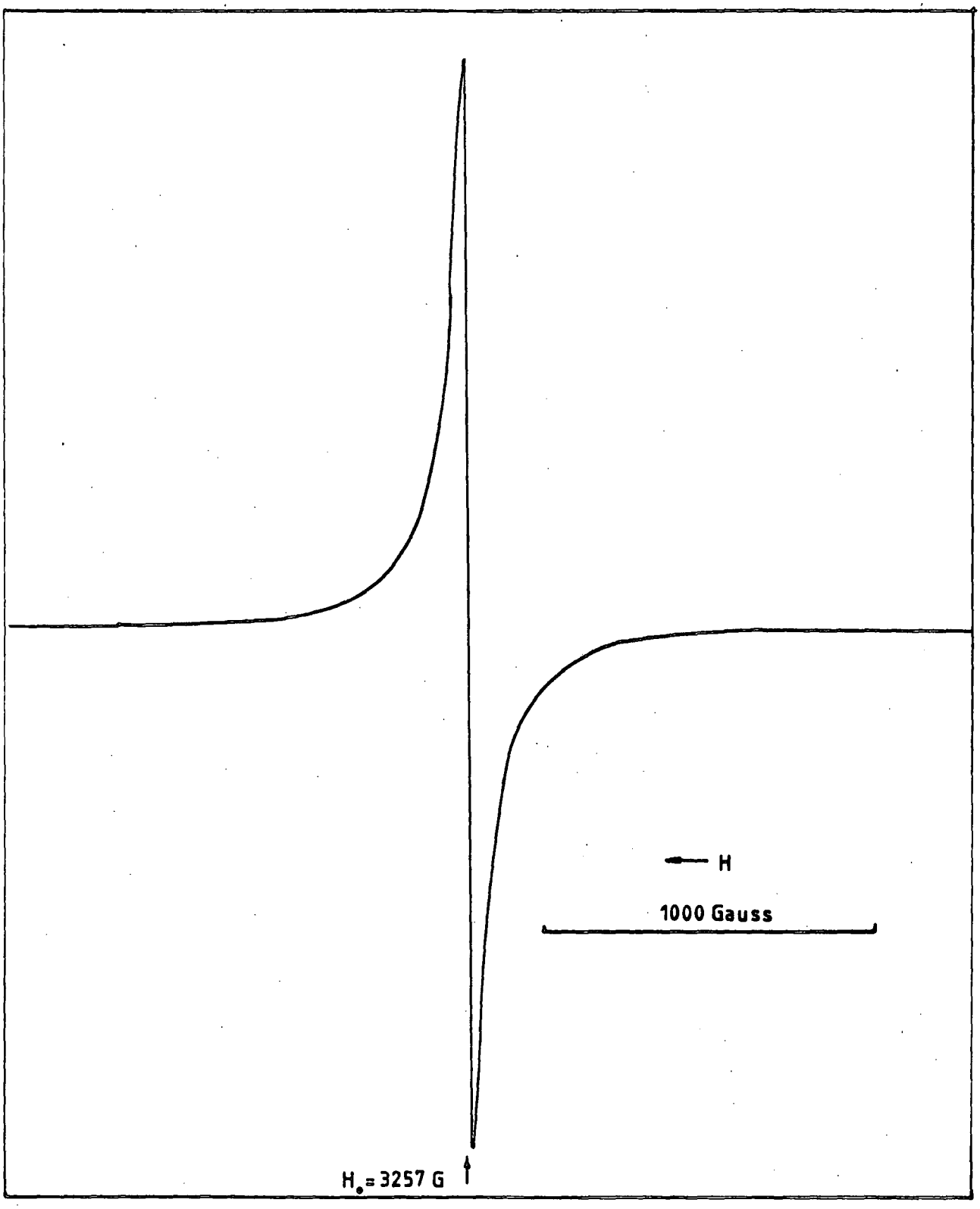

Figure 7.1 FMR Spectrum : 11900 ppm sample, after 5 min at 700° C :
9.111 GHz : H // ⟨100⟩ : 293 K

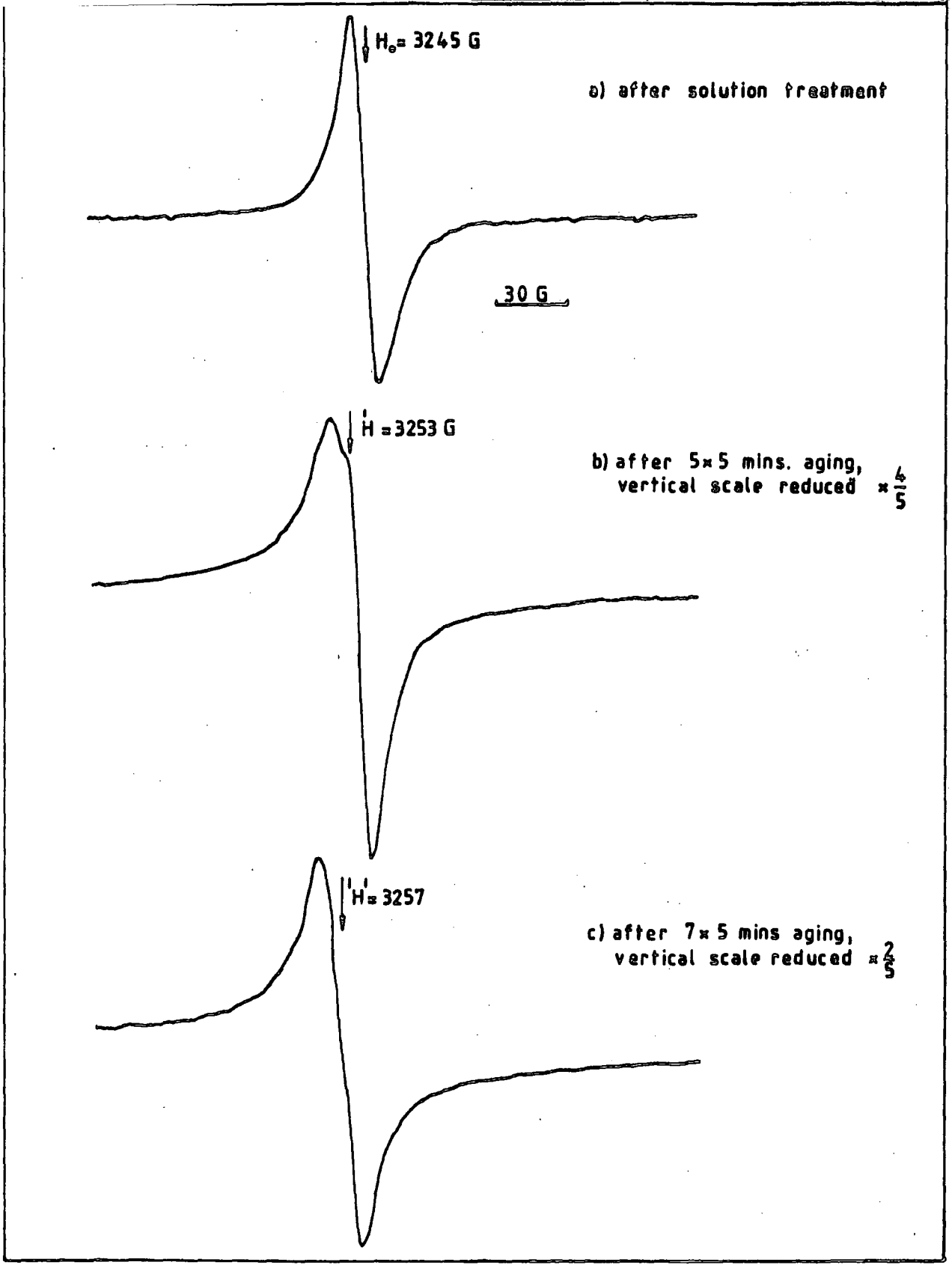

Figure 7.2 Changes in the spectrum of 2300ppm sample with aging at 700°C

All recorded at room temp.: 9.100 GHz: H//⟨100⟩:

intensity of the line increased gradually with increasing time of aging, for aging times up to one hour. We may characterise this line by an effective g-value which is given by the experimental value of 2.000 ± .003. The theoretical uncertainty is considerably greater than ±.003 but regular, repeated observations of many lines lead to the conclusion that the accuracy and precision achieved in practice are rather better than those calculated theoretically.

The linewidths of all these samples showed the same behavioural trend with aging time, decreasing from a value of approximately 30 gauss for the peak-to-peak width at the first appearance of the line to about 20 gauss after a total of one hour's heating. The scatter of results is such however that no clear empirical relationship between aging time and line width can be stated. It should be noted that although the line widths are only about half an order of magnitude greater than those found in paramagnetic resonance spectra of the isolated Fe^{3+} ions, the wings of the lines are spread considerably wider extending the base of the line over a range of many hundreds of gauss - as compared with the few tens of gauss of the paramagnetic lines. Furthermore,the width of the line decreases with increasing temperature, which confirms that this line cannot be paramagnetic in origin.

The same precipitate line was detected in the 2300 ppm sample upon aging, although it took very much longer to 'grow in'. Figures 7.2 a), b), and c) show a set of spectra taken from this sample at aging times of 0, 25, and 35 minutes respectively. These spectra are reproduced to the same scale, and show the gradual establishment - over the top of the Fe^{3+} isolated ion line - of a second line of slightly lower g-value (g = 2.000) and greater

peak-to-peak width. Evidence that this is a similar line to that found in the higher concentration samples is given by spectra such as that shown in Figure 7.3 which shows how, after 25 minutes aging the wings of the line spread, almost as far as the remainder of the fine structure lines from the isolated ion spectrum. After 35 minutes aging the fine structure had totally disappeared, and the wings of the line were spread even more widely. Unfortunately this sample broke after 40 minutes total aging, and it was not possible to pursue the growth of this particular line further. What would probably have transpired can be assessed from the behaviour of the 4300 ppm sample.

The changes in the spectrum of the 4300 ppm sample after 5 minutes aging at 700°C were the same as were achieved in the 2300 ppm sample over a period of 25 minutes: the spectrum is shown in Figure 7.4a. However a further 5 minutes treatment of the 4300 ppm sample results in the spectrum of Figure 7.4b. It may be seen that a massive line has now appeared, swamping the previous lines, although the vestiges of the isolated ion fine structure lines are still visible, implying that some Fe^{3+} ions are still in isolated sites. It is also interesting to note at this stage of the treatment the enhancement of a second, still very much weaker line, which is thought to be that due to Fe^{3+} ions associated with vacancies (70).

The spectrum of 7.4 b is repeated in Figure 7.4c at a lower gain and on this scale the features are lost and we have only a single line visible. This is the same isotropic line which appeared after only two to three minutes aging in the highly doped samples.

Considering the similarity of behaviour in all but the two samples with the lowest concentrations, the only difference between most samples being the length of time which it takes for the

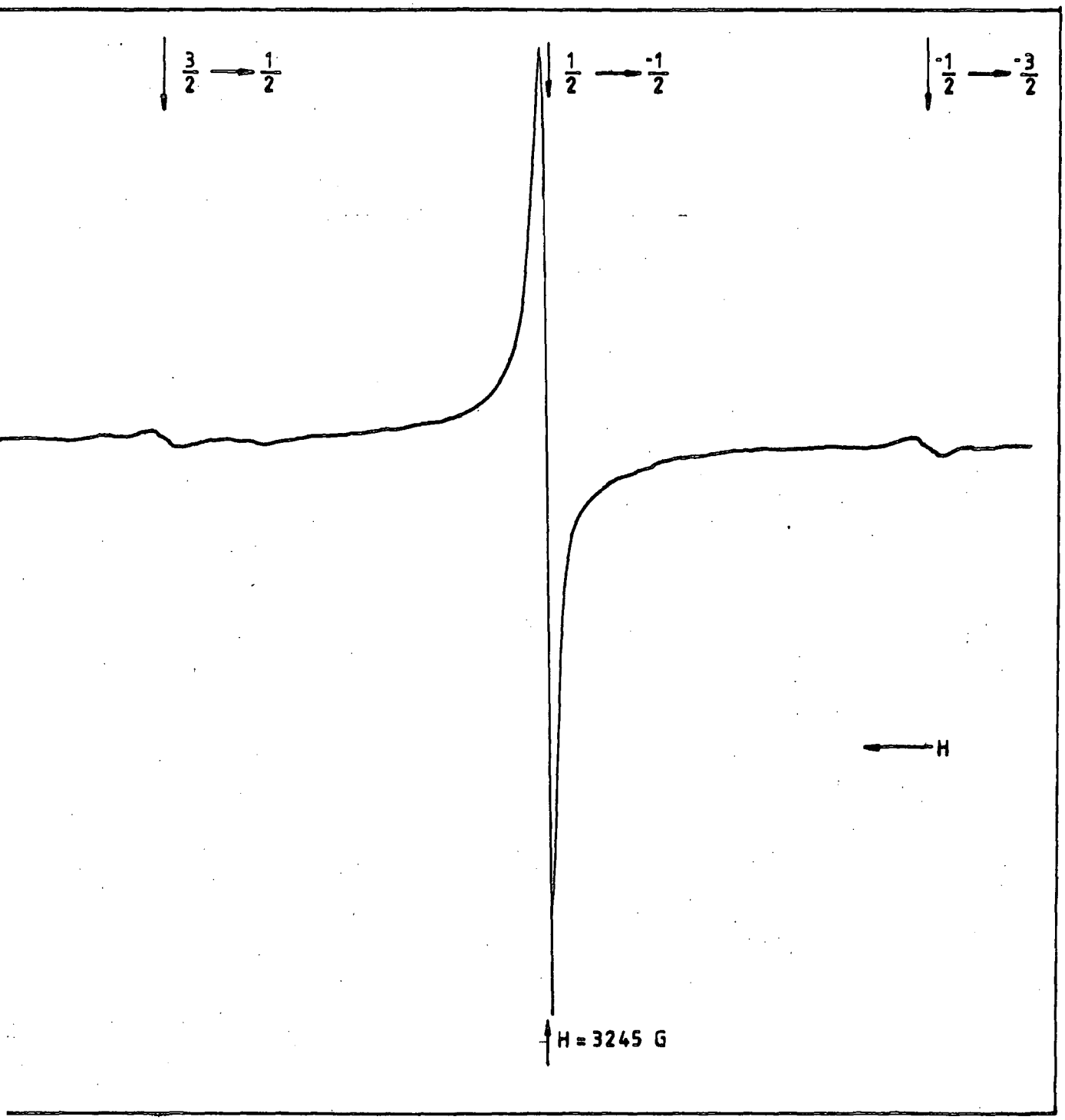

Figure 7.3 Spectrum from 2300 ppm sample, aged 5×5 mins. at 700°C.
Room temp.: 9.100 GHz : H//⟨100⟩.

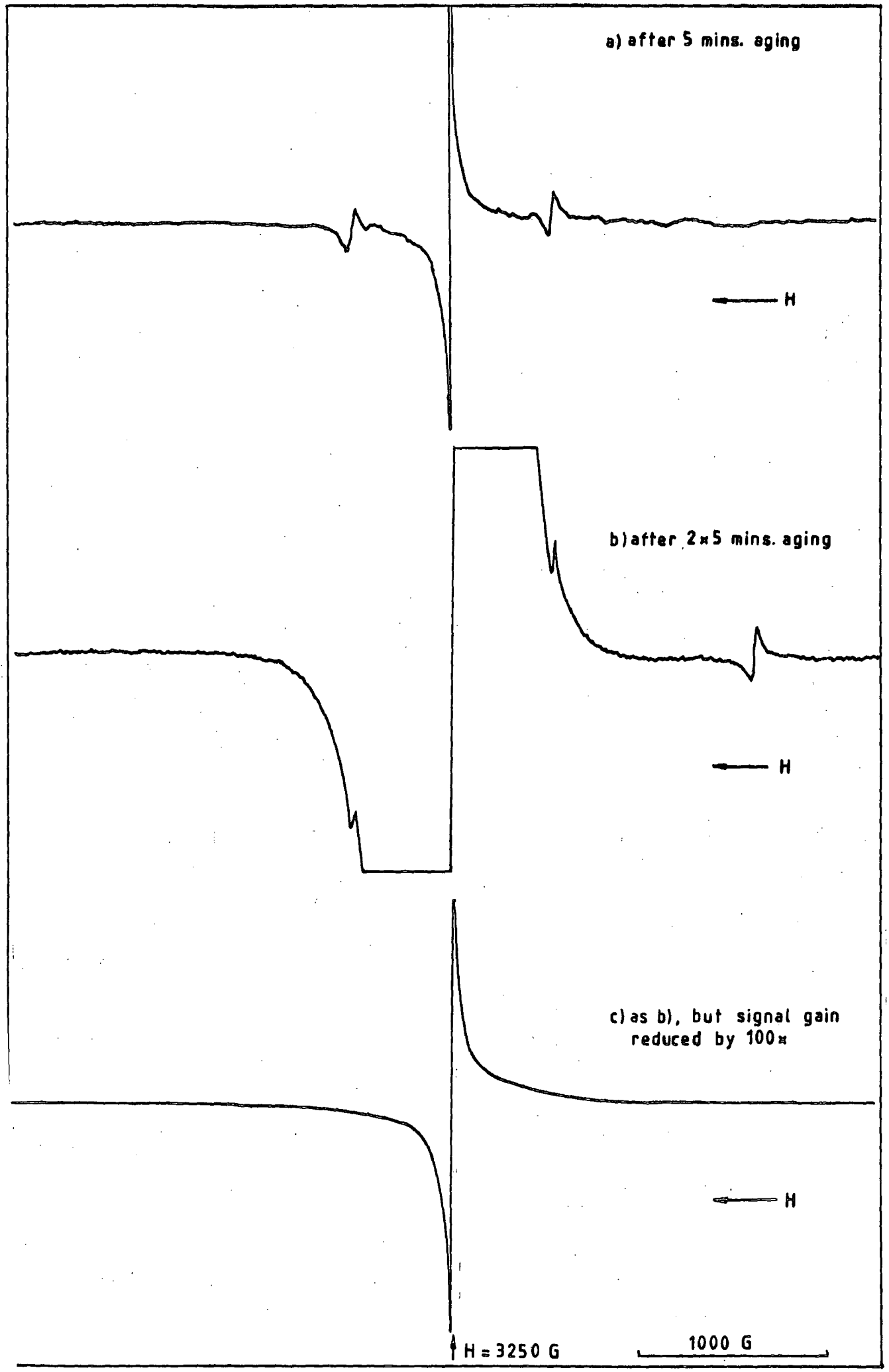

Figure 7.4 Changes in the spectrum of 4300 ppm sample with aging at 700° C (9.11 GHz:293 K: H//K100)

ferrimagnetic resonance line to appear, and since the ease with which this line may be produced clearly depends upon iron concentration, it would seem reasonable to speculate that were the aging process continued for a sufficiently long time that similar ferrimagnetic resonance would be obtained from all samples.

Aging of selected samples at 700°C for times of up to 7 hours showed that a second ferrimagnetic resonance line gradually appeared beneath the isotropic line. This second line was considerably broader, and unlike the first line, was anisotropic. Since this same broad anisotropic line could be produced much more quickly by aging at 800°C detailed investigations of the anisotropic line were carried out following aging at 800°C, and are reported in the next section.

In view of what follows in the next section it should be reiterated that the ferrimagnetic resonance line obtained initially upon aging at 700°C for times of up to one hour is isotropic, has an effective g-value of 2.000, and a peak-to-peak derivative width of 20 - 30 gauss.

7.2 Aging at 800°C

It was thought that the behaviour observed during the aging at 700°C would continue at 800°C, but at a faster rate. In other words that the EPR signal would be the same, but perhaps more intense as a consequence of more rapid precipitation. This was expected because although different FMR signals have been reported in aged iron-doped MgO the most comprehensive FMR study of the growth process - that of de Biasi and Devezas (73) - makes no mention of changes in spectra, even though the investigation covered a range of aging

temperatures from 700 - 1000°C. Consequently the programme of aging treatments selected was one which it was thought would 'overlap' with the 'top end' of the 700°C treatments, and then provide information on the behaviour as the aging was carried to much longer times. The samples were held at 800°C for consecutive periods of 0.25, 0.75, 9, and 14 hours, making a total of 24 hours treatment in all, for each sample. Once again magnetic resonance spectra were obtained from each sample between stages.

Since the spectral lines were found to be anisotropic, spectra were recorded for at least two different orientations of the samples. The results obtained from the different samples may once again be be divided into three main groups, which essentially reflect the doping levels. The 4N sample remained unaltered as far as the resonance signal was concerned, even after 24 hours at 800°C; the three highest concentration samples (8500, 11900, and 12900 ppm iron) showed similar ferrimagnetic resonance spectra; and the middle range samples showed evidence of precipitation, but not identically with that of the highly doped samples. The overall situation was considerably more complicated than that which arose from the 700°C treatment, and so the different types of behaviour are described under seperate headings.

(i) The high concentration samples - 8500, 11900, and 12900 ppm iron

The spectra from these samples after 15 minutes aging show no sign of the isolated ion spectra, but do show two very intense, overlapping lines; an example taken from the 12900 ppm sample is shown in Figure 7.5a. Because of the way in which the lines overlap it is

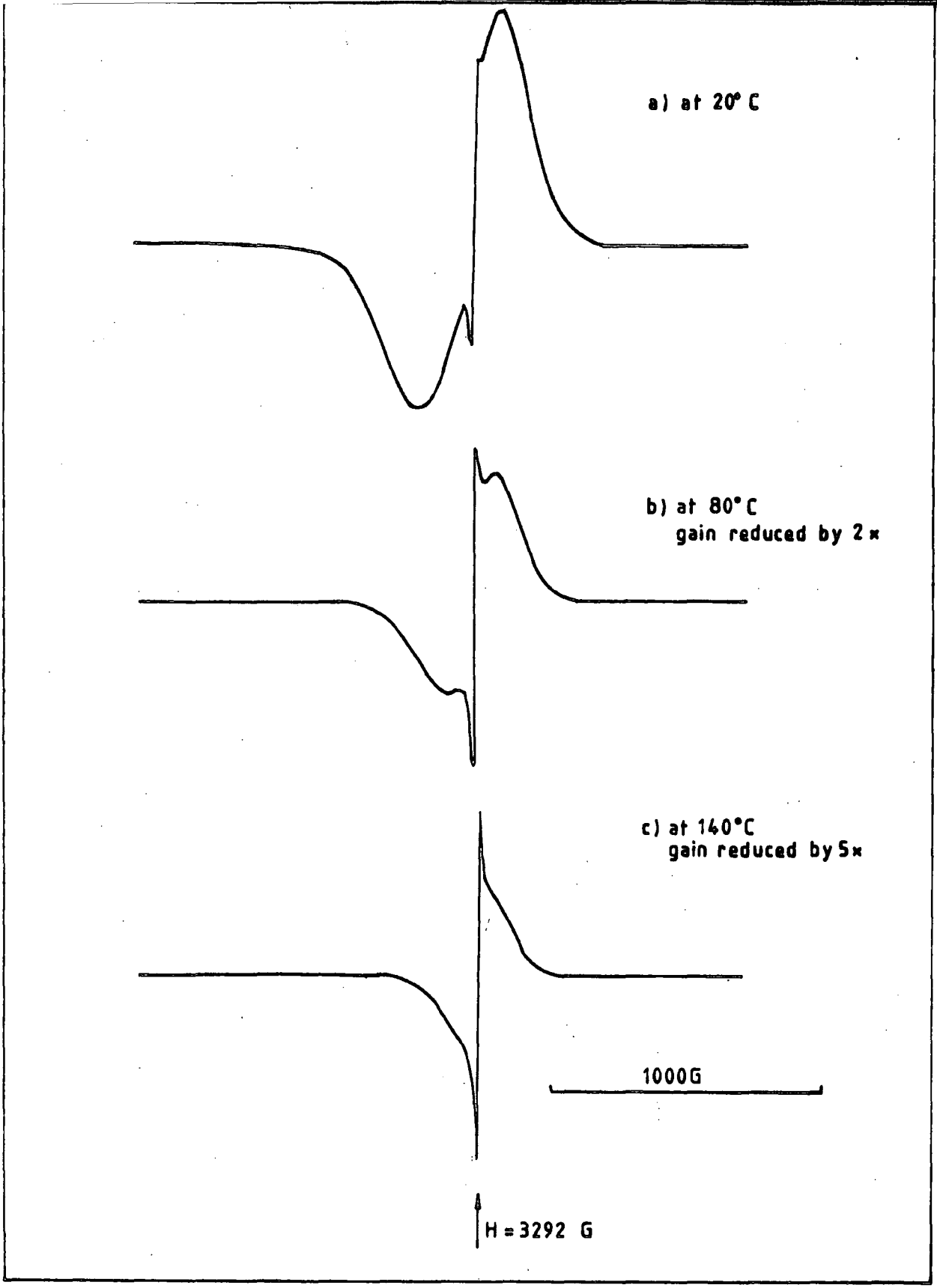

Figure 7.5 FMR Spectra from 11900ppm sample, aged 15 mins, 800°C: H// ⟨100⟩

difficult to measure the centre-field value for each line; a reasonable approximation has been obtained by taking the midpoint of the derivative peak-to-peak separations as providing this information.

The narrow line was found to have a width of a few tens of gauss, being slightly narrower when the field was applied in the ⟨100⟩ direction rather than the ⟨110⟩. The width for either orientation decreased with increasing temperature, in the case of the 12900 sample for example decreasing from 25.2 and 28.6 gauss for the ⟨100⟩ and ⟨110⟩ orientations respectively at room temperature, to 14.3 and 14.5 gauss at 140°C. This line was isotropic, to within the limits of accuracy of the measurement, having an effective g-value of g = 2.00; the uncertainty in this value being largely owed to the distortion produced by the underlying broader line. The peak-to-peak intensity was found to increase with increasing recording temperature, almost doubling, for example, when the 12900 ppm sample was heated from 80°C to 140°C. Figure 7.5a), b), and c) illustrates this change with spectra taken at temperatures of 20°C, 80°C, and 140°C respectively. The horizontal scales are the same in each case but the vertical scales have been reduced by amounts in the ratio 1 : 2 : 5.

Continued aging of the samples reduced the intensity of the narrow line - to the extent that after one hours aging it was sufficiently indistinct to prevent an estimate of the derivative peak positions. After longer aging times it appeared only as a slight distortion of the broader line, and then only at higher temperatures.

The broad line, illustrated typically in Figure7.5a, behaved differently from the narrow line in almost every respect. It was anisotropic, the anisotropy increasing with aging time, and after all

aging times being temperature dependent, varying after 24 hours aging from the order of 200 - 300 gauss at -160°C to a few gauss at 140°C. For the shortest baking times the anisotropy was found to be positive, and small; in every other case it was negative. The peak-to-peak intensity of the derivative of the line increased with aging but, unlike the narrow line the broad line decreased in intensity with recording temperature, although this is not clearly shown in Figure 7.5 where the behaviour of the narrow line disguises the behaviour of the broad line, to a certain extent.

The line width was found to be narrower in the ⟨110⟩ rather than the ⟨100⟩ orientations for all three samples at all temperatures after aging for up to an hour. After aging for ten hours the line was still narrower in the ⟨110⟩ direction when measured at room temperature, but this situation was reversed when the measurements were made at 80°C and 140°C, and was also reversed when the aging times were extended to 24 hours, for all measurement temperatures. The difference between the linewidths for the two orientations was found to be virtually constant for all three samples after 24 hours aging, being between 10 and 20 gauss over the range -160°C to 140°C. This was in marked contrast to the behaviour at short aging times, where differences in linewidths of as much as 100 gauss were obtained at room temperature, reducing with increased measurement temperature.

We return to the linewidths of these broad lines later, adding here only the comment that perhaps the most fascinating aspect of the linewidths is their repeatability from sample to sample. When lines are so wide as these it is sometimes difficult to spot the exact turning point of the derivative peak, and one may therefore expect an

uncertainty of a few gauss, which is negligible as far as lines which are of the order of a hundred or so gauss are concerned. As can be seen from the graphs presented later, when this uncertainty is allowed for the values of linewidths determined at any particular temperature for all these samples are identical, after any given aging period.

(ii) The middle range samples - 4300, 2300, and 310 ppm.

The 4300 ppm sample gives an apparently single FMR signal, after fifteen minutes aging, which is anisotropic. To within a few gauss this anisotropy does not change with aging time, up to 24 hours, but at all aging times it shows a decrease with increasing measurement temperature.

The peak-to-peak intensity of the derivative line increases with aging; and also appears to increase, at a given aging time, with measurement temperature. This increase of intensity with temperature is accompanied by an apparent narrowing of the line, although the linewidth does not change with aging time. It is always narrower in the $\langle 100 \rangle$ rather than the $\langle 110 \rangle$ orientation. It is interesting to note that as aging proceeds the symmetry of this line about its centre-field value begins to show a marked variation with orientation. This effect is illustrated in Figure 7.6 where it may be seen that when recorded in the $\langle 110 \rangle$ orientation the line is almost perfectly symmetric, whilst a definite asymmetry appears with the $\langle 100 \rangle$ orientation. The particular lines shown were obtained after aging for 24 hours, but in fact the effect is noticeable with aging times as short as one hour. The asymmetry suggests that this apparently single line perhaps comprises two lines, which overlap completely in the $\langle 110 \rangle$ orientation. If the lines exhibit slightly different degrees of

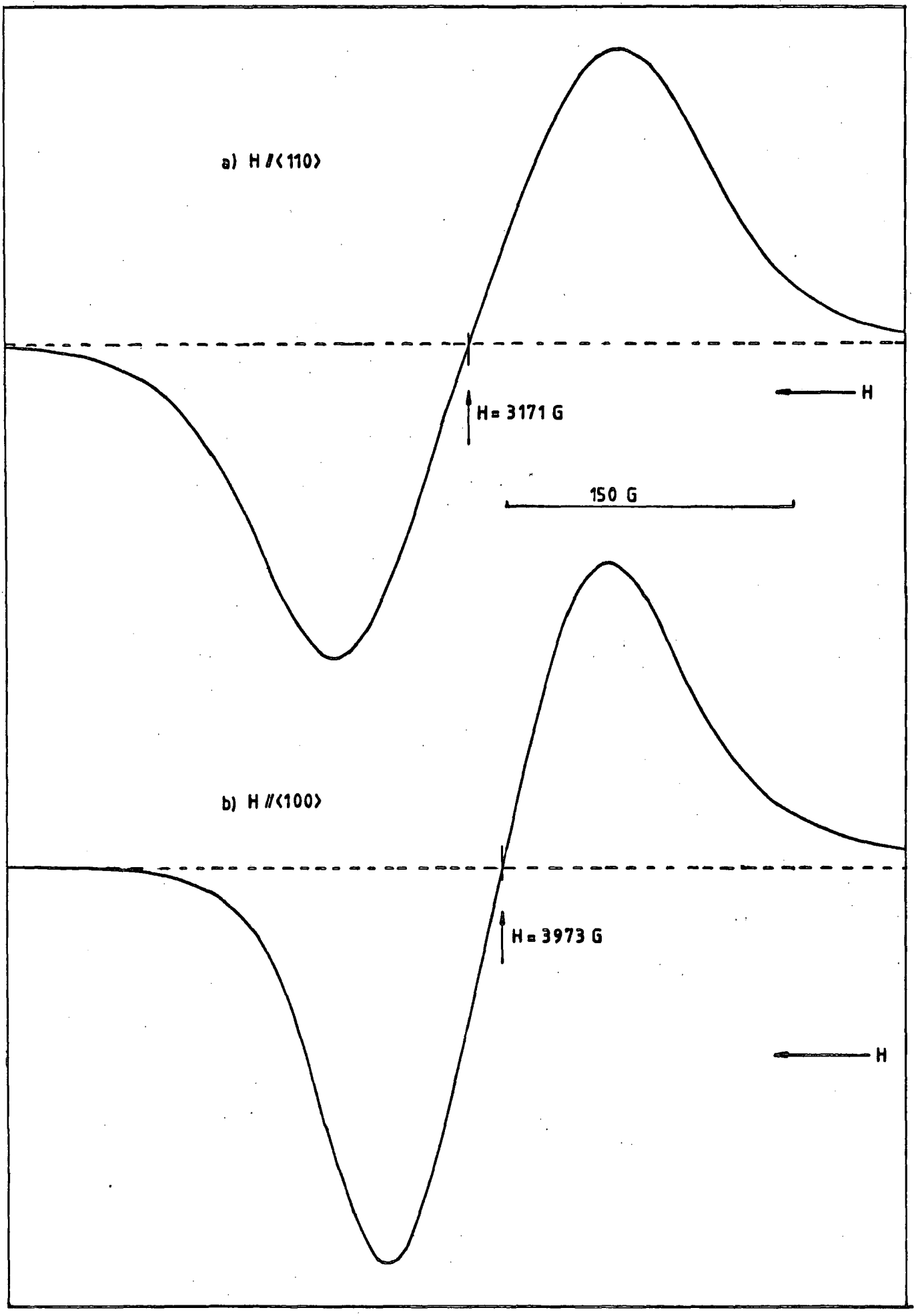

Figure 7.6 Spectra from 4300 ppm sample, aged 24 hrs., 800°C: 9.217 GHz: 113 K

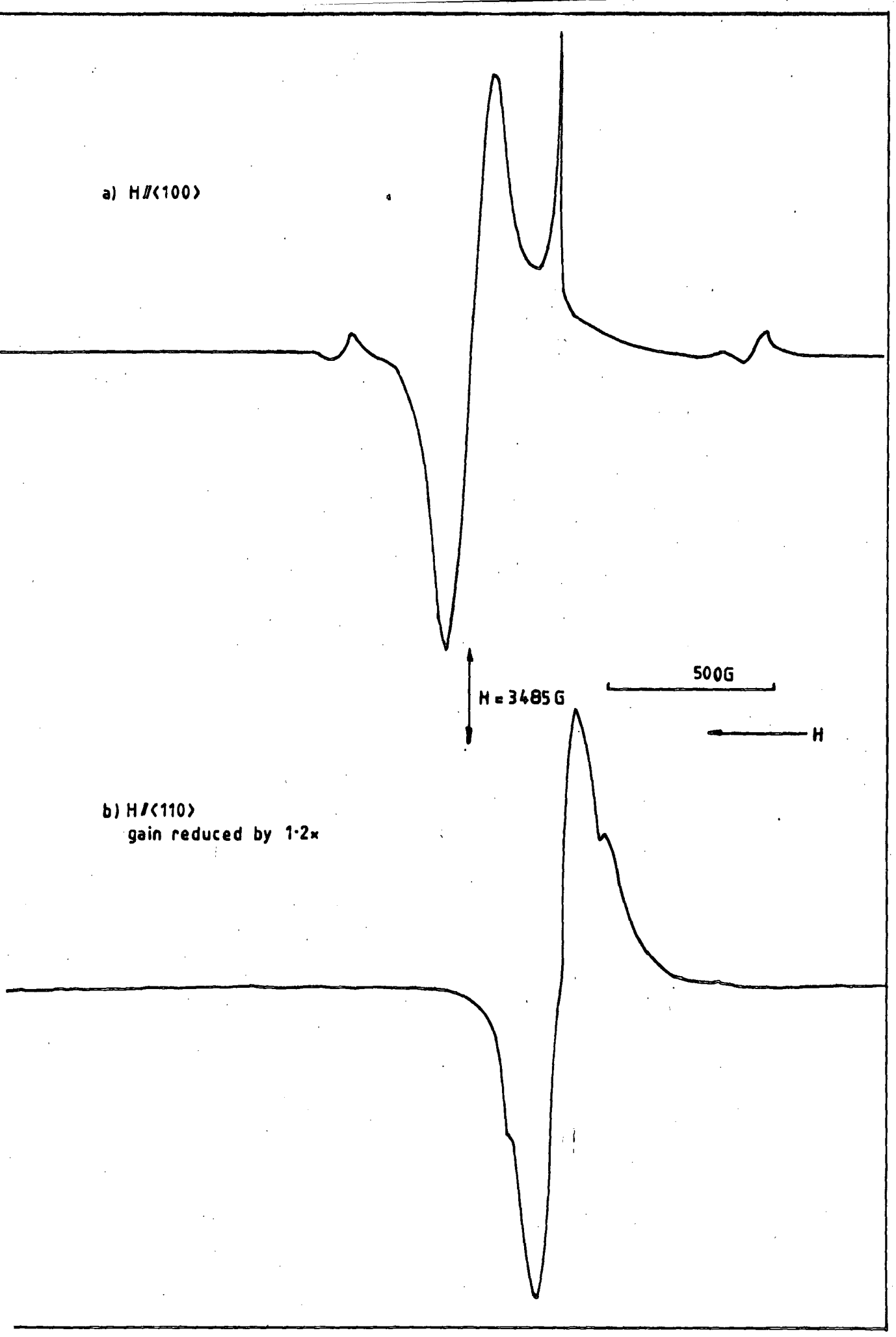

igure 7.7 Spectra from 2300 ppm sample, aged 15 mins, 800° C : 9.214 GHz : 293 K

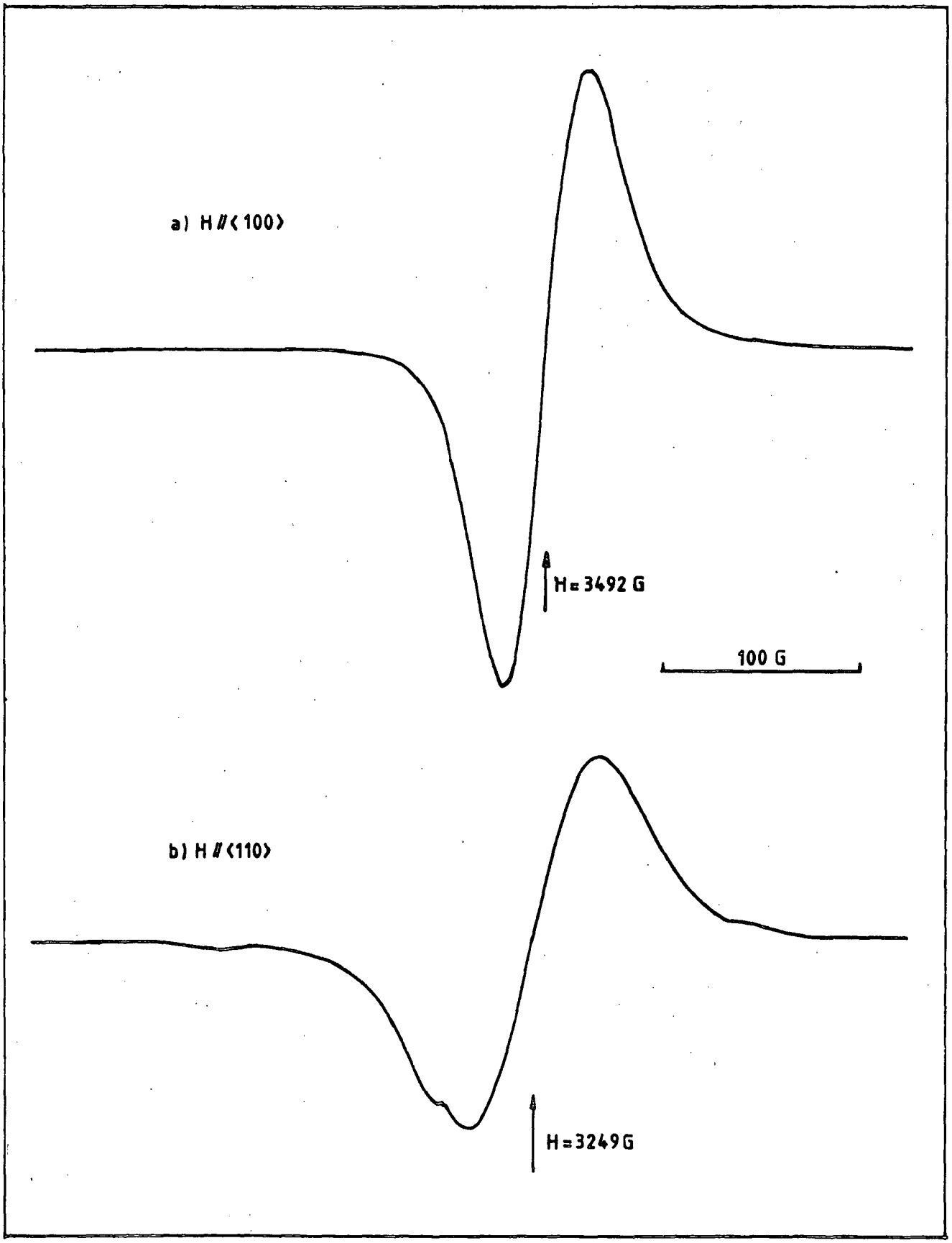

Figure 7.8 Spectra from 2300 ppm sample, aged 1 hr, 800°C : 9.214 GHz : 270K
Gain of both reduced by 32×, c.f. fig 7.7a).

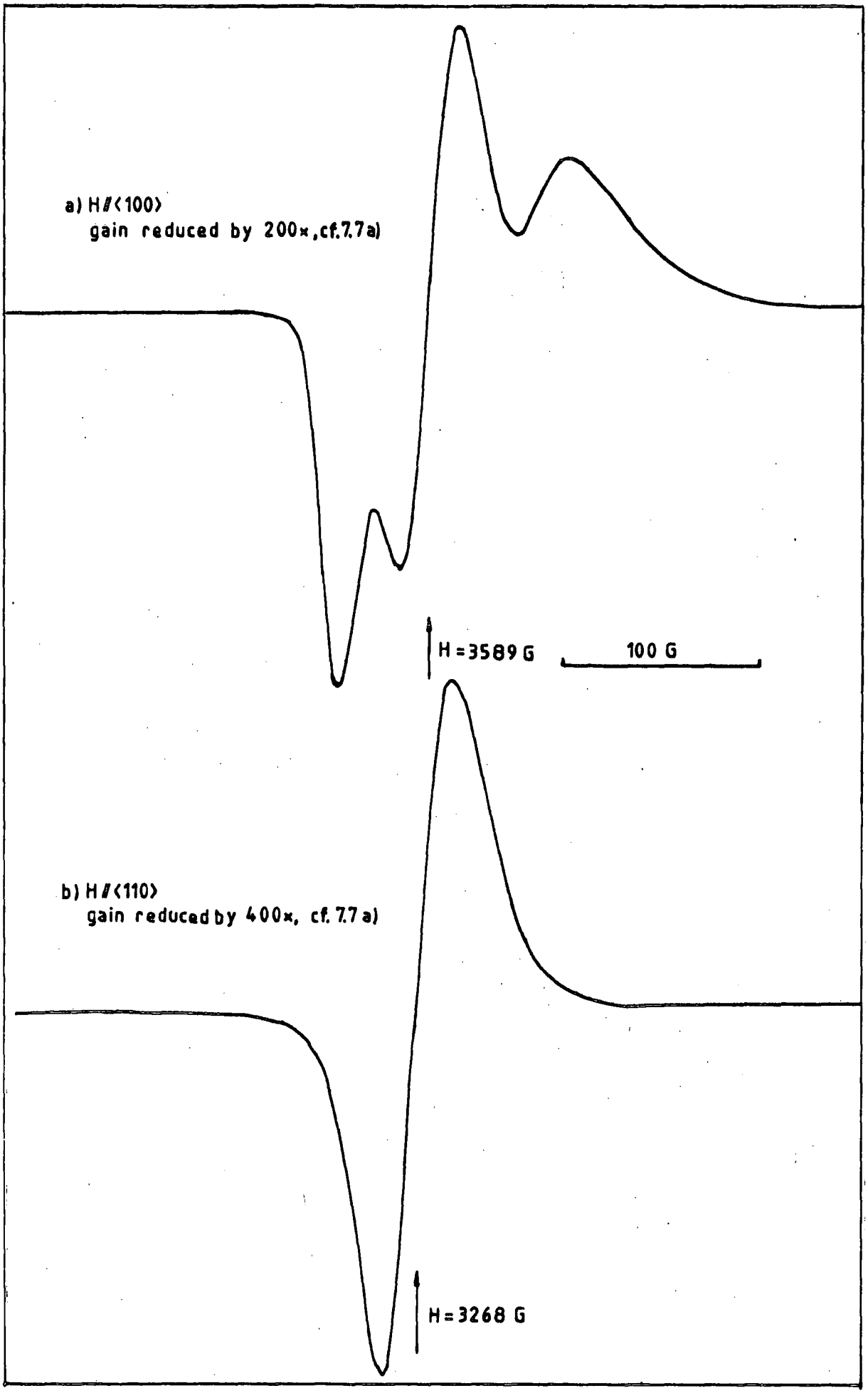

Figure 7.9 Spectra from 2300 ppm sample, aged 10 hr, 800°C : 9.214 GHz : 293 K

anisotropy, then rotation to the ⟨100⟩ orientation would lead to relative movement of the two lines, and a consequent change of symmetry. In this context it is of interest to examine the behaviour of the 2300 ppm sample.

After fifteen minutes aging the 2300 ppm sample shows, besides the Fe^{3+} cubic site spectrum, a FMR line which is anisotropic. Because of the overlap with, and similarity in intensity to, the isolated ion spectrum it is not always possible to measure acccurately the centre-field and linewidth of this line. However, the behaviour appears to be similar to that of the 4300 ppm sample line, giving almost identical values of anisotropy field, and a similar variation in anisotropy with measurement temperature, and being narrower in the ⟨100⟩ than the ⟨110⟩ orientation. Continued aging enhances this line whilst the isolated ion line is reduced in intensity. Figures 7.7 and 7.8 show the growth of the FMR line, being spectra recorded after 15 minutes and 1 hour respectively.

Ten hours of aging introduces a second, broader, line overlying the first, which has now narrowed still further. The anisotropy of both lines is identical, as is the change of anisotropy of each with temperature, although the centre-field values are slightly different, the narrower line being a few gauss higher in field when distinguishable; that is, when in the ⟨100⟩ orientation. When the lines are recorded in the ⟨110⟩ orientation they overlap in such a way that they are quite indistinguishable, as is shown in Figure 7.9. It seems that the only reason the two are at all separable is the difference in behaviour of the widths of the two lines with sample rotation.

A further fourteen hours aging of this sample results in an

apparently single line similar to that detected from the 4300 ppm sample - i.e. one which appears to be a single symmetric line when recorded in the $\langle 110 \rangle$ orientation, but quite asymmetric in the $\langle 100 \rangle$ orientation. Comparison of Figures 7.6 and 7.9 suggests that this (apparently) single line is one which is gradually produced with aging as a consequence of the broader line narrowing and changing in intensity so that the two overlap and become difficult to distinguish. The difference between the two samples is once again explained by suggesting that the changes occur in the same order in both samples, but more quickly in the higher concentration samples. This could of course be tested by aging the 4300 ppm sample for very short times.

These observations on the 2300 ppm sample suggest that the analysis of the spectrum of the 4300 ppm was correct, especially when it is noted that the values of anisotropy field and the way in which the anisotropy varies with temperature are almost identical in the two samples.

For the aging times employed the 310 ppm sample showed only the very earliest stages of precipitation - a weak anisotropic FMR line appearing beside the isolated ion spectrum after 24 hours aging.

7.3 Summary

The way in which these spectra may be related to the precipitates, and the ways in which changes in spectra may be used to infer changes in precipitation are discussed in the next chapter following an outline of the theory of ferrimagnetic resonance with particular reference to superparamagnetic particles. We conclude this

chapter with a brief summary of the effects of aging as follows : -

(i) Aging at 700°C produces precipitation in all except the 4N and 310 ppm samples, within one hour.

(ii) The resulting ferrimagnetic line is narrow (20 - 39 gauss) and isotropic.

(iii) It appears that all samples are affected similarily, the difference in intensity of the lines being apparently related to both aging time and iron concentration.

(iv) Extending the aging to much longer times leads to the appearance of a second, broad, anisotropic line.

(v) Aging at 800°C produces no effect on the 4N sample at times as long as 24 hours, but produces FMR spectral lines in all other samples.

(v) The way in which the spectral lines develop with time in the high concentration samples apparently follows a similar pattern to that which occurs when aging is at 700°C, but the changes take place more quickly.

(vi) The spectral lines produced in the middle range samples (310, 2300 and 4300 ppm) on aging at 800°C behave differently from the lines produced in the higher concentration samples, although it may be that continued aging would alter this picture.

CHAPTER 8

FMR : Analysis of the Experimental Results

8.1 Ferrimagnetic resonance absorption.

Wangsness (77-81) has shown that the observed behaviour of the resonance absorption of materials such as magnesium ferrite may be satisfactorily accounted for in terms of the classical approach initially proposed by Kittel (82-84) to explain the behaviour of ferromagnetic materials. This classical approach to ferromagnetic resonance has been justified by various workers (85-88) who, by quantum mechanical methods have obtained the same result as Kittel.

In a ferro- or ferri-magnetic material the magnetic ions are aligned under the influence of exchange forces, and the sample exhibits a bulk magnetisation. In the presence of a large enough static field the magnetisation will be the saturation value, and will be aligned parallel to the applied field. For the case of a material such as magnesioferrite the resultant magnetisation will be the vector sum of the magnetisations of the two sublattices, which are oppositely aligned. Since these two magnetisations may vary differently with temperature, it is possible that there will be a temperature at which the two will be exactly equal and opposite, and so the effect of each will be to cancel the other and the material will appear to be antiferromagnetic. Provided we are well clear of such a 'compensation point' though the nett magnetisation vector will behave to all intents and purposes like the magnetisation vector of a ferromagnetic material.

If a small perturbing field is applied at right angles to the static field the magnetisation vector will be disturbed from its equilibrium position, and will then precess about the direction of the applied field, gradually spiralling back in to its previous alignment as it loses energy under the influence of damping mechanisms. If the perturbing field is not merely a single pulse but a repetitive one of frequency ω , then when ω is similar to the precessional frequency energy will be coupled in to the precessing spins, and a large amplitude precession may build up, limited only by the damping of the system. It is important if we wish to excite only this low frequency response of the system that the magnitude of the perturbing field is small compared with the static field; and that the sample is of such a size that it may be regarded as small compared with the wavelength of the microwave radiation within the sample.

Under these circumstances the condition for ferrimagnetic resonance is given (83), for the simple case of a spherical sample, by

$$\omega = \gamma_{eff} H_{res} \qquad 8.1$$

where ω gives the microwave freqency, γ_{eff} is the magnetomechanical ratio for an electron spin, and H_{res} is the field at the sample required for resonance. The value of H_{res} is dictated by ω/γ_{eff}, and is not necessarily - indeed is seldom - exactly equal to the value of static field H_s which has to be applied to obtain resonance. The discrepancy between H_{res} and H_s arises as a consequence of the demagnetising field of the sample, and the magnetocrystalline anisotropy, which is discussed in some detail in the next section.

The effective magnetomechanical ratio is so labelled because

it is based on an effective g-value (g_{eff}) which is a mean value of spectroscopic splitting factor depedent upon the individual g-values of the various ions on the different types of site, and their distribution between the sites. In fact if the g-values appropriate to the ions on each of the types of site are known, for example from paramagnetic resonance experiments, then measurement of g_{eff} will allow the determination of the distribution of the cations between the various sites in the spinel structure.

8.2 Magnetocrystalline Anisotropy and Resonance

Even in the absence of an external field the magnetic characteristics of a ferrite are anisotropic, as a result of the magnetic interaction between spin and orbital moments, since the latter are coupled to the crystal lattice. Consequently it is easier to magnetise this type of material in some crystallographic directions than in others, the symmetry of the anisotropy being related to the symmetry of the lattice.

The observed effect which this has upon the magnetic resonance is to cause the value of static field which must be applied to produce resonance to vary with crystal orientation within the static field, for a fixed frequency of microwave radiation. A convenient way of coping with this is to rewrite the equation of 8.1 as

$$\frac{\omega}{\gamma_{eff}} = \left[H_s + H_a\right] = H_{res} \qquad 8.2$$

Here H_{res} is the field at which resonance occurs, determined by ω/γ_{eff}, H_s is the external field to be applied to the sample and

H_a the effective 'anisotropy field'.

The way in which H_s varies with orientation for a material such as magnesioferrite is illustrated by the three-dimensional surface portrayed in Figure 8.1. If one imagines the field applied always through the origin of the crystallographic axes shown then the distance from the origin to the surface represents the relative magnitude of the static field required to produce resonance in that orientation. Were the resonance field H_{res} also to be portrayed on the same diagram, and to the same scale, then it would comprise a sphere, centred on the origin and with a radius which would locate the surface somewhere between the maximum values of H_s along the $\langle 100 \rangle$ directions and the minima in the $\langle 111 \rangle$ directions.

We have discussed the anisotropy so far in terms of the effective 'anisotropy field', since that is what is measured in a resonance experiment. An alternative approach is to consider the free energy of the crystal, in which case we must add to the free energy a term the magnitude of which will depend upon the direction of magnetisation with respect to the crystal axes. We should also strictly include a second component which arises out of the stresses due to manetostriction. The sum of these two terms is the total anisotropy energy, which may be expressed in terms of the anisotropy constants K, the magnetisation, and an angular function.

It is shown in the standard texts (89) that when the applied field H_s is large enough and applied in a $\langle 100 \rangle$ plane of a cubic crystal then to a very good approximation

$$H_s = \frac{\omega}{\gamma_{eff}} - \frac{K_1}{M_s} \cdot \frac{1}{2}\left[\frac{3}{2} + \frac{5}{2}\cos 4\phi\right] \qquad 8.3$$

where the second term on the right hand side is that which we

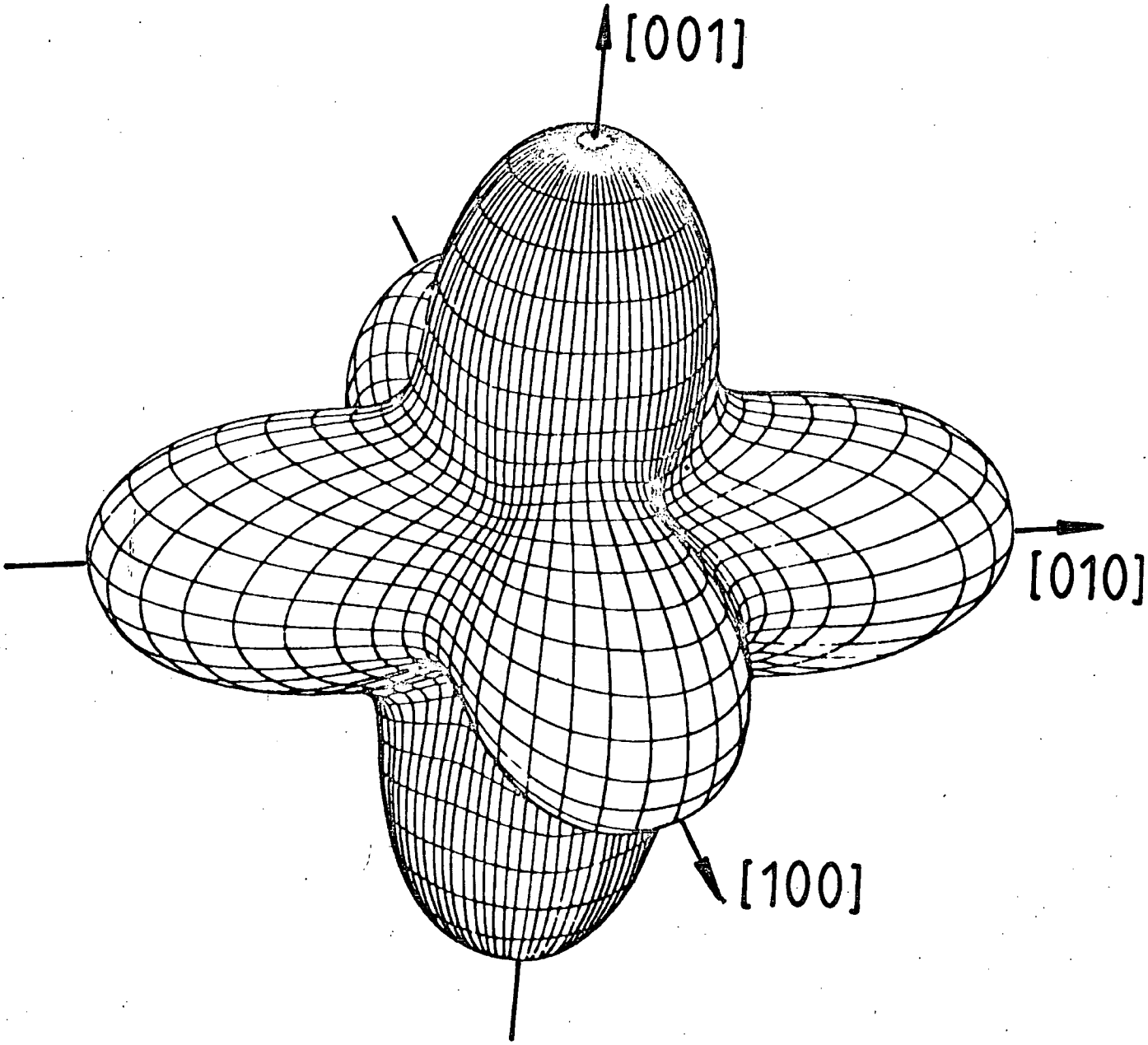

Figure 8.1 Anisotropy Surface (cubic)

previously called the effective anisotropy field, but which is now expressed in terms of the first anisotropy constant K_1, the saturation magnetisation M_s, and the angle ϕ between both H_s and the steady magnetisation vector and the $\langle 001 \rangle$ axis. The limiting condition on H_s mentioned above is that $H_s \gg K_1/M_s$. Following de Biasi (72) and others we have assumed that the second anisotropy constant K_2 is negligible.

In a magnetic resonance experiment the resonance field is usually measured for several orientations of applied field and for various sample geometries and analysis of the results enables one to calculate the unknowns K_1, M_s, and g_{eff}, so characterising the material. Our case is somewhat complicated however by the fact that we are dealing with very small precipitates, which are expected to be superparamagnetic and will not therefore behave in the same manner as bulk magnesioferrite. This problem is dealt with in more detail in Section 8.3.

When H_s is applied along the $\langle 001 \rangle$ and $\langle 101 \rangle$ directions then equation 8.3 reduces respectively to

$$H_{s\langle 001 \rangle} = \frac{\omega}{\gamma_{eff}} - \frac{2K_1}{M_s} \qquad 8.4a$$

$$H_{s\langle 101 \rangle} = \frac{\omega}{\gamma_{eff}} + \frac{K_1}{2M_s} \qquad 8.4b$$

and combining these leads to

$$\frac{K_1}{M_s} = \frac{H_{s\langle 101 \rangle} - H_{s\langle 001 \rangle}}{2.5} \qquad 8.5$$

Hence the measurement of H_s for two such orientations of the crystal will allow the determination of K_1/M_s, assuming that the

demagnetising field due to shape effects, the magnetostrictive effect, and the second anisotropy constant are all negligible. De Biasi (75) has suggested that these are useful approximations in the case of magnesioferrite precipitated from MgO which has been aged for reasonably long times in air. The question as to how long a time is a 'reasonably long time' is discussed later.

8.3 Superparamagnetism.

The magnesioferrite precipitates with which we are dealing are so small that they can be expected to behave as superparamagnetic single domain particles (23,73). The lack of domain structure is a consequence of the 'trade-off' between the magnetostatic self-energy of the particle and the energy required to form a domain wall in opposition to the exchange forces which attempt to align the spins (90). Various workers have discussed such particles, and the ways in which their behaviour can be expected to differ from that of bulk material (75,91-93).

The important difference is that since the anisotropy energy of the particles is directly proportional to the particle volume very small particles have relatively very small anisotropy energies. If the volume is so small that the anisotropy energy is of the same order as the thermal energy of the particles then the direction of magnetisation of the particles will undergo thermal fluctuations. Consequently the anisotropy field which is measured for a coherent assembly of small non-interacting particles, fixed in position in a diamagnetic matrix, will be reduced compared with the value of anisotropy field which would be measured for the bulk material.

If we follow both the approach and the nomenclature of de Biasi (75) then we may show that the relationship between the value of anisotropy field H_a^{sp} measured for the small particle case is related to H_a, that which would be obtained for the bulk case, by the relation

$$\frac{H_a^{sp}}{H_a} = \frac{1 - 10X^{-1}\coth X + 45X^{-2} - 105X^{-3}\coth X + 105X^{-4}}{\coth X - X^{-1}} \qquad 8.6$$

where $X = I_s \bar{V} H_s / kT$, I_s being the magnetisation and $\bar{V}$ the mean volume of the particles, H the applied field strength and k,T Boltzman's constant and absolute temperature.

We have once again made the assumption that the particles are spherical in shape; and in addition that all particles have the same magnetisation and volume. The way in which H_a^{sp} approaches H_a as the volume of the particles is increased is shown in Figure 8.2, where H_a^{sp}/H_a is plotted as a function of X, the solid line showing the theoretical relationship. The derivation of the experimental points is explained in the next section; they were obtained from the observed anisotropy data using curve-fitting techniques.

8.4 The FMR Results : Anisotropy and Aging Time.

The results of the FMR experiments which were outlined in Chapter 7 do not present a straightforward picture for analysis. It would seem that the behaviour of the samples aged at 700°C was similar to that of the high iron concentration samples aged at 800°C, as far as can be assessed from the FMR spectrum, although the changes in the spectrum, which presumably relate to the changes in the precipitate, took longer to appear at the lower temperature. However, although the behaviour is consistent from sample to sample, and at both temperatures for these samples, there is clearly a problem in

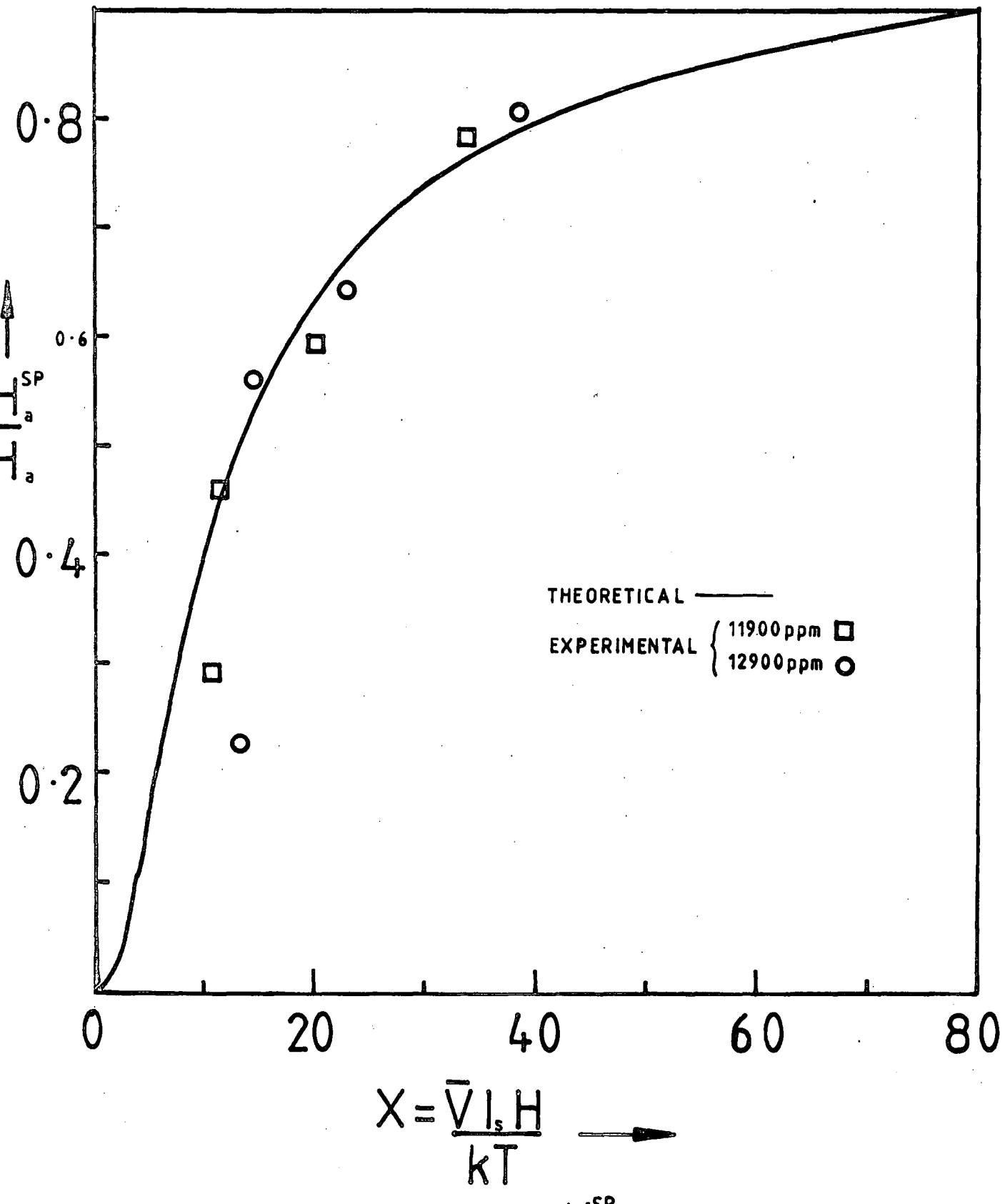

igure 8.2 Variation of $\frac{H_a^{SP}}{H_a}$ with X.

that one of the lines recorded is isotropic; and we have pointed out in Section 8.2 that a FMR line is expected to be anisotropic. The origin of the isotropic line is not at present understood.

On the other hand the low iron concentration (310, 2300, and 4300 ppm) samples behave differently from the high concentration samples when aged at 800°C. No isotropic line appears, but two anisotropic lines do appear in the spectrum of the 2300 and 4300 ppm samples. The line obtained from the 310 ppm sample has not been analysed in detail as it is so weak, but it does appear to follow the behaviour of the single anisotropic line which is obtained from the 2300 ppm sample after short aging times. The anisotropy field measured for these lower concentration samples does not behave according to the theory outlined in the previous sections of this chapter. We find that although the anisotropy field, which is identical for both the lines, increases with aging time initially it does go through a maximum, after which it decreases. It is thought that this is a result of changes in the chemical form or cation distribution which take place during the early stages of the precipitation.

However the lines obtained from the two highest concentration samples following aging at 800°C do behave more or less as predicted, so we have analysed the behaviour of these lines in some detail. The measured anisotropy field is expected to change with the volume of precipitate, and since these two factors may be considered to be the two variables related by equation 8.6 it should be possible, with our knowledge of the anisotropy field to extract useful information regarding the precipitate volume. However, it is clear that besides these two variables Equation 8.6 contains two

unknowns - the anisotropy field for the bulk material and the magnetisation, each of which will be a function of chemical composition of the precipitates and the measurement temperature.

De Biasi has outlined a useful way of approaching this problem (72). Having measured the anisotropy field for various aging times one then assumes

i). that the volume increases linearly with time according to the relation

$$V = A + Bt \qquad 8.7$$

where A and B are constants (For long aging times this is consistent with coarsening theory (94))

ii). that the chemical composition and the magnetisation are unaffected by the growth of the precipitates.

The variables in equation 8.6 then become the measured anisotropy field and aging time. Curve fitting techniques may then be used to fit the experimental values of anisotropy field and aging time to the theoretical curve of equation 8.6, allowing the subsequent determination of the unknown constant parameters.

We have adopted this approach to analyse the anisotropic lines obtained from the 11900 and 12900 ppm iron samples, using a least-squares curve fitting computer programme. With so little data on any one individual specimen one cannot put too much emphasis on the results of this exercise but it is of interest because it allows us to compare our results, where the aging was carried out in oxygen, with those of de Biasi, who carried out the aging process in air. The

measured data values used in the computation are shown in Table 8.1.

The particular programme used included a facility for adjusting the weighting which was given to each of the data sets. It is interesting to note that for both samples by far the best fits to the curve (as assessed by a built-in 'Chi-squared test') were obtained when the first set of data, recorded after only fifteen minutes aging, was very lightly weighted in comparison with all the other sets. The nett effect of this may be seen in diagram 8.2 where the data points for each sample are shown, fitted to the curve of equation 8.6. The lightly-weighted data points lie a relatively long way from the curve. This could be interpreted in various ways.

One possibility is that the assumption, that the increase of volume of the precipitates with time is a linear process for all aging times investigated, is erroneous. This is of interest because there is some discussion in the literature regarding the times at which a linear aging process actually commences (23,73). However there are other possibilities; for example, it could be that when the precipitates are small the assumption that the shape anisotropy is negligible in comparison with the magnetocrystalline anisotropy may no longer hold. We are unable to distinguish here between the two possibilities, but the problem could possibly be resolved by taking many more sets of readings at very short aging times and looking for a fit between the data and a theoretical curve which takes into account both the shape and the magnetocrystalline anisotropy.

By assuming reasonable values of 3300 gauss and 300 K for H and T in equation 8.6 we may use the fitted data points to determine values of H_a and I_s. The parameters A and B which relate to the volume growth rate of the precipitates are given by the computer

TABLE 8.1 : Experimental data values used in curve fitting.

Aging time (hour)	Measured Anisotropy Field, H_a^{sp} (Gauss)	
	11900 ppm Sample	12900 ppm Sample
0.25	-32.8	-23.6
1.00	-52	-58.5
10.00	-67.2	-66.8
24.00	-88.8	-84.4

TABLE 8.2 : Parameters determined by curve-fitting.

Parameter	Value		
	11,900 ppm Sample	12,900 ppm Sample	de Biasi (73)
A (cm^3)	4.8×10^{-19}	6.2×10^{-19}	6×10^{-19}
B ($cm^3\ hr^{-1}$)	4.6×10^{-20}	4.8×10^{-20}	4×10^{-20}
H_a (Gauss)	113	104	
I_s	258	258	262

Figure 8.3 Variation of mean precipitate volume with time

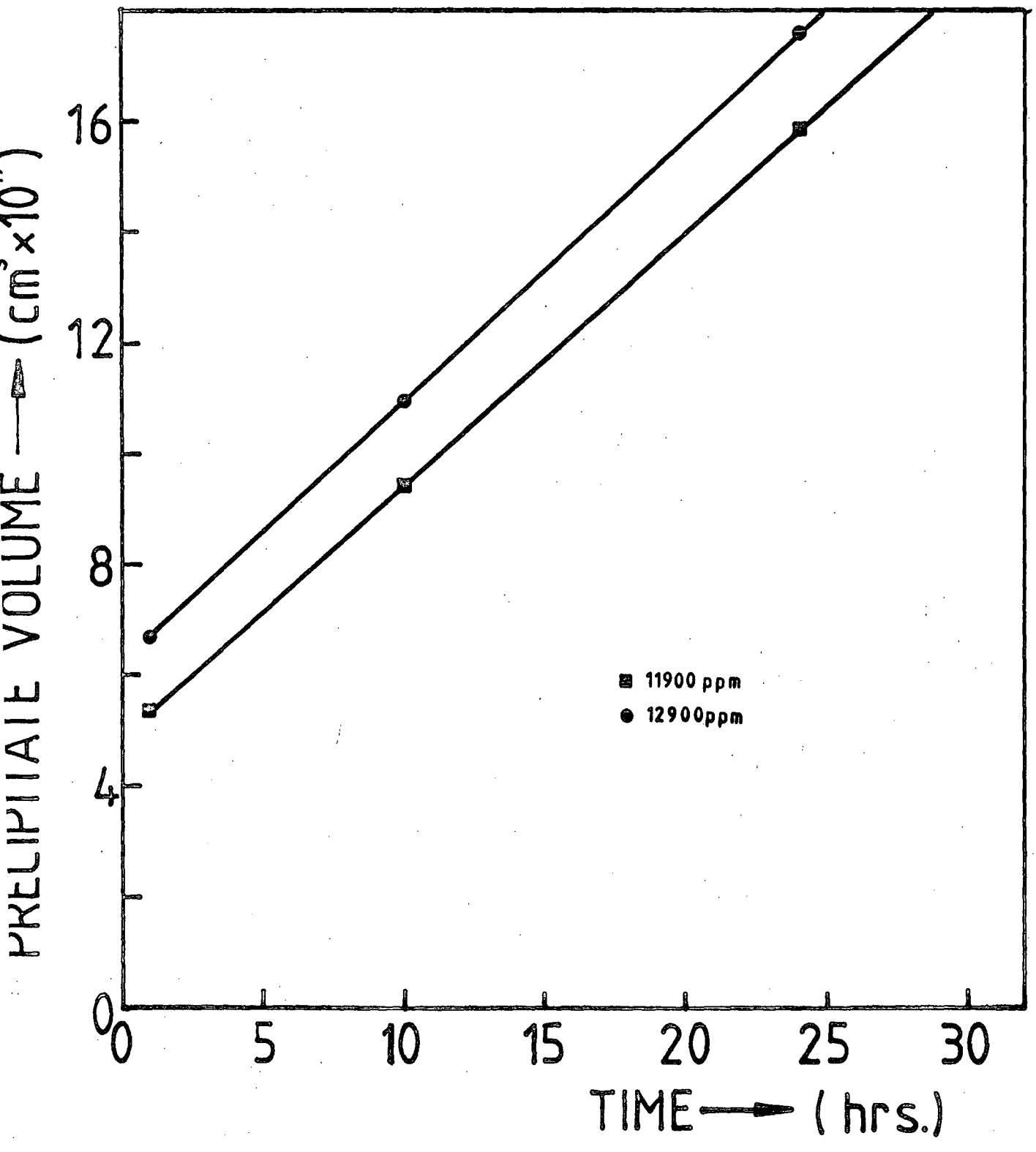

programme for any fit to the curve, and so we may determine the volume at any time. The closeness with which the experimental points fit to the curve is relatively insensitive to the value of the parameter B, a roughly similar fit, as assessed by the Chi-squared test, being achieved for a range of 25% about a mean value. The values which we have obtained for the various parameters are given in Table 8.2, where some of de Biasi's data is also shown for comparison, and it can be seen that despite the imprecision of our values there is good agreement between his figures and ours. The variation in precipitate volume with aging time is plotted on the graph in Figure 8.3. It should of course be remembered that not all particles will have the same volume; the volumes will be distributed about a mean value.

8.5 The FMR Results : Anisotropy and Temperature.

For bulk material of the same composition as the precipitates the relationship between anisotropy field H_a, the first anisotropy constant K_1, and the magnetisation I_s is given by

$$H_a = K_1 / I_S \qquad 8.8$$

Since the magnetisation in this case is the vector sum of the magnetisation of the two sublattices we may write

$$H_a = K_1 / (I_A + I_B) \qquad 8.9$$

K_1, I_A and I_B will all be temperature dependent, and therefore we expect a variation in H_a with temperature. It is difficult to predict the precise form this variation should take, since K_1 is not

a simple function of temperature (95,96). It is even more difficult to predict the variation in the value of anisotropy field for an assembly of coherent small particles, which is the anisotropy field we have measured, since this is itself a relatively complicated, temperature dependent, function of the bulk parameter (see equation 8.6). It comes as something of a surprise therefore to find that for all the samples aged at 800°C the effective anisotropy field measured across the temperature range 100 - 420 K follows the simple relation

$$\sqrt{|H_a^{sp}|} = C + DT \qquad 8.10$$

where $D = -0.045 \pm 0.004\ G^{1/2} K^{-1}$, T is the absolute temperature, and C varies from sample to sample. This relationship apparently holds for samples of all concentrations of iron from 2300 - 12900 ppm, notwithstanding the discussion at the start of the previous section, where it was mentioned that both the measured values of anisotropy field and the way in which these varied with temperature differed from sample to sample.

In diagram 8.4 we show the relationship between anisotropy field and temperature for various samples, measured after 24 hours aging at 800°C. If we assume that the intercept of the plotted line with the temperature axis gives the Curie temperature, T_c, then we may rewrite equation 8.10 as

$$\sqrt{|H_a^{sp}|} = C(1 - \frac{T}{T_c}) \qquad 8.11$$

We obtain a value of T_c from the graph of 500 ± 10 K for the 11900

Figure 8.4 Variation of measured anisotropy field with temperature

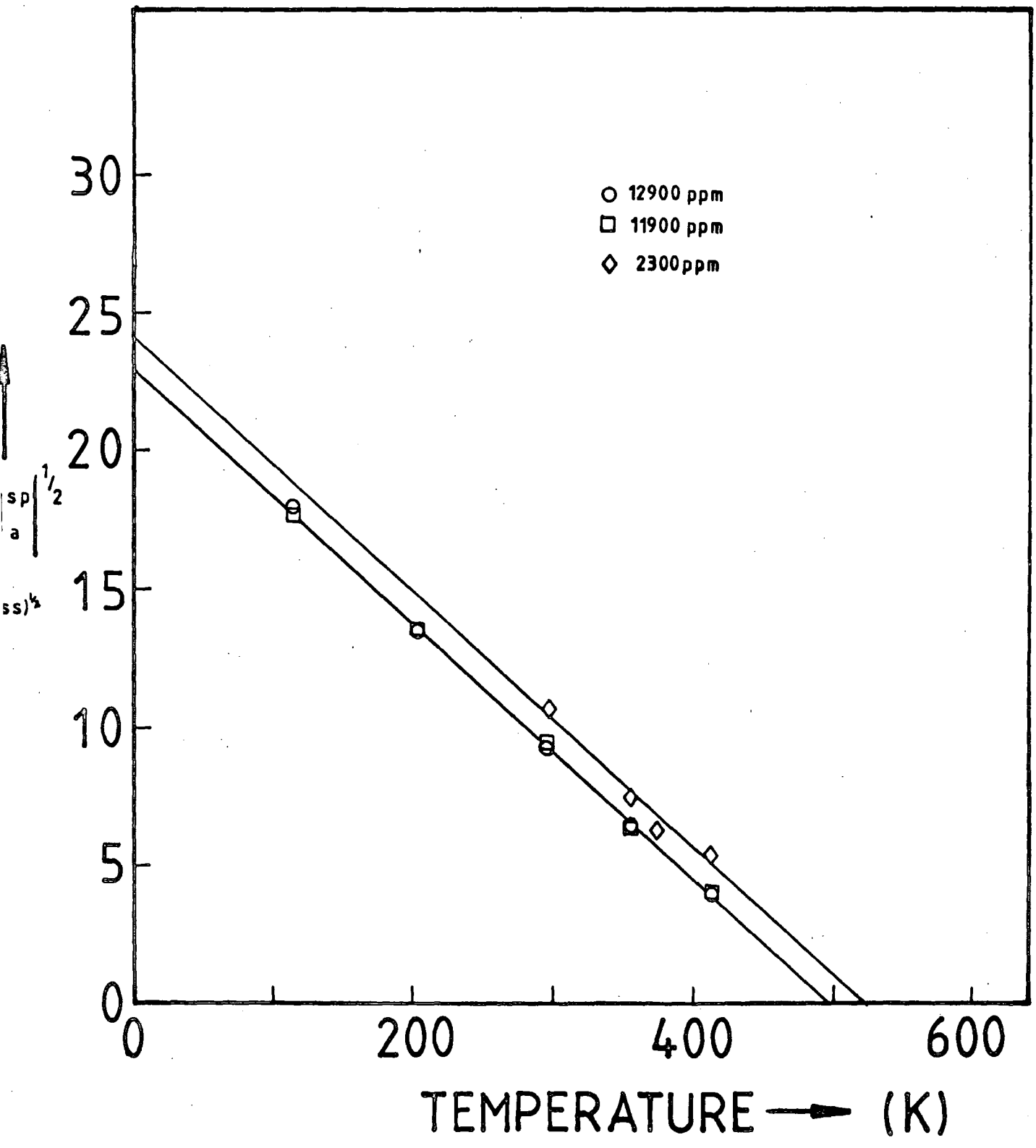

and 12900 ppm iron samples. This compares well with the value of Curie temperature of 490 K, determined by Wirtz and Fine (23) for magnesioferrite precipitates in sintered polycrystalline spheres of MgO containing 1 cation% iron aged at 800°C.

8.6 Characterisation of the Precipitates.

Wirtz and Fine (23) have shown that for magnesioferrite precipitated from iron doped MgO the Curie temperature is given by the empirical relation

$$T_c = 200 + 490(1 - \rho x) \quad K \qquad 8.12$$

where x is the compositon parameter in the chemical formula $Mg_xFe_{3-x}O_{4-(x-1)/2}$ and ρ is the fraction of Mg^{2+} ions located on tetrahedral sites. Whilst knowledge of the Curie temperature alone is insufficient to allow us to separate ρ and x, our measured value of Curie temperature is, at 500 K, close enough to that of Wirtz and Fine to give the same value of the product ρx. We are not strictly justified in proceeding further with the analysis without additonal information - for example from magnetometry measurements - since having aged in oxygen it may be that x is different from the value found by Wirtz and Fine, and this in turn would affect our value of ρ. However, if we make the assumption that as a result of aging at the same temperature as Wirtz and Fine we will obtain the same fractional cation distribution, and take $\rho = 0.30$, then we obtain a value for the composition parameter of x = 1.29.

If we assume that all the iron is in the Fe^{3+} state, that none of the other ions contribute a magnetic moment of significance,

and that each Fe^{3+} ion will contribute 5 Bohr magnetons, then we obtain a value of 2.42 Bohr magnetons per formula unit for the magnetic moment. Taking a lattice parameter of 8.4 Å yields a magnetisation at 0 K of 303 emu cm^{-3}. Wirtz and Fine (23) give 310 emu cm^{-3}. If we extrapolate our value of 303 emu cm^{-3} to room temperature we obtain a value of I_s = 252 emu cm^{-3} as compared with the value computed for these samples in section 8.4 of approximately 258 emu cm^{-3}. Taking 255 emu cm^{-3} for the room temperature magnetisation allows us to use the relation $K_1 = H_a/I_s$ to determine values of the anisotropy constant at room temperature of -3.0×10^4 and -2.8×10^4 erg cm^{-3} for the 11900 and 12900 ppm iron doped samples, respectively. These compare favourably with a room temperature value of about -3.2×10^4 erg cm^{-3} given by Belson and Kriessman (95) for a single crystal of magnesioferrite.

De Biasi (76) has investigated experimentally the behaviour of the effective g-value of magnesioferrite precipitates in MgO, and finds that it decreases with increasing deviation from stoichiometry. We may use his plot of g vs. composition parameter x to predict the g-value for our precipitates. With x = 1.29 we obtain g = 1.999; our measured value at room temperature for the effective g-value of the precipitates in the 12900 ppm iron sample is identical, providing strong confirmation that the composition parameters and cation distributions determined above are reasonable values.

8.7 The FMR Results : Linewidths.

The broad trends of the changes in width of the narrow spectral lines obtained at short aging times have been described in Chapter 7, although the way in which this line arises is not clear.

In addition, for the low iron concentration samples aged at 800°C the evidence suggests that whilst precipitates of magnesioferrite have formed, they have not attained equilibrium, at the longest aging times used, in terms of the chemical composition, or degree of inversion, or possibly both. Consequently, at this stage we can make little useful comment about the widths of any of these lines.

On the other hand the analysis of the previous three sections suggests that as far as the high iron concentration samples aged at 800°C are concerned, the precipitates may be characterised in some considerable detail, after aging times of one hour and upwards. It was suggested that for aging times of less than an hour at this temperature the precipitates had not attained their equilibrium stoicchiometry or inversion, but that from times of about one hour onwards the only change taking place was an increase in the mean volume of the precipitates. It is interesting to note that the changes in linewidths which take place may well bear out this analysis.

We have plotted the variation with aging time of the derivative peak-to-peak linewidth for the three highest concentration samples in diagram 8.5. The data *are* shown for two different crystal orientations, and for various measurement temperatures in the range 113 K to 413 K. It can be seen that for all three samples the values are virtually identical, as is the effect of aging; the linewidth increases at first, reaching a maximum after one hour. It then decreases continuously with continued aging. It is thought that the change in trend at the one-hour mark could be a result of the precipitates attaining their equilibrium stoichiometry and inversion at that time.

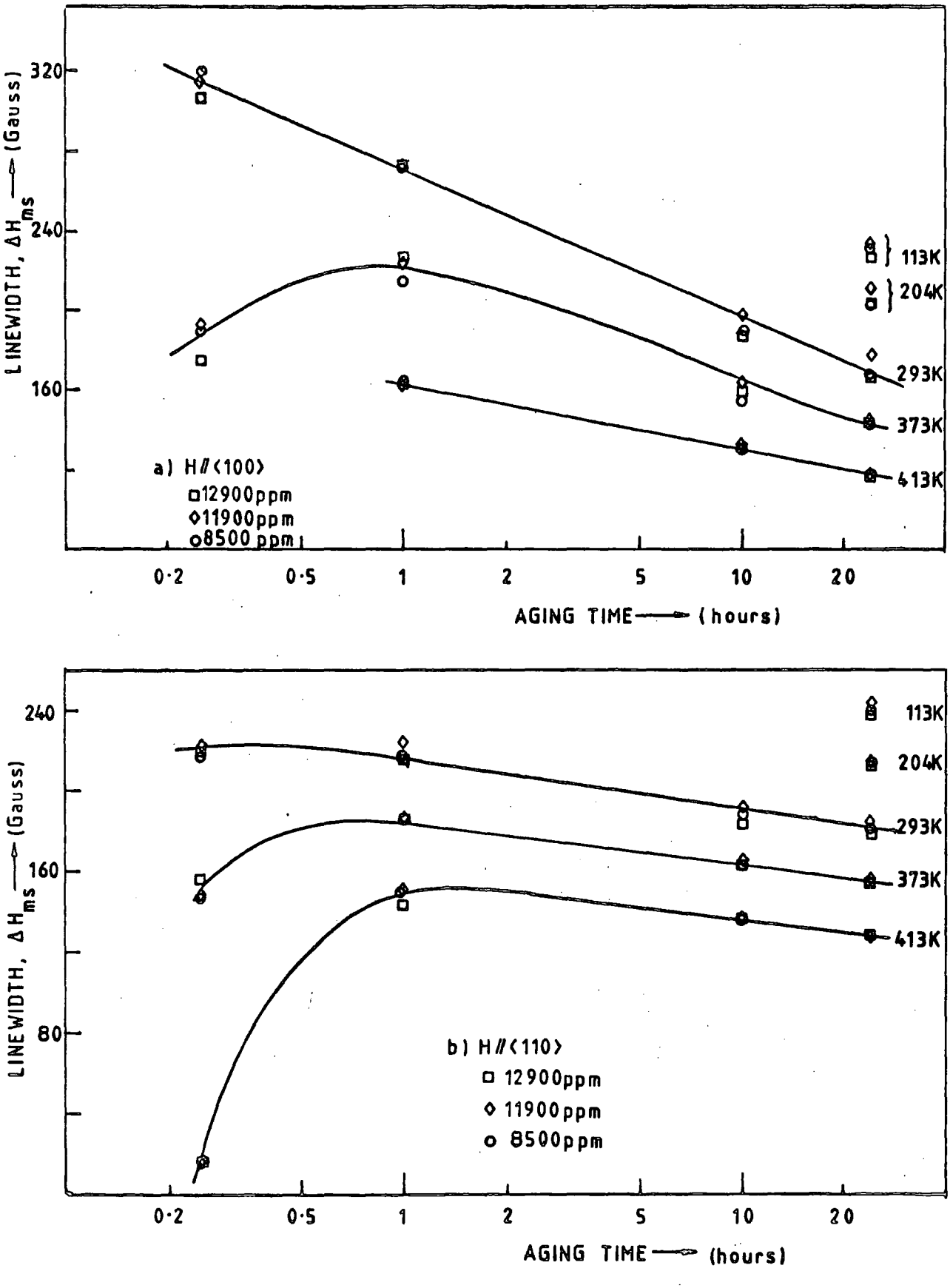

Figure 8.5 Variation of measured width of broad FMR line with aging time

Figure 8.6 Variation of measured width of broad FMR line with recording temperature.

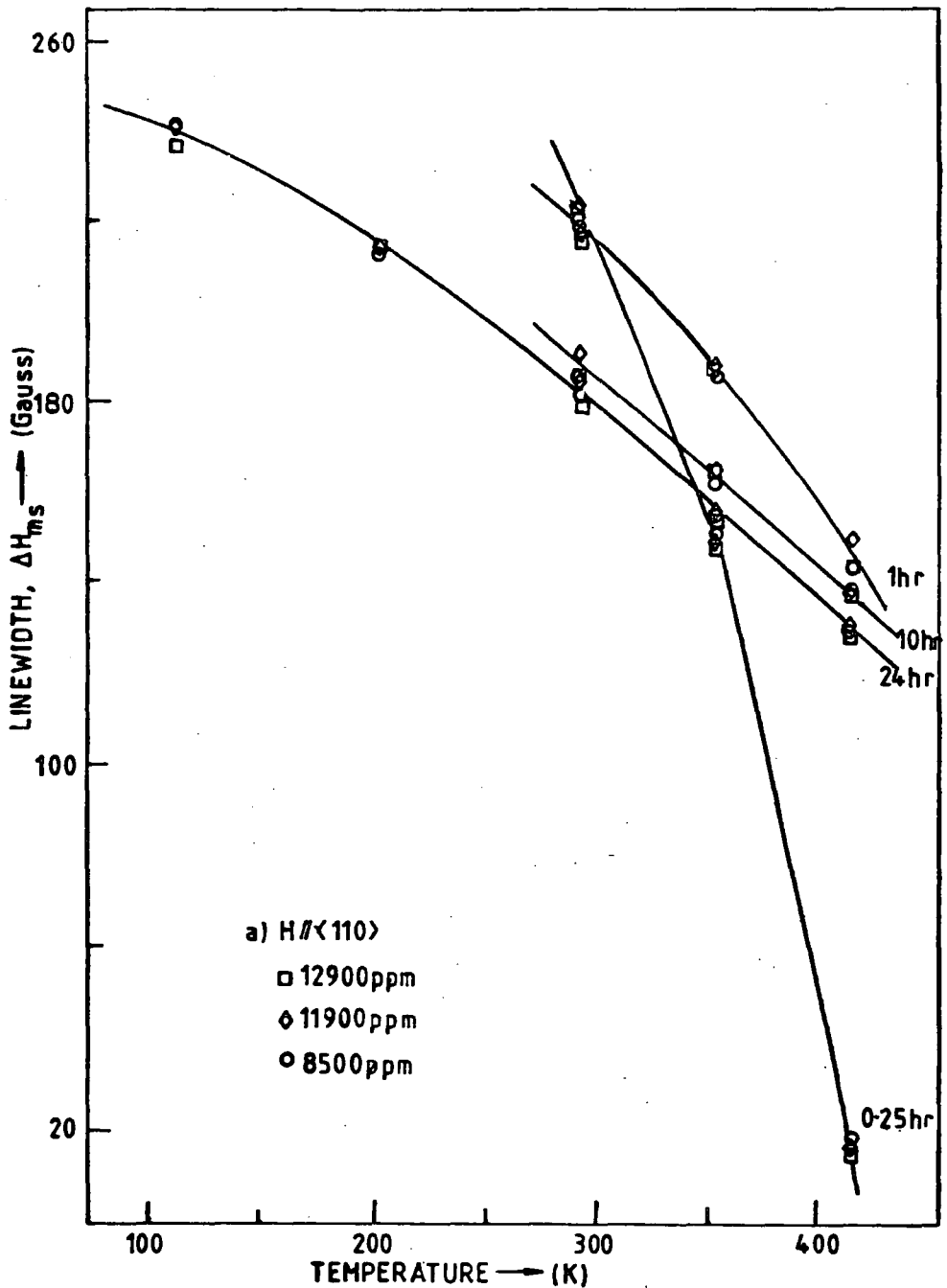

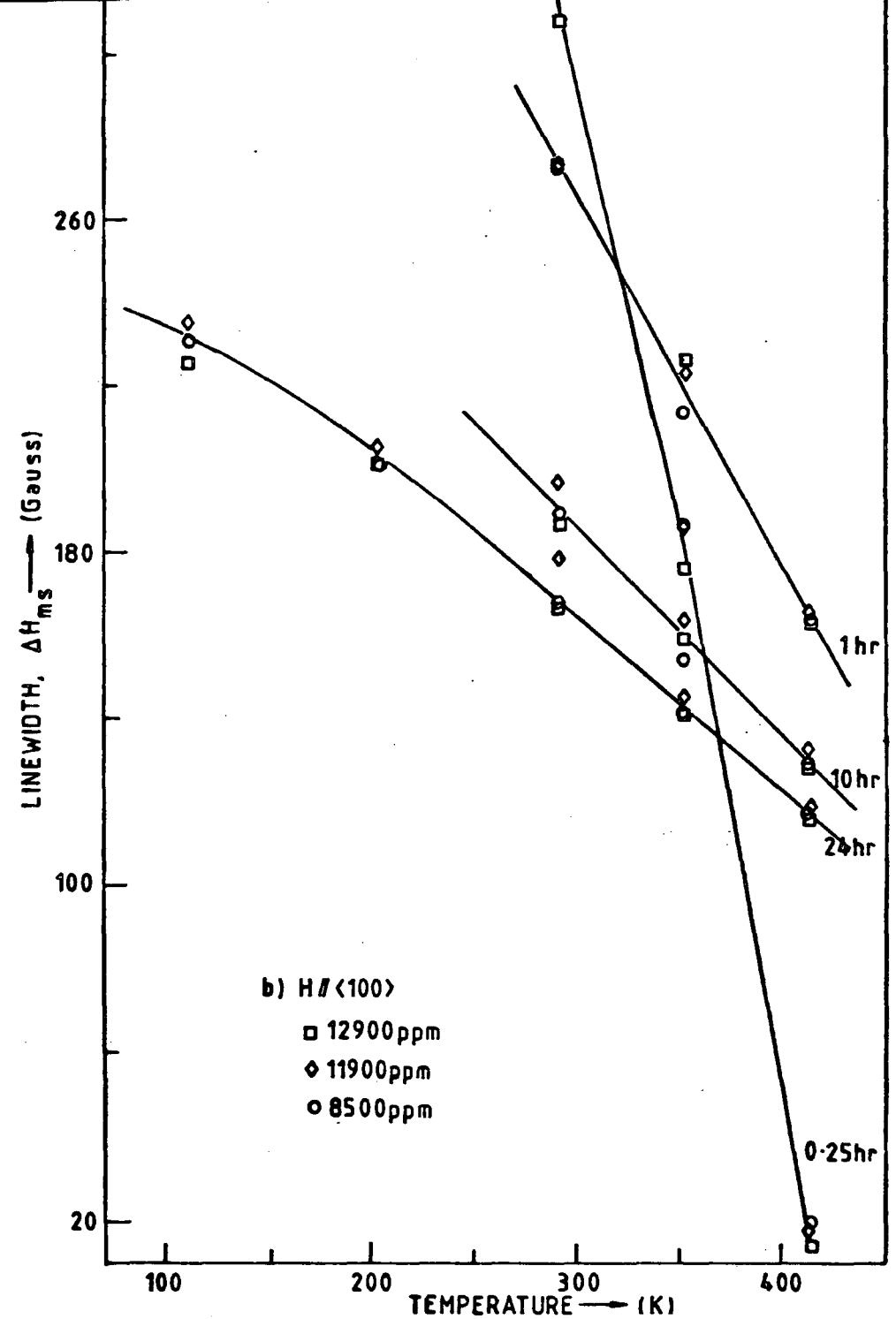

If this is so then one is tempted to suggest that the decrease in width from that time onwards is somehow a consequence of the growth alone. On the other hand, since we expect the mean volume of precipitate to vary with initial iron concentration (see Figure 8.3) any volume dependent factor which determined linewidth should lead to all three samples showing similar trends in width with aging, but quite different values of width at any one time. We do not find this in practise. One possible cause might be that in the early stages the precipitate comprises clusters which are chemically similar and which are close enough together to act rather like single crystals with voids, the 'voids' being the interpenetrating regions of ordinary MgO. The effect of voids such as these on the linewidth would be similar to the effects of porosity in polycrystalline ferrites (97); they would cause considerable line broadening. Presumably a consequence of continued aging would then be to fill these voids, reducing the 'effective porosity' and so narrowing the resonance line.

Measurements of linewidth over the temperature range 110 K - 413 K yield a continuous, almost linear, decrease in linewidth with increasing temperature for all three samples, at each stage of the aging (Figure 8.6). This result is quite at variance with that of Belson and Kriessman who found that with a polished single-crystal sphere of magnesioferrite the linewidths were independent of temperature. The reason for this discrepancy is not clear. Since the major difference between the our samples and that of Belson and Kriessman is that our samples are superparamagnetic whereas they used a relatively large single crystal, one imagines that the solution to this problem may lie in a fuller analysis of the superparamagnetic state.

There does not appear to be any data in the literature relating to the linewidths of a distribution of coherent superparamagnetic particles such as the ones we have investigated. In view of the consistency in the behaviour of our samples in terms of the FMR linewidth, it would seem that this could be an area worthy of more thourough investigation, both experimentally and theoretically.

CHAPTER 9

The Effects of Aging II : Reflection Electron Diffraction

9.1 Introduction.

When a high energy (100 keV) beam of electrons is incident upon a crystal surface at a low angle the beam is diffracted by the lattice. The reflection electron diffraction (RED) pattern produced yields information concerning the crystal lattice similar to that which may be obtained by transmission electron or by x-ray diffraction, or by the related technique of low energy electron diffraction (LEED). There are however certain distinct advantages to be gained in using RED rather than these other techniques when studying a process such as the aging process reported here.

Since the precipitates formed are coherent with the matrix (22) and are present only in very small quantities, and since the precipitate and host have similar lattices, x-ray back-reflection methods are likely to require excessively long exposure times; and powder methods, besides suffering from a similar problem, are destructive. Transmission electron diffraction is also a destructive technique, in view of the extremes of thinness required to allow transmission of the beam. The other technique mentioned - LEED - requires UHV conditions and is specifically for the study of atomically clean surfaces of low index planes of single crystals. Further, with the LEED technique the electrons only have a low energy and so will only penetrate the first few atomic layers of the sample. Clearly this is advantageous in an investigation of the surface only,

but would be of limited use in our case where we expect precipitates of perhaps 100 Å in extent, distributed throughout the material.

Considering its simplicity and effectiveness the RED technique has been surprisingly seldom utilised. It is described in a few of the standard texts, and introductory outlines of the technique have been given by Bauer (98) and by Russell (99). We mention here only those aspects particularily relevant to this study.

9.2 Experimental Details.

The RED work was carried out on a JEM-120 electron microscope, using a goniometer stage situated just below the projection lens of the microscope, so that the electron beam impinged on the large face of the sample at an angle of 1 - 2 degrees. The goniometer stage allowed for 360^{o} rotation of the sample about an axis perpendicular to the beam, for tilt of up to 10^{o} about a second horizontal axis perpendicular to the first, and for translation in two mutually perpendicular directions in the horizontal plane. It was therefore possible to examine different areas of the sample, in various orientations with respect to the beam. Charge which accumulated on the sample was neutralised as neccessary by means of an electron gun, mounted at the same level as the goniometer, which could be used to fire electrons with energies of 200 - 1000 eV at the samples. These electrons remove the charge both by ionising gas atoms to provide a conducting plasma, and by producing secondary emitted electrons from the surface of the sample.

The technique, besides being non-destructive, was fast and simple to carry out, owing to the use of a specimen airlock. In fact

it was possible to mount a sample, examine it in various orientations, and photograph the diffraction patterns obtained, all within the space of about ten minutes.

The samples to be observed were cleaned in acetone, dried in air and then etched in fuming nitric acid for five minutes. This etchant attacks the magnesium oxide more rapidly than it attacks the precipitates (100) so that the etching process produces a surface comprising etch hillocks with precipitates at the peaks. This is illustrated in the electron micrograph in Figure 9.1 which shows the etched surface of an undoped magnesium oxide crystal. The advantage in producing such a surface is that the electron beam preferentially samples precipitates when glanced off the surface. This enhances those parts of the diffraction pattern arising from the precipitates as compared with those arising from the bulk material.

9.3 RED - Some Theoretical Considerations.

The de Broglie electron wavelength coresponding to an accelerating potential V (volts) is given by

$$\lambda = \sqrt{\frac{150}{V(1 + 10^{-6}V)}}\ \text{Å} \qquad 9.1$$

Since V is typically 100 kV, $\lambda \approx 0.04$ A. The Bragg condition for diffraction is

$$\lambda = 2\, d_{hkl} \sin\theta \qquad 9.2$$

where d_{hkl} is the interplanar spacing and θ is the Bragg angle. Since d_{hkl} is $\approx$ 2 Å the Bragg angle $\approx 1^{\circ}$. Consequently only those sets of planes which are virtually parallel to the sample surface

Figure 9.2

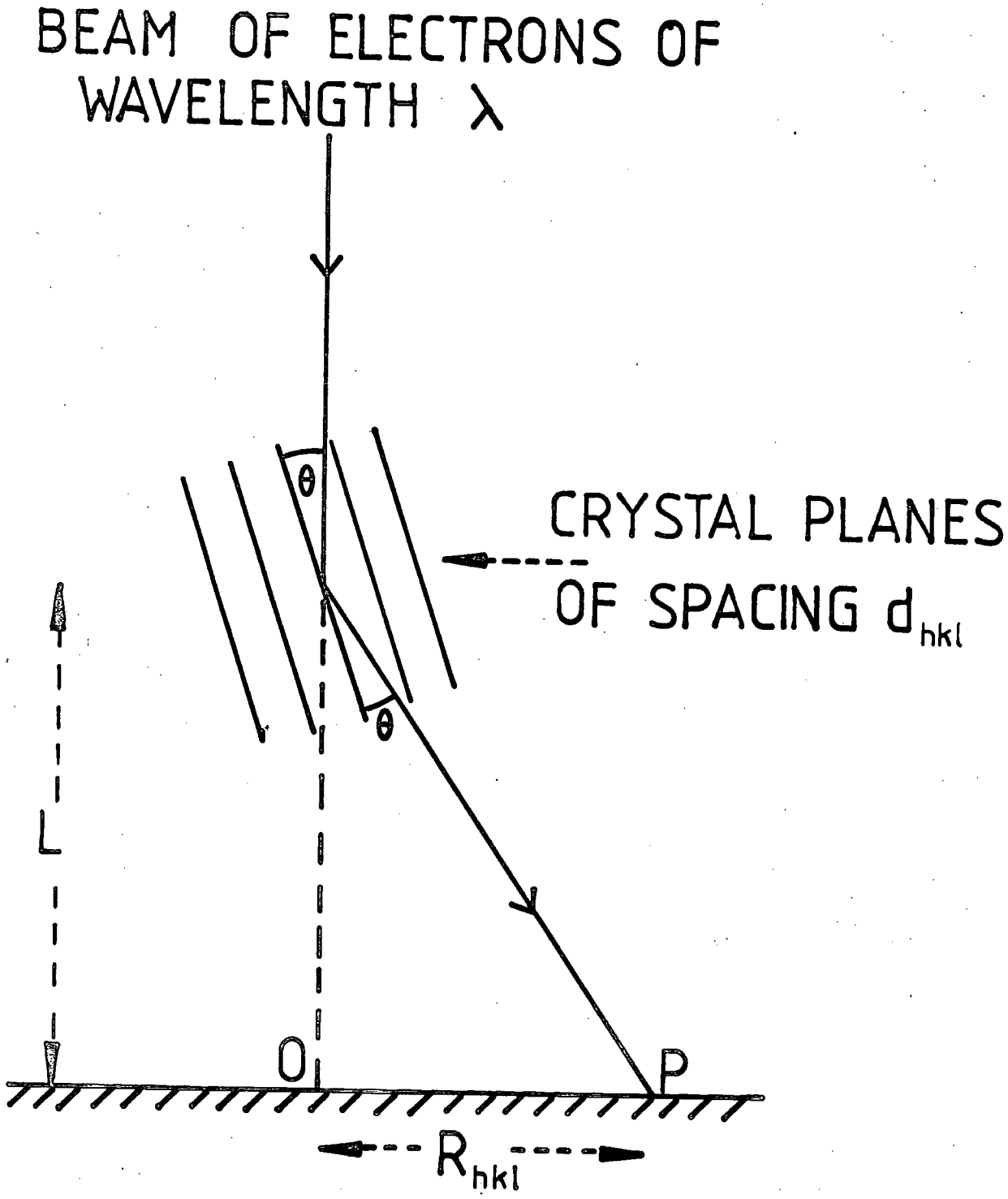
BEAM OF ELECTRONS OF WAVELENGTH λ
θ
CRYSTAL PLANES
OF SPACING d_{hkl}
θ
L
O
P
R_{hkl}

Figure 9.3

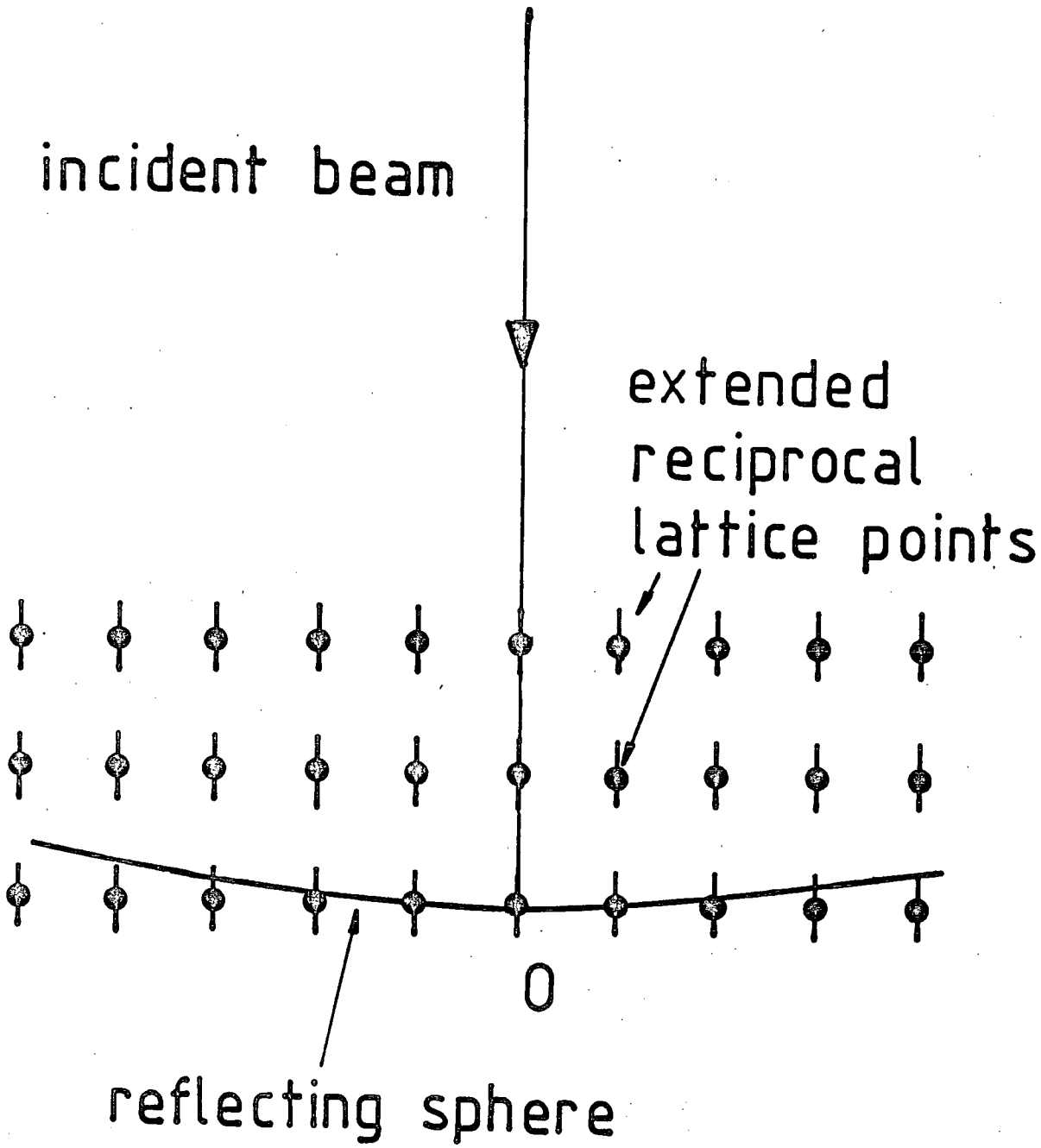
incident beam
extended
reciprocal
lattice points
O
reflecting sphere

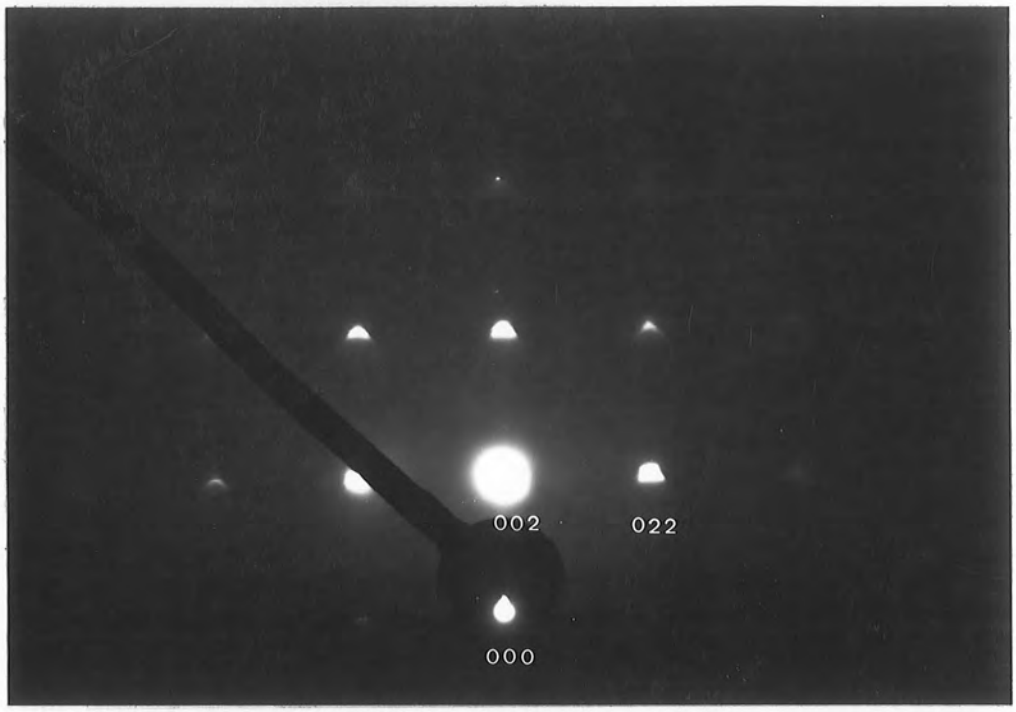

Figure 9.4 a) MgO - (100) reciprocal lattice plane

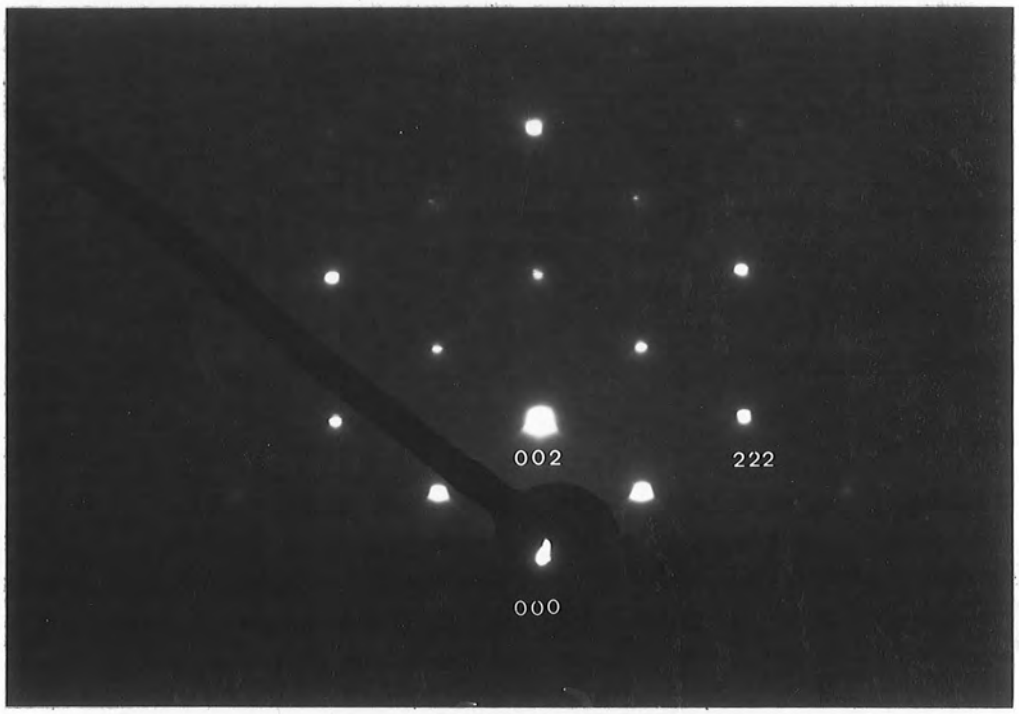

Figure 9.4 b) MgO - (110) reciprocal lattice plane

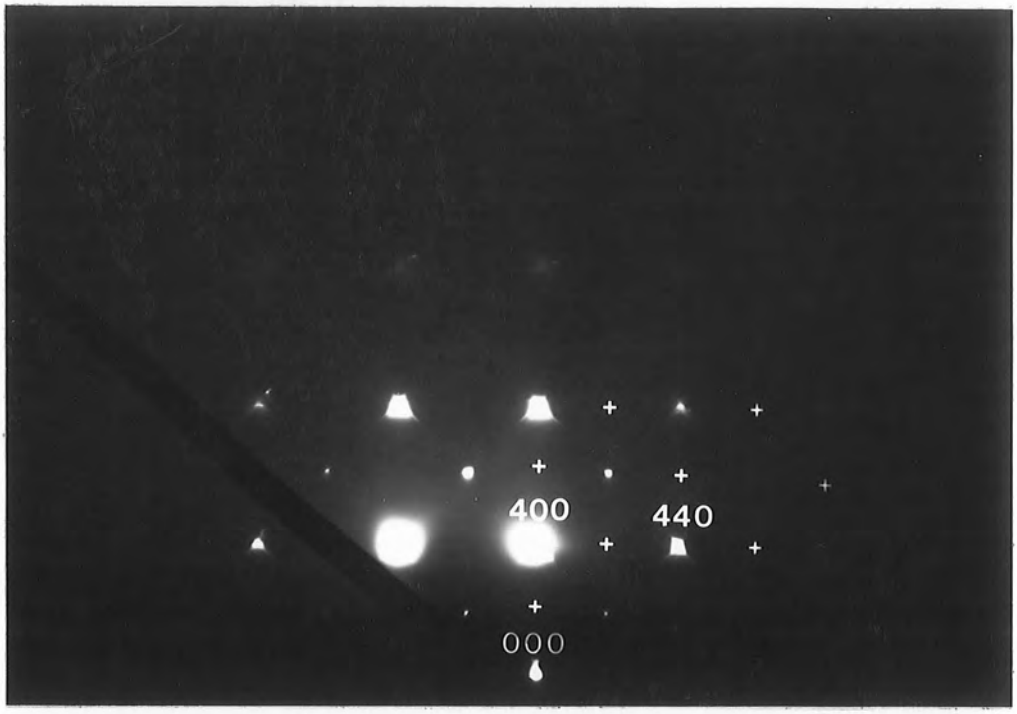

Figure 9.5 a) MgO and magnesioferrite - (100) r.l. plane

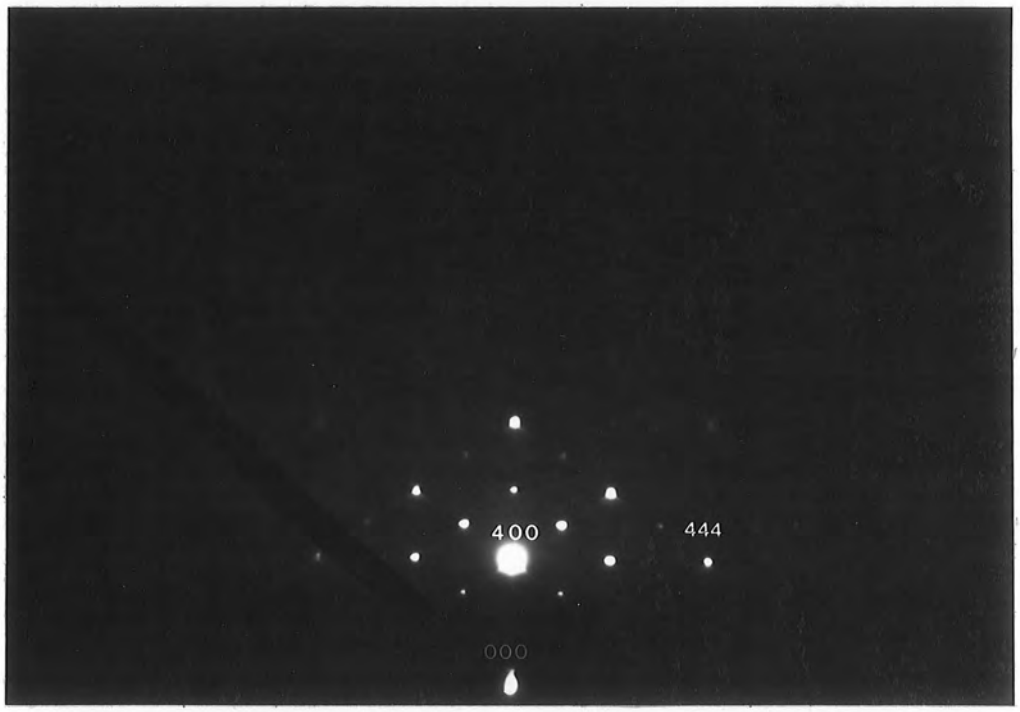

Figure 9.5 b) MgO and magnesioferrite - (110) r.l.plane

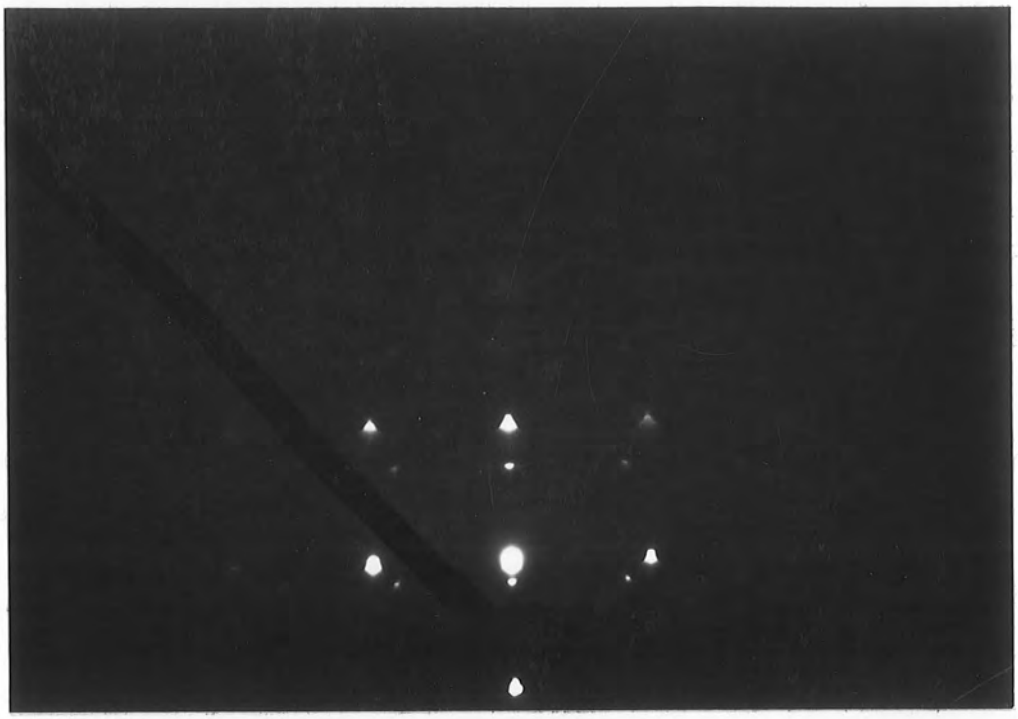

Figure 9.6 a) MgO showing additional spots from zirconia

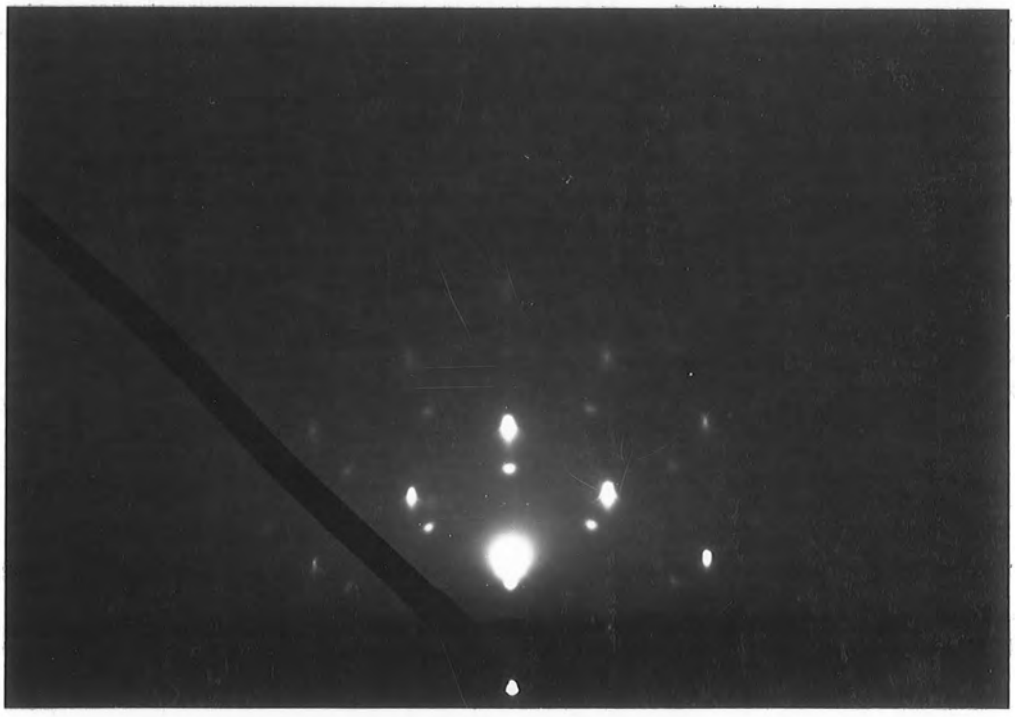

Figure 9.6 b) MgO showing additional spots from zirconia

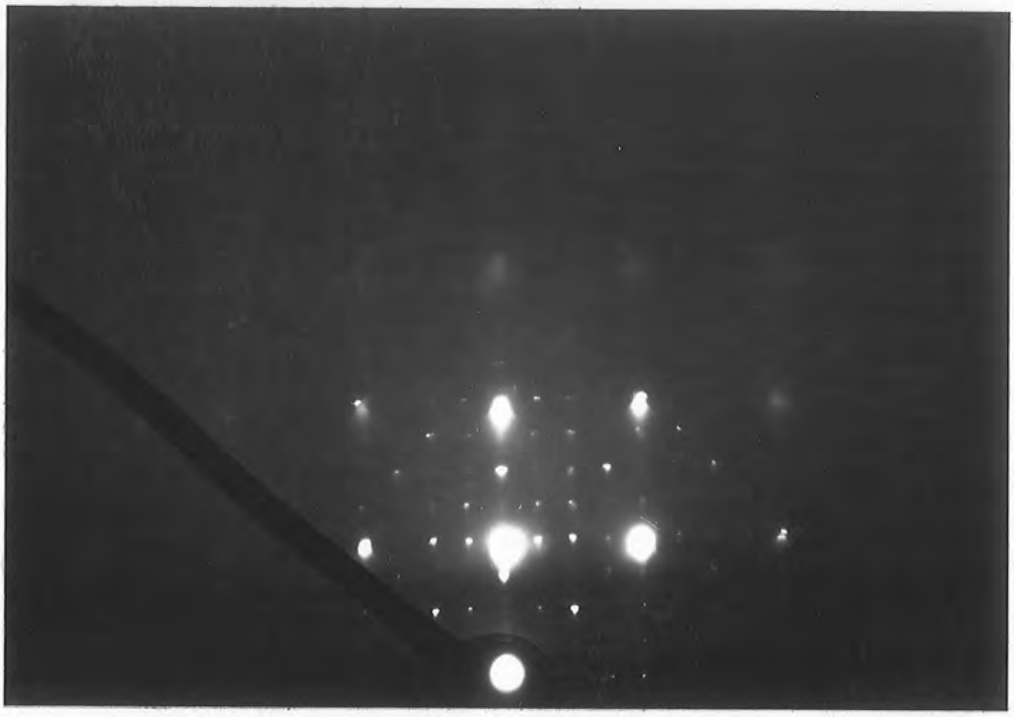

Figure 9.7 MgO showing pattern from unknown precipitate - (100)

- see below for indexing

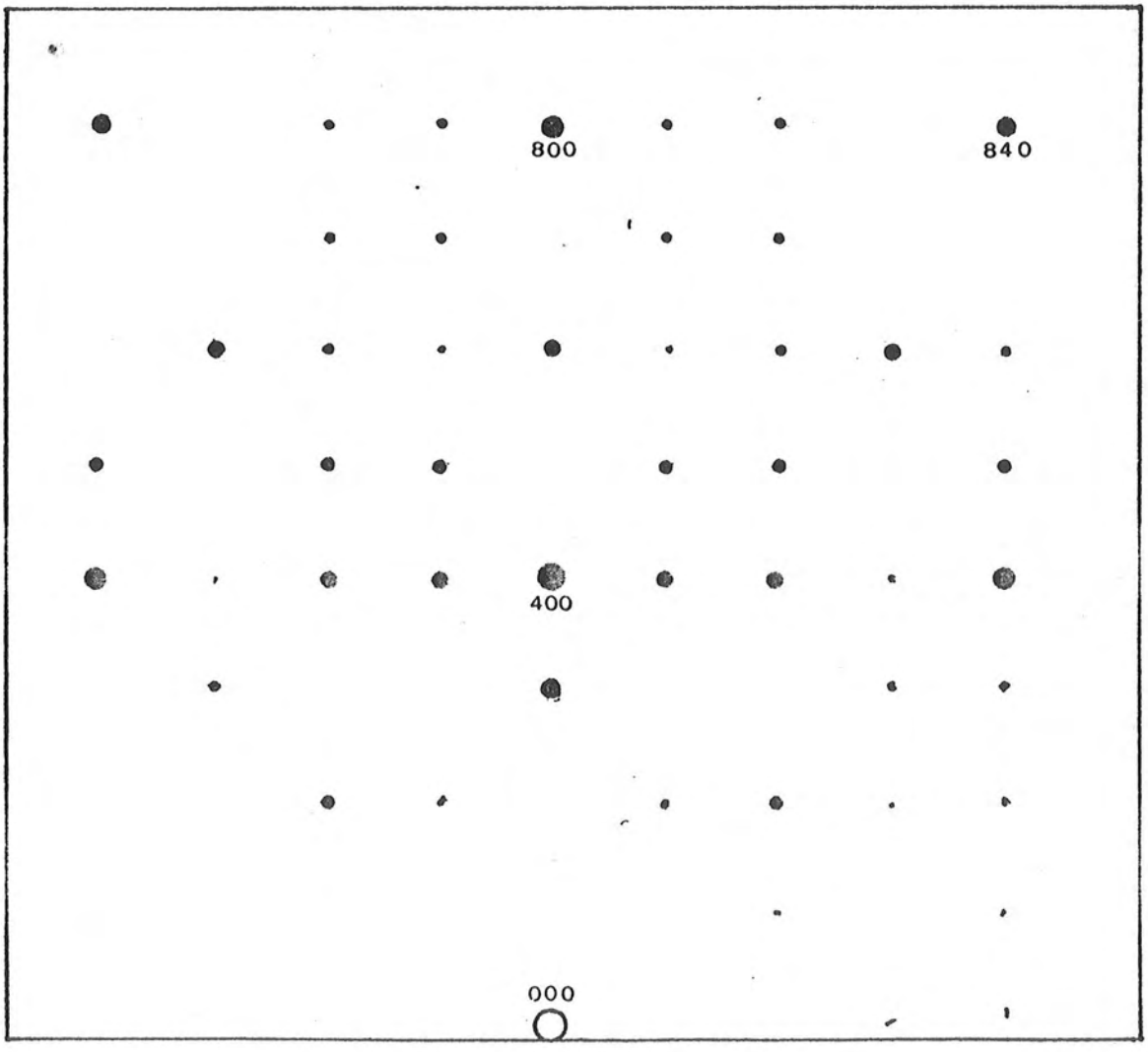

contribute to the diffraction pattern. It is clear from figure 9.2 that

$$R_{hkl} = L \tan 2\theta \qquad 9.3$$

where R_{hkl} is the distance from any diffracted spot to the undeviated beam (in the plane of the diffracted image), L is the distance from the sample to the film, and θ is the Bragg angle as before. Since θ is very small we may approximate, and at the same time combine 9.2 and 9.3 to obtain the 'camera equation'

$$\lambda L = R_{hkl} d_{hkl} \qquad 9.4$$

L is a constant for the camera (when the sample is located below the projection lens, as here), and λ and R may be determined, allowing d_{hkl} to be calculated. In practise L is usually found by first examining a sample of known interplanar spacing. In the work reported here a value for L was not calculated explicitly since all the specimens examined comprised mainly magnesium oxide. Where a second phase was evident its parameters could be determined by reference to the pattern from MgO which was present in all cases.

The interpretation of the diffraction patterns obtained using RED is considerably simplified because the very short wavelength of the electrons leads to a Ewald sphere which has a very large radius $(1/\lambda)$ in the reciprocal lattice construction. It can be seen from Figure 9.3 that in fact the sphere approximates to a plane section through the reciprocal lattice, and the diffraction pattern obtained corresponds directly to this plane section which is perpendicular to the direction of the incident beam.

The points of the reciprocal lattice do have a finite volume and as a result many more spots are obtained in the diffraction pattern than would otherwise be the case. In particular, as is shown in Figure 9.3 the reciprocal lattice points in our case are extended at right angles to the reciprocal lattice plane, mainly because the surface of the sample is covered with asperities, as a consequence of the etch treatment. These do not strictly behave solely as reflecting centres, but act as thin samples for transmitted electron diffraction as well, the thinness of the layers through which the beam can pass in real space giving rise to extended points in reciprocal space.

Other important aspects of RED which specifically relate to this work are dealt with as they arise in the next section where the results obtained by the RED technique are discussed.

9.4 RED Results: Spinel Formation.

Samples with various iron concentrations were examined after aging at temperatures in the range 600 - 800^{o}C for different lengths of time, in oxygen. Four different types of diffraction patterns were obtained in all. Two of these relate to the magnesium oxide and the growth of the ferrimagnetic precipitates, and they are discussed in this section. The other two are not thought to be directly related to the ferrimagnetic precipitates, and are dealt with in section 9.5.

The patterns in Figure 9.4 (a) and (b) arise from the magnesium oxide lattice, (a) showing a $\{100\}$ plane in reciprocal space obtained with the electron beam almost parallel to a $\langle 100 \rangle$ direction and (b) showing the $\{110\}$ plane, obtained with the beam almost parallel to a $\langle 110 \rangle$ direction. The lattice is face-centred cubic, and

indexing of the reciprocal lattice points is straightforward (101).

These patterns were obtained from a sample containing 11900 ppm iron, in the as-recieved state. The streaks associated with the spots are an indication of the degree of etching, being a result of electron refraction at the pyramidal faces of the etch hillocks. Similar patterns were obtained from all samples before heat treatment, and after solution treatment at 1400°C, with the exception of the 4N samples and one or two other special cases mentioned later.

Figures 9.5 (a) and (b) show patterns obtained with the same beam alignments as in 9.4, but in this case being taken from a sample which contains 2300 ppm iron, and which has been aged at 700°C for 7 hours. The spots on these patterns which are wholly or partly due to magnesium oxide may be determined by comparison with 9.4, and not surprisingly, they turn out to be the strong spots. The other spots which appear in figure 9.5 represent a second cubic lattice in register with the magnesium oxide lattice, and are thought to be caused by the magnesioferrite precipitates, which would have a lattice parameter of 8.38 Å in the bulk - very nearly exactly twice that of the host lattice. The pattern closely resembles that obtained by transmitted electron diffraction by Groves and Fine (22) and by Krawitz and Cohen (9). The indices shown in figure 9.5 refer to the magnesioferrite lattice. Evidence that this is a reasonable assignment in our case also may be deduced as follows.

First of all if one takes the allowed reflections given by the ASTM index for x-ray diffraction, then all the expected reflections are either present, or would be present at positions which would overlap the spots due to the MgO reflections.

Secondly, the systematic absences arising from the high

symmetry of the spinel structure may be obtained from the ASTM index as (200), (420), (600), (640), and (820). In some cases these overlap with host lattice reflections, in which case it is not possible to detect if they are present or otherwise. All other cases have been shown by '+' on the indexed pattern, and reference to the photographs shows that as far as the (100) plane is concerned the expected absences are indeed absent; whilst in the case of the (110) plane some of the spots which should be absent do appear - for example the (200) spinel reflection. This cannot be a genuine lattice reflection however, as it is not present in the (100) plane. It, and the other expected systematic absences which in fact 'turn up' in the (110) pattern are explained therefore by the phenomena of double diffraction (102).

This arises when part of the primary beam which has already been diffracted is incident upon a second precipitate, whereupon it acts as a primary beam producing a similar pattern to that produced by the main primary beam, but one which is displaced by an appropriate amount. In this case it is thought that the beams which would normally provide the (111) type reflections act as primary beams, producing patterns centred upon the (111) spots. What appears to be a (200) reflection due to the main primary beam is therefore explained as being a (111) type reflection due to a twice-diffracted beam. All the 'systematic absences which are present' in the (110) pattern may be explained in this way.

The diffraction patterns produced after aging are therefore consistent with the idea that a second phase with a spinel-type structure and a lattice parameter twice that of the magnesium oxide has been precipitated. Further evidence leading towards the same

conclusion may be briefly summarised as follows:-

i). The spinel pattern is consistently detected in only those samples which give a ferrimagnetic resonance signal, and samples which show the spinel RED pattern always give a ferrimagnetic resonance signal.

ii). The spinel pattern is never found in samples after solution treatment at 1400°C, but occurs in most samples for a wide variety of aging times in the 600 - 800°C temperature range.

iii). Whilst the intensity of the pattern is dependent upon a whole variety of factors - some of which, such as etch rate, are difficult to control precisely - it would seem from the many dozens of individual obsevations made on different samples that the spinel pattern forms most rapidly, and with the greatest intensity relative to the host lattice pattern, in those samples which have the highest iron concentrations, or are subject to the longest aging times or the highest temperatures (within the 'aging' range) - or any combination of these factors. This is of course consistent with the corresponding growth in the intensity of the ferrimagnetic resonance signal, as discussed in the last chapter.

The diffraction spots attributed to the spinel precipitates were detected in samples of all iron concentrations from 310 ppm upwards, when appropriately aged; but not in the 4N samples even after 24 hours at 800°C. Again this is in line with the findings of the FMR experiments, and again it would seem reasonable to suggest that were the aging process continued for long enough then we would find

spinel precipitates in the 4N samples as well.

It is important to point out that as far as the electron diffraction studies were concerned, there was no distinction, other than one of intensity, between the consequence of aging at 700°C and 800°C. The changes which took place in the diffraction pattern when the spinel phase was precipitated were always the same, regardless of aging temperature or time.

There is one additional point which should be made with regard to the spinel diffraction pattern. Close examination of Figure 9.5 (b) shows that there is very slight evidence of polycrystallinity, in the very faint rings which may be detected passing through some of the spots. It is not really clear why this should be since it is expected that the precipitates should form in register with the lattice - the ease of precipitation depending to a certain extent upon the fact that the host and precipitate share the same oxygen lattice - and this is generally true, otherwise the spinel spots would be much more like complete rings. It may be that because of the slight mismatch between the lattices that as the precipitates grow the effects of the mismatch become greater, leading to strain. Alternatively, the etching process may lead to a redeposition of some of the exposed precipitate material on the sample surface, either in a polycrystalline from or in random orientation compared with the MgO lattice.

9.5 RED Results: Other Structures.

Whilst most of the samples investigated followed the general pattern of behaviour outlined in the previous section, two different deviations from this were noted for certain samples, on a few

occasions. These deviations manifested themselves in two quite distinct diffraction patterns, which are shown in Figures 9.6 and 9.7.

We consider first the patterns of Figure 9.6. As with the spinel pattern discussed in the previous section the main spots of this pattern are due to the magnesium oxide lattice, but superimposed are spots due to a second cubic structure of slightly greater lattice parameter than the MgO. The regular arrays of fainter spots clustered beside each of the main reflections are caused by double diffraction. It is interesting to note that whilst the refraction streaks at the MgO spots are strong, indicating regular pyramidal etch hillocks with their faces in the $\{111\}$ real space planes, the spots due to the precipitate have faint indications of polycrystalline rings.

This particular pattern was only recorded in the 4N samples, in which it was always present in the as-recieved state. Furthermore, heat treatments at 700 - 800°C and 1400°C did not apparently affect it in any way. The lattice parameter of the unknown structure was determined by comparison with the MgO lattice as 5.10 Å, and it is thought that these patterns are due to the same precipitates as were observed by Venables (8) as arising in Norton Co. MgO, and which also exhibited a cubic structure, with a lattice parameter of 5.14 Å. After a very much more detailed investigation than we have had time for Venables came to the conclusion that these particular diffraction patterns are due to precipitates of calcium-stabilised zirconia.

In order to correlate the volume of precipitate estimated from electron micrographs with the total amount of zirconium detected in the samples by neutron-activation analysis, Venables found it necessary to postulate that virtually the total content of zirconium had precipitated out, even when that content was of the order

of 1 ppm; and that in doing so it had managed to scavenge sufficient calcium locally to stabilise the cubic structure. This identification hinged on the relative intensities of x-ray powder diffraction lines. In the absence of a better explanation one has to accept this assignment, but there are one or two points which are still not yet fully explained satisfactorily:-

i).The precipitates have never been reported in other than undoped samples. Furthermore, whilst we have found them regularily in 4N crystals, all other crystals have been free of them, suggesting that they occur preferrentially in purer material. The zirconium content is so small and the precipitation so ready that it seems odd that such a small increase in other impurities should have such an effect on the behaviour of the zirconium.

ii).The lattice parameter of this second structure is so different from that of MgO that it is not really clear why such single crystal precipitates should form so readily in such close register with the MgO lattice. In only two to three unit cell distances the lattice planes would be completely 'out of step'. In spite of this, the precipitated material is consistently observed to be in excellent register with the MgO lattice.

However we cannot at present put forward a more reasonable explanation, and according to Henderson and Wertz (1), the zirconium and calcium content of Spicer crystals is comparable with that of the Norton material examined by Venables.

The second unusual pattern which we have detected, in one 4N

sample, one 2300 ppm iron doped sample, and two different 4300 ppm iron doped samples, is shown in Figure 9.7. This pattern has only been recorded after solution treatment of the samples at 1400°C for twenty-four hours in one atmosphere oxygen and in view of the rarity with which it occurs it has not proved possible to demonstrate which of these factors are essential to its production. The samples which gave this pattern showed no sign of it before heat treatment, and the apparent intensity and the relative intensities of the spots would seem to be independent of sample despite the orders of magnitude difference in iron content.

A further important factor which mitigates against this pattern being due to a precipitate based on iron is that no changes are detected in the paramagnetic resonance signal, other than the expected increase in intensity of the isolated iron ion spectrum. There is no suggestion of a ferri- or ferro-magnetic resonance signal appearing, which suggests that whatever is forming the precipitate is probably not a magnetic ion. This excludes Cr^{3+} as well as Fe^{3+} from being involved.

The pattern is not understood at present, although it has been tentatively indexed as a spinel structure in register with the magnesium oxide lattice. Beneath the photograph the indexing scheme is shown. An obvious difficulty which arises if one wishes to index this structure as a spinel is the presence of so many reflections which should be systematic absences. The magnesioferrite spinel did not behave in this unorthodox way!

In order to form a spinel structure we require a '3+' ion, with the restriction that in this case it should be a non-magnetic one. The obvious candidate is aluminium, Al^{3+}, which forms the

spinel $MgAl_2O_4$. Aluminium is a common impurity in Spicer MgO crystals (1), usually in concentrations of 100 - 200 ppm. The situation is complicated by the fact that although most ions are expected to show a preference for either tetrahadral or octahedral sites, experimental evidence suggests that even in the bulk stoichiometric material the expected behaviour is not always consistent. Consequently it is time consuming to work through the structure factor calculations for various possible degrees of inversion of the $MgAl_2O_4$ cell, with a view to determining whether this pattern could arise from such a structure. The task is not made any simpler by the fact that there has been considerable debate in the literature recently (104-108) as to the precise crystal structure of spinel and the electron diffraction pattern one should expect from it.

It was mentioned in Chapter 2 that calculations carried out by Gourdin and Kingery (35) suggest that aluminium spinel is likely to form as precipitates in the magnesium oxide lattice. Aluminium spinel has been reported on one occasion previously (41) as a precipitate in magnesium oxide, when a transmission electron diffraction pattern of the (111) reciprocal space plane was published. Unfortunately our samples are $\{100\}$ slices so we have been unable to obtain a diffraction pattern in this orientation, for comparison. It is hoped to obtain such a pattern in future; to this end work is continuing with samples of Mgo deliberately doped with aluminium.

One further point that should be noted about this particular pattern is that the only refraction streaks are at right-angles to the sample surface - the 'shadow' of which may just be made out at the bottom of the photograph. This implies that the crystal surface is

smoothly polished, and does not show etch hillocks like those caused by the iron spinel precipitates.

9.6 RED Results: Conclusions.

The findings of the RED work may be briefly summarised as follows:-

i). No samples showed evidence of magnesioferrite precipitation either in the as recieved state, or after solution treatment at 1400°C.

ii). Samples with an iron content of 310ppm or more showed evidence of magnesioferrite precipitation, even after short aging times (minutes) at temperatures in the range 600 - 800°C.

iii). Although the technique is probably more sensitive than transmission electron diffraction in detecting relatively small quantities of precipitated material, as a consequence of the disproportionately large volumes of precipitate preferrentially sampled, it was not possible to distinguish in any way between the patterns due to precipitation caused by aging at different temperatures in the 600 - 800°C range.

iv). The magnesioferrite precipitates are generally in alignment with the lattice, as expected, although there is faint evidence that there may be a small amount of polycrystallinity.

v). Although the technique is non-quantitative, it does seem that the intensity of the spinel precipitate patterns which appear and the readiness with which they appear is in proportion to the aging time,

the aging temperature, and the iron concentration in the sample.

vi). Two precipitate structures other than magnesioferrite spinel have been detected. One is identified as that which Venables (103) ascribed to cubic calcium-stabilized zirconia, and although the evidence for this identification is not thought to be compelling it is accepted in the absence of any obvious alternative. The second unknown pattern has not been identified, although it is thought that it may be due to aluminium spinel precipitates. Work is continuing in an attempt to confirm this identification.

SUMMARY

The distribution of iron in single crystal magnesium oxide has been investigated using the techniques of electron paramagnetic resonance, ferrimagnetic resonance and reflection electron diffraction. The total iron content of the samples investigated was in the range 100 - 13000 ppm by weight, and measurements were made on the crystals in the as received state, after solution treatment, and following various aging treatments.

Integration of the EPR spectral lines suggests that both as received and solution treated samples have considerably less iron in the Fe^{3+} state in isolated, cubic sites than is expected. In some cases the total iron content in these sites is considerably less than one per cent of the iron. Whilst the solution treatment does increase this quantity, in some cases by up to ten times, only in the most lightly doped samples does the amount of iron contributing to this spectrum approach the total amount of iron in the sample.

The experimental EPR linewidths are broader than expected on the basis of dipolar broadening theory, although the discrepancy is considerably reduced by solution treatment. The analysis of the linewidths provides strong supporting evidence for the idea that much of the iron is clustered in some way, even in the as grown crystals.

After solution treatment a very broad (1.3 kG wide) very low amplitude line was detected in two samples. The appearance of this line was accompanied by the disappearance of the fine structure lines, and whilst the two events appear to be related it is not clear why this should be. At liquid helium temperatures this line shows a

complicated structure. A fuller investigation of this broad line would be worthwhile, since the structure may give information on the earliest stages of the precipitation of magnesioferrite.

However, in general neither the FMR nor the RED studies gave any evidence of the precipitation of magnesioferrite in the as grown state, or after solution treatment. The RED studies did give evidence of two other precipitates, both of which exhibited a cubic structure in register with the host lattice. One of these, with a lattice parameter of 5.10 Å, is similar to the precipitates which Venables has suggested are calcium-stabilised zirconia. These precipitates are always found, and only found, in the 4N material. It is tentatively suggested that the second unusual diffraction pattern, which only appears after solution treatment, may be due to precipitates of magnesium aluminium spinel. Work is continuing in an attempt to verify this assignment.

Following aging, all except those samples with the lowest concentrations of iron showed evidence of the precipitation of magnesioferrite. The RED patterns which appeared following aging were, barring intensity, always the same, regardless of sample, aging time or aging temperature. They comprised a characteristic spinel pattern having a lattice parameter very close to exactly twice that of MgO. On the other hand the FMR spectra showed different spectral lines, depending upon time of aging. Initially an isotropic line was produced, which gave way upon continued aging to a much broader, anisotropic line. Although the isotropic line is not understood, it is thought to be due in some way to the early stages of the clustering process.

The measured anisotropy was used to characterise the

precipitates in some samples in terms of chemical structure, magnetic properties, mean volume and growth rate. It was found that the volume of the precipitates increased linearly with time from aging times of one hour onwards; that the appropriate chemical formula was $Mg_xFe_{3-x}O_{4-(x-1)/2}$ where x = 1.29; and that the fraction of magnesium ions on tetrahedral sites was 0.30. The growth parameters are in accord with published data, which is of particular interest since it implies that the precipitate growth process is consistent and reproducible. This will simplify considerably the programme being put in hand to correlate precipitate growth with changes in dielectric behaviour.

The measured anisotropy was found in each case to follow the empirical law

$$\sqrt{|H_a^{sp}|} = C + DT$$

where D = -0.045 ±.004 $G^{0.5}K^{-1}$, T is temperature, and C a sample dependent constant.

The widths of the FMR lines of the high concentration samples aged at 800°C were independent of iron concentration, but after one hours aging narrowed continually with aging. It is suggested that this is a consequence of 'voids' of MgO within the initial clusters which act as do voids in polycrystalline ferrites to broaden the lines, but which gradually 'fill in' with precipitate as aging progresses. These same linewidths were also found to decrease monotonically with increasing measurement temperature between 110 K and 410 K, which is a result quite at variance with the reported behaviour of FMR linewidths in bulk magnesioferrite. It is thought that this discrepancy may be a consequence of the superparamagnetic

nature of the precipitates. It is felt in view of the consistency of the measured widths and their sample independence that this is an area which might merit further investigation, both theoretically and experimentally.

REFERENCES

1. A. Henderson and J.E.Wertz, 'Defects in the Alkaline Earth Oxides' Taylor and Francis Ltd., London, 1977.
2. D. Woodhouse and J.White, 'Trans. Brit.Ceram.Soc. 54 (1955) 333.
3. J. Brynestad and H.Flood, Z. fur Elektrochem. 62 (1958) 953.
4. H.S.Belson and C.J.Kriessman, J.Appl.Phys. Suppl. V30 (1959) 170S.
5. L.C.F.Blackman, Trans.Faraday Soc. 55 (1959) 391.
6. A.K.Goswain, M. Rosenbloom, and R.W.Teale, J.Appl.Phys. 39 (1968) 828.
7. P. Reijnen, Philips Res.Reports, 23 (1968) 151.
8. A.B. van Groenon, P.F.Bongers, and A.L.Stuyts,Mater.Sci.Eng. 3 (1968/69), 317.
9. A. Krawitz and J.B. Cohen,J.Am.Ceram.Soc.,57 (1974) 186.
10. W. K.Chen and N.L.Petersen, J.Phys. Chem.Solids, 41 (1980) 335.
11. W.Low, Proc.Phys.Soc.(London), B69 (1956) 1169.
12. W.Low and M.Weger, Phys.Rev. 118 (1960) 1130.
13. A.M.Stoneham, K.A.Müller,and W.Berlinger, Solid St.Comm.,10 (1972)1005.
14. F.A.Modine, E.Sonder and R.A.Weeks, J.Appl.Phys. 48 (1977) 3514.
15. J.E.Wertz, J.W.Orton and P.Auzins, J.Appl.Phys. 33 (1962) 322.
16. J.S.Thorp, R.A.Vasquez, C.Adcock and W.Hutton, J.Mater.Sci., 11 (1976) 89.
17. A.D.Inglis and J.S.Thorp, J.Mater.Sci. 16 (1981) 1887.
18. B.Henderson, J.E.Wertz, T.P.P.Hall and R.D.Dowsing, J.Phys.C : Solid St.Phys. 4 (1971) 107.
19. R.A. Weeks, J.Gastineau and E.Sonder, phys.stat.sol(a) 61 (1980) 265.
20. J.W.Orton, P.Auzins, J.H.E.Griffiths and J.E.Wertz, Proc.Phys.Soc. 78 (1961) 554.
21. E.Sonder, T.G.Stratton and R.A.Weeks, J.Chem.Phys. 70 (1979) 4603.
22. G.W.Groves and M.E. Fine, J.Appl.Phys. 35 (1964) 3587.
23. G.P.Wirtz and M.E.Fine, J.Appl.Phys. 38 (1967) 3729.

24. G.P.Wirtz and M.E.Fine, J.Amer.Ceram.Soc. 51 (1968) 402.

25. K.N.Woods and M.E.Fine, J.Amer.Ceram.Soc. 52 (1969) 186.

26. K.N.Woods and M.E.Fine, J.Appl.Phys. 40 (1969) 3425.

27. R.J. Stoker, J.Amer.Ceram.Soc. 48 (1965) 60.

28. Idem. ibid 49 (1966) 39.

29. G.D.Miles, F.J.P.Clarke, B.Henderson, and R.D.King, Proc.Brit.Ceram.Soc. 6 (1966) 325.

30. R.W.Davidge, J.Mater.Sci. 2 (1967) 339.

31. B.J.Wicks and M.E.Lewis, Phys.stat.sol (a) 6 (1971) 281.

32. B. Reppich, Mater.Sci.Eng. 22 (1976) 71.

33. F. Sato and K.Sumino, J.Mater.Sci. 15 (1980) 1625.

34. R.S. de Biasi, Magn.Lett. 1 (1978) 103.

35. W.H.Gourdin, W.D.Kingery, J.Mater.Sci. 14 (1979) 2053.

36. W.H.Gourdin, W.D.Kingery, and J.Driear, J.Mater.Sci.14 (1979) 2074.

37. R.W.G. Wyckoff, 'Crystal Structures', Vol.I., Interscience (1965).

38. R.D.Shannon and C.T.Prewitt, Acta.Cryst. B25 (1969) 925.

39. L.J.C.Bluck, M.Sc.Thesis, Durham Univ. (1979) (unpublished).

40. A.Abragam and B.Bleaney, 'Electron Paramagnetic Resonance of Transition Ions', Clarendon Press, Oxford, 1970, p 445.

41. B.Henderson, Phil.Mag. 9 (1964) 153.

42. E.F.Harris and J.H.Crawford, Jr., phys.stat.sol.(a) 35 (1976) 667.

43. B.Phillips, S.Somiya, and A.Muan, J.Am.Ceram.Soc. 44 (1961) 169.

44. C.P.Poole, 'Electron Spin Resonance', Wiley-Interscience, N.Y.,1967.

45. C.P.Poole, H.A.Farach, 'The Theory of Magnetic Resonance', Wiley-Interscience, N.Y., 1972.

46. H.Bethe, Ann.Phys., 3 (1929) 133.

47. J.H.Van Vleck, W.G.Penney, Phil.Mag. 17 (1934) 961.

48. Reference 40, p 441.

49. P. Debye, Ann.Physik., 32 (1938) 85.

50. R. de L Kronig, C.J.Bouwkamp, Physica 6 (1939) 290.

51. J.L.Kolopus, L.V.Holroyd, phys.stat.sol. 8 (1965) 711.

52. R.S.de Biasi, phys.stat.sol.(b) 87 (1978) K29.

53. W.Low, Phys.Rev. 105 (1957) 792.

54. C.P.Poole, H.A.Farach, 'Relaxation in Magnetic Resonance' Academic Press, N.Y., 1971.

55. J.H.Van Vleck, Phys.Rev. 74 (1948) 1168.

56. P.W.Anderson, P.R.Weiss, Rev.Modern Phys. 25 (1953) 269.

57. C.Kittel, E.Abrahams, Phys.Rev. 90 (1953) 238.

58. W.J.C.Grant, M.W.P.Strandberg, Phys. Rev. 135 (1964) A715.

59. B.I.Kochelaev, R.Kh.Sabirov, G.G.Khaliullin, Sov.Phys.Solid State 19 (1977) 86.

60. J.S.Thorp, M.D.Hossain, L.J.C.Bluck, J.Mater.Sci.14 (1979) 2853.

61. J.S.Thorp, M.D.Hossain, L.J.C.Bluck, T.G.Bushell, J.Mater.Sci.15 (1980) 903.

62. P.W.Anderson, Phys.Rev. 79 (1950) 350.

63. S.A. Al'tshuler, B.M.Kozyrev, 'Electron Paramagnetic Resonance in Compounds of Transition Elements', 2nd Ed., 1974., U.K.distrib. J.Wiley & Sons, Chichester.

64. G. Arfken, 'Mathematical Methods for Physicists' Acad.Press, N.Y. London (1966).

65. B.Bleaney, K.W.H.Stevens, Rep.Prog.Phys. 16 (1953) 108.

66. Reference 1, p.40.

67. R.S. de Biasi, A. Caldas, J.Phys.C. 10 (1977) 107.

68. 'Operational Considerations with the V4532 Dual Sample Cavity' Varian Publication No.87-214-002 (Varian, Palo Alto).

69. S. Hodgskiss, Ph.D.Thesis, University of Durham (unpublished).

70. T.A.Yager, W.D. Kingery, J.Mater.Sci.16 (1981) 489.

71. J.H. Van Vleck, Nuovo.Cim.Supp.6 (1956) 993.

72. R.S.de Biasi, T.C.Devezas, Phys.Lett. 50A (1974) 137.

73. Idem, J.Am.Ceram.Soc. 59 (1976) 55.

74. Idem, Physica 86-88B (1977) 1237.

75. Idem, J.Appl.Phys. 49 (1978) 2466.

76. R.S.de Biasi, J.Magn. & Magn.Mater.8 (1978)178.

77. R.K. Wangsness, Phys.Rev. 86 (1952) 146.

78. Idem, ibid 91 (1953) 1085.

79. Idem, ibid 93 (1954) 68.

80. Idem, ibid 98 (1955) 1200.

81. Idem, Am.J.Phys. 24 (1956) 60.

82. C. Kittel, Phys.Rev., 71 (1947) 2702.

83. Idem, ibid 73 (1948) 155.

84. Idem, ibid 76 (1949) 743.

85. J.M.Luttinger, C.Kittel, Helv.Phys. Acta, 21 (1948) 480.

86. D.Polder, Phil.Mag. 40 (1949) 99.

87. J.M.Richardson, Phys. Rev. 75 (1949) 1630.

88. J.H.Van Vleck, ibid 78 (1950) 266.

89. A.G.Gurevich, 'Ferrites at Microwave Frequencies', Consultants Bureau Enterprises Ltd., N.Y, 1963.

90. C.Kittel, Phys. Rev. 70 (1946) 965.

91. C.P. Bean, J.D.Livingston, J.Appl.Phys, 30 Suppl.(1959) 120S.

92. J.D.Livingston, C.P.Bean, ibid, 30 Suppl. (1959) 318S.

93. R.M.Asimow, Trans.AIME, 233 (1965) 401.

94. I.M.Lifshitz, V.V.Slyozov, J.Phys. Chem.Solids,19 (1961) 35.

95. See Reference 4.

96. V.J.Folen, G.T.Rado, J.Appl.Phys. 29 (1958) 438.

97. P.E.Seiden, J.G.Grunberg, J.Appl.Phys. 34 (1963) 1696.

98. E.Bauer, in 'Techniques of Metals Research' Vol.2, ed. R.F.Bunshal, Wiley-Interscience, N.Y, 1969.

99. G.J.Russell, Prog.Cryst.Growth Charact.,(to be published)

100. D.H.Bowen, Proc.6th Saclay Metall.Colloq. (1962) p 151.

101. P.B.Hirsch, et al, 'Electron Microscopy of Thin Crystals' Butterworths, London (1965) p 499.

102. Reference 10, p 117.

103. J.D. Denables, J.Appl.Phys. 34 (1963) 293.

104. L. Hwang, A.H.Heuer, T.E.Mitchell, Phil.Mag. 28 (1973) 241.

105. A.H.Heuer, T.E.Mitchell, J.Phys.C: Solid State Phys. 8 (1975) L541.

106. R.K.Mishra, G.Thomas, Acta.Cryst. A33 (1977) 678.

107. P.Thompson, N.W.Grimes, J.Appl.Cryst. 10 (1977) 369.

108. P.P.K.Smith, Phil.Mag. B 38 (1978) 99.